Online System Identification for Fault Tolerant Control of Unmanned Aerial Vehicles

by
Jéan-Paul Appel

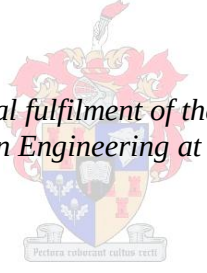

Thesis presented in partial fulfilment of the requirements for the degree Master of Science in Engineering at Stellenbosch University

Supervisor: Dr I.K. Peddle
Department of Electrical & Electronic Engineering

March 2013

Declaration

By submitting this thesis electronically, I declare that the entirety of the work contained therein is my own, original work, that I am the sole author thereof (save to the extent explicitly otherwise stated), that reproduction and publication thereof by Stellenbosch University will not infringe any third party rights and that I have not previously in its entirety or in part submitted it for obtaining any qualification.

March 2013

Abstract

In this thesis the strategy for performing System Identification on an aircraft is presented. The ultimate aim of this document is to outline the steps required for successful aircraft parameter estimation within a Fault Tolerant Control Framework.

A brief derivation of the classical 6 degree-of-freedom aircraft model is firstly presented. The derivation gives insight into the aircraft dynamics that are to be used to estimate the aircraft parameters, and provides a basis for the methods provided in this thesis.

Different techniques of System Identification were evaluated, resulting in the choice of the Regression method to be used. This method, based on the Least-Squares method, is chosen because of its simplicity of use and because it does not require as much computational time as the other methods presented. Regression methods, including a recursive algorithm, are then applied to aircraft parameter estimation and practical considerations such as Identifiability and corrupted measurements are highlighted.

The determination of unknown measurements required for System Identification of aircraft parameters is then discussed. Methods for both estimating and measuring the Angle-of-Attack (AoA) and angular accelerations are presented. The design and calibration of an AoA probe for AoA measurements, as well as a novel method that uses distributed sensors to determine the angular accelerations is also presented.

The techniques presented in this thesis are then tested on a non-linear aircraft model. Through simulation it was shown that for the given sensor setup, the methods do not provide sufficiently accurate parameter estimates. When using the Regression method, obtaining measurements of the angle-of-attack solely through estimation causes problems in the estimation of the aerodynamic lift coefficients.

Flight tests were performed and the data was analyzed. Similar issues as experienced with estimation done on the non-linear aircraft simulation, was found. Recommendations with regards to how to conduct future flight tests for system identification is proposed and possible sources of errors are highlighted.

Opsomming

In hierdie tesis word die strategie vir die uitvoering van Stelsel Identifikasie op 'n vliegtuig aangebied. Die uiteindelike doel van hierdie document is om die stappe wat nodig is vir 'n suksesvolle vliegtuig parameter beraming, binne 'n Fout Tolerante Beheer Raamwerk, uit eente sit.

'n Kort afleiding van die klassieke 6 graad-van-vryheid vliegtuig model word eerstens aangebied. Die afleiding gee insig in die vliegtuig dinamika wat gebruik moet word om die vliegtuig parameters te beraam, en bied 'n basis vir die metodes wat in hierdie tesis verskyn.

Verskillende tegnieke van Stelsel Identifikasie is geëvalueer, wat lei tot gebruik van die regressie-metode. Hierdie metode is gekies as gevolg van sy eenvoudigheid en omdat dit nie soveel berekening tyd as die ander metodes vereis nie. Regressie metodes, insluitend 'n rekursiewe algoritme, word dan toegepas op vliegtuig parameter beraming en praktiese orwegings soos identifiseerbaarheid en korrupte metings word uitgelig.

Die bepaling van onbekende afmetings wat benodig is, word vir Stelsel Identifisering van die vliegtuig parameters bespreek. Metodes om die invalshoek en hoekige versnellings te meet en beraam, word aangebied. Die ontwerp en kalibrasie van 'n invalshoek sensor vir invalshoek metings, sowel as 'n nuwe metode wat gebruik maak van verspreide sensore om die hoekversnellings te bepaal, word ook aangebied.

Die tegnieke wat in hierdie tesis aangebied is, word dan op 'n nie-lineêre vliegtuig model getoets. Deur simulasie is dit getoon dat die metodes vir die gegewe sensor opstelling nie voldoende akkurate parameters beraam nie. Dit is ook bewys dat met die gebruik van die Regressie metode, die vekryging van metings van die invalshoek slegs deur skatting, probleme in die beraming van die aerodinamiese lug koëffisiente veroorsaak.

Die tegnieke wat in hierdie tesis verskyn, word dan op werklike vlug data toegepas.Vlugtoetse is uitgevoer en die data is ontleed. Aanbeveling met betrekking tot hoe om toekomstige vlug toetse vir Stelsel Identifikasiete word voorgestel, en moontlike bronne van foute word uitgelig.

Acknowledgements

I would like to extend my gratitude to the following people:

- Dr. Ian Peddle for his support and guidance that he provided throughout the course of this project.
- My immediate family, especially my Mom and Dad who have made it possible for me to be where I am today. I thank you for all the support that you have provided me. I thank you for the guidance and the inspiring words that you have given me in times when things have gone rough.
- I thank all my friends who have supported me, distracted me and motivated me when needed.
- I thank my current work, Denel Dynamics, for supporting me and giving me the necessary time off that I required to finish off this dissertation.
- Finally I thank the Lord Jesus Christ for making this all possible. You deserve all the praise and acknowledgement. “For the Lord giveth wisdom: and out of his mouth cometh knowledge and understanding”, Proverbs 2:6.

Table of Contents

Declaration i

Abstract ii

Opsomming iii

Acknowledgements iv

Table of Contents v

List of Figures x

List of Tables xiii

Nomenclature xiv

Chapter 1 1

Introduction and Overview 1

1.1 Background 1

1.2 System Identification Background and Overview 6

1.3 Thesis Outline 7

Chapter 2 9

Aircraft Dynamics 9

2.1 Introduction 9

2.2 Coordinate Systems and Notation 9

2.2.1 Coordinate Systems 9

2.3 Aircraft Model Overview 12

2.3.1 Inner Loop Model – Specific Forces and Moments 13

2.3.2 Outer Loop Model – Point Mass Kinematics 19

2.3.3 Non-Linear Simulation 22
Chapter 3 23
System Identification Methods 23
3.1 Parameter Estimation Models 24
3.1.1 Fisher Model 25
3.1.2 Least-Squares Model 29
3.1.3 Model Choice 31
Chapter 4 32
Applying Regression Techniques 32
4.1 Input-Output Equations 32
4.2 Recursive Implementation 35
4.2.1 Recursive Least Squares (RLS) 35
4.2.2 Exponential Forgetting Method 36
4.2.3 Covariance Resetting 37
4.3 Pre-processing Flight Data 37
4.3.1 Measurement Errors 37
4.3.2 Data Consistency Check 41
4.3.3 Sensor bias determination 44
Chapter 5 49
Parameter Identifiability 49
5.1 Modeling Errors 49
5.2 Estimate Statistics 50
5.2.1 Scaling 51

5.2.2 Data Collinearity 52
5.2.3 Model fit statistics 54
5.3 Optimal Input Design 55
5.3.1 Types of inputs 55
5.3.2 Natural Frequencies 61
5.3.3 Considerations 64
Chapter 6 65
Angle of Attack Estimation and Sensing 65
6.1 Sensor Design 65
6.1.1 Probe Design 68
6.1.2 Avionics and Sensors 69
6.2 AoA Calibration 72
6.2.1 Calibration Procedure Overview 72
6.2.2 Formulation of the Calibration Curves 73
6.2.3 Wind-Tunnel Setup 73
6.2.4 Calibration Results 76
6.2.5 Summary 79
6.3 Estimator Development 81
6.3.1 Aerodynamic Based Estimator 81
6.3.2 The Kinematic Based Estimator 97
6.3.3 Estimator Choice 97
Chapter 7 98
Angular Acceleration Determination 98
7.1 Numerical Differentiation 98

7.1.1 Central Difference formulation 98
7.1.2 Smoothed Differentiators 99
7.1.3 Other Methods 101
7.1.4 Practical Problems 103
7.2 Distributed Sensors 104
Chapter 8 108
System Identification Simulation Results 108
8.1 Non-Linear Simulation: Short Period Mode 108
8.1.1 Aircraft parameters 109
8.1.2 Control Inputs 110
8.1.3 Data Consistency Check 115
8.1.4 Bias Estimation 117
8.1.5 Estimation of Angular Accelerations 124
8.1.6 AoA estimation 127
8.1.7 Parameter Estimation: Short Period mode 128
8.2 Conclusion 134
Chapter 9 135
Estimation from Flight Test Data 135
9.1 Prior Parameter Estimates 135
9.2 Kinematic consistency and Data check 137
9.3 Bias estimation 138
9.4 AoA measurement 144
9.5 Angular Acceleration Estimation 145
9.6 Parameter Estimation 146

9.7 Conclusion 150
Chapter 10 151
Summary and Recommendations 151
10.1 Summary 151
10.2 Recommendations 154
11 Bibliography 155
12 Appendix A: Flight Data (Sampioen) 159
13 Appendix B: Output Error Method 163

List of Figures

Figure 1: A 3D model of the Modular UAV 2
Figure 2: FTC Architecture Overview [2] 3
Figure 3: Fault Detection and Isolation Block Expanded [2] 5
Figure 4: North East Down Axis System [1] 10
Figure 5: Aircraft Body Axis 10
Figure 6: Wind axis transformation wrt Body coordinate system (Zipfel, 2006) 11
Figure 7: Aircraft Overview [3] 12
Figure 8: Simulink® Model used for simulation 22
Figure 9: Details of Implemented Filter Error method for linear systems 28
Figure 10: Deterministic Measurement Errors (Tischler, 2006) 39
Figure 11: Non-deterministic Measurement Errors (Tischler, 2006) 40
Figure 12: Energy Spectra of pulse inputs (Jategoankar, 1996) 56
Figure 13: Energy Spectra of doublet inputs(Jategoankar, 1996) 58
Figure 14: Normalized Energy Spectra of a Doublet (Jategoankar, 1996) 59
Figure 15: Energy Spectra Comparison (Jategoankar, 1996) 60
Figure 16: Pivoted Vane for AoA sensing 66
Figure 17: Illustration of a differential pressure probe 67
Figure 18: AoA probe mounted on the aircraft 68
Figure 19: Overview of the Avionics used for AoA Sensoring 69
Figure 20: Conceptual operation of CANSense Pressure board 69
Figure 21: Pressure Sense board and OBC 70
Figure 22: Flow diagram of AoA calibration procedure 72
Figure 23: Wind-tunnel with variable speed drive 74
Figure 24: Calibration setup 74
Figure 25: AoA calibration rig in the wind-tunnel 75
Figure 26: Calibration Curves 76
Figure 27: Final calibration curve 77
Figure 28: Calibration curves zoomed in about $\Delta P=0$ 78

Figure 29: Variation in pressure readings at 10deg 79
Figure 30: AoA estimator Simulink Simulation 90
Figure 31: AoA estimator with pitch rate bias 91
Figure 32: AoAEstimtor with bias estimation and pitch rate bias added 92
Figure 33: AoA estimation using PIKF and added pitch rate bias 93
Figure 34: AoA estimator with CLa error 94
Figure 35: AoA Estimtor with bias estimation and pitch rate bias added 95
Figure 36: AoA estimation using PIKF withCLa error 96
Figure 37: Fitting a polynomial to 3 points 99
Figure 38: Magnitude response of Savitzky-Golay filters [41] 101
Figure 39: Magnitude response of Smooth Robust differentiators [41] 102
Figure 40: Illustration of distributed sensoring 104
Figure 41: Simulink Model for distributed sensing 106
Figure 42: Comparison of distributed sensors and numerical differentiation 107
Figure 43: Short Period mode excitation 112
Figure 44: Roll mode excitation 113
Figure 45: Dutch roll mode excitation 115
Figure 46: Output of FPR comparison 116
Figure 47: FPR after bias estimation (without AoA and AoS measurements) 118
Figure 48: Measured variables for bias estimation 120
Figure 49: FPR after bias estimation (with AoA measurement) 122
Figure 50: Angular accelerations as determined by ndiff08 124
Figure 51: Differentiation with 11th order smoothing filter 125
Figure 52: Actual vs Estimated angular accelerations 126
Figure 53: AoA estimate using FPR 127
Figure 54: Time history of Pitch moment coefficients 130
Figure 55 : Time history of the Lift coefficients 133
Figure 56: FPR applied to Flight Data 137
Figure 57: FPR on Flight Data after bias estimation 139
Figure 58: FPR for time period 2 142
Figure 59: AoA measurement analysis 144

Figure 60: Angular accelerations determined through numerical differentiation 145
Figure 61: Pitching Moment Coefficients 146
Figure 62: Measured Pitch Rate Response 148
Figure 63: Elevator Response for time period 2 149
Figure 64: Accelerometer Measurements (Sampioen) 159
Figure 65: Gyroscope measurements (Sampieon) 160
Figure 66: Measured Attidtude Angles (Sampioen) 161
Figure 67: Airspeed Measurements (Sampioen) 162
Figure 68: Details of implemented output error method 163

List of Tables

Table 1: AoA calibration speeds 76
Table 2: AoA curve statistics 78
Table 3: Savitzky-Golay Filter (M=2) 100
Table 4: Modular UAV Physical Specifications 109
Table 5: Modular UAV Stability Derivatives 110
Table 6: Modular UAV Control Derivatives 110
Table 7: Estimated Biases excluding AoA and AoS measurements 117
Table 8: Measured variables with correlation greater than 0.9 119
Table 9: Estimated Biases including AoA measurements 121
Table 10: Estimation of pitching moment coefficients (Q_dot determined by means of numerical differentiation) 129
Table 11: Estimation of pitching moment coefficients (modified Q_dot) 130
Table 12: Estimated lift coefficient comparison 132
Table 13: Estimated Lift Coefficient using accurate AoA estimates 132
Table 14: Sampioen Aircraft Parameters 136
Table 15: Bias Estimates from Flight Data 138
Table 16: Bias Estimates for time period 2 140
Table 17: Bias comparison 141
Table 18 : Comparison of AVL and Estmimated Pitching Moment Coefficients 147

Nomenclature

Greek Letters

α	Angle of Attack
β	Sideslip angle
δ_A	Aileron deflection
δ_e	Elevator deflection
δ_R	Rudder deflection
δ_T	Throttle input
ϕ	Roll angle
ρ	Air density
λ	Forgetting factor
$\mathbf{\Sigma}$	Specific acceleration vector
Θ	Vector of Parameters
$\widehat{\Theta}$	Vector of Estimated Parameters
θ	Pitch angle
ψ	Yaw angle

Lowercase Letters

a_x	Accelerometer in the x body axis
a_y	Accelerometer in the y body axis
a_z	Accelerometer in the z body axis
b	Wing span
c	Chord length
e	Oswald efficiency factor
m	Aircraft mass
p	Roll rate perturbation
q	Pitch rate perturbation
r	Roll rate perturbation
y	Observation vector
z	Measurement vector

Uppercase Letters

AR	Aspect ratio
C_D	Aerodynamic drag coefficient
C_l	Aerodynamic roll moment coefficient
C_L	Aerodynamic lift coefficient
C_m	Aerodynamic pitching moment coefficient

C_n	Aerodynamic yaw moment coefficient
C_X	Aerodynamic axial force coefficient
C_Y	Aerodynamic lateral force coefficient
C_Z	Aerodynamic normal force coefficient
$\boldsymbol{F}$	Vector of forces
$\boldsymbol{H}$	Matrix of Regressors
$\boldsymbol{I}$	Inertial matrix
L	Rolling moment
M	Pitching moment
N	Yaw moment
P	Total Roll rate
Q	Total Pitch rate
R	Total Yaw rate
S	Wing area
X	Axial force
Y	Lateral Force
Z	Normal force

Subscript

0	Trim values
A	Aerodynamic
B	Body axes
I	Inertial axes
S	Stability axes
W	Wind axes

Superscript

BI	Body axes with respect to the inertial axes
BW	Body axes with respect to the wind axes
WI	Wind axes with respect to the inertial axes

Acronyms

AVL	Athena Vortex Lattice
FDI	Fault Detection and Isolation
FPR	Flight Path Reconstruction
FTC	Fault Tolerant control
ML	Maximum Likelihood
UAV	Unmanned Aerial Vehicle
WLS	Weighted Least Squares

Chapter 1

Introduction and Overview

1.1 Background

Unmanned aerial vehicles (UAV's) have been around and in service for decades (even before the 1960's) performing missions such as border patrol, forest monitoring, inspection of power lines and homeland security, amongst other intelligence, surveillance and reconnaissance (ISR) missions. Though in recent years UAV usage has increased, there is still a general concern with regards to the safety and reliability of operating a UAV.

To increase the reliability of UAV systems, many techniques have been researched. Among these techniques is a branch of techniques called Fault Tolerant Control (FTC). FTC is a control technology that allows a UAV to operate safely in the presence of system component failures or faults.

Fault tolerant control can be broken up into two main categories namely,

1. Passive fault tolerant control, and
2. Active fault tolerant control.

The main difference between these two branches of techniques is that the passive branch of techniques deal with designing a flight control system that is robust enough to deal with a certain degree of uncertainty or faults in the system, whereas active fault control techniques aim to determine or isolate a fault (or faults) in the system, and then reconfigure the flight controller such that the flight controller adapts to this fault. In passive methods the flight controller prior to a fault is the same controller as after a fault or failure has occurred. Active fault tolerant control, however, deals with the reallocation of control of the actuators in the presence of a fault. In this case, the control law is actively changing to adapt to a fault, such as to carry out the necessary control functions required. For both these categories system redundancy is required to ensure safe flight after a fault has occurred.

This project forms part of a larger joint project done by postgraduate students at the University of Stellenbosch. The joint project investigates the implementation of FTC on the Modular UAV aircraft, designed by the CSIR (Council for Scientific and Industrial Research). This research focuses primarily on the Single Failure Survivability (SFS) of the Modular UAV aircraft, with focus particularly on aircraft actuator faults. The Modular UAV is chosen as the platform to test FTC because of the built-in redundancy of the aircraft. The Modular UAV, as shown in Figure 1, has two fuselages, two engines, two rudders, a set of ailerons, a set of flaps and an elevator.

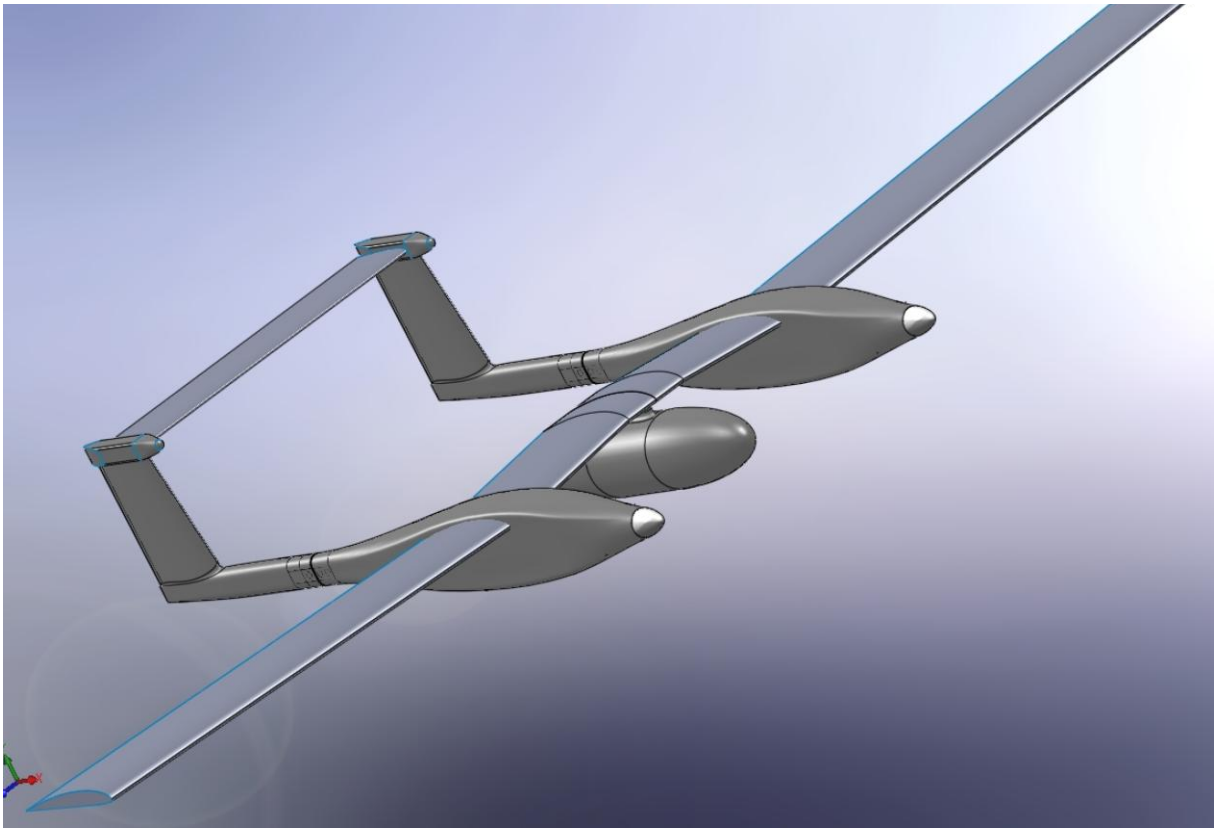

Figure 1: A 3D model of the Modular UAV

.

The FTC architecture used for the Modular UAV research, as described in [1, 2], is illustrated in Figure 2.

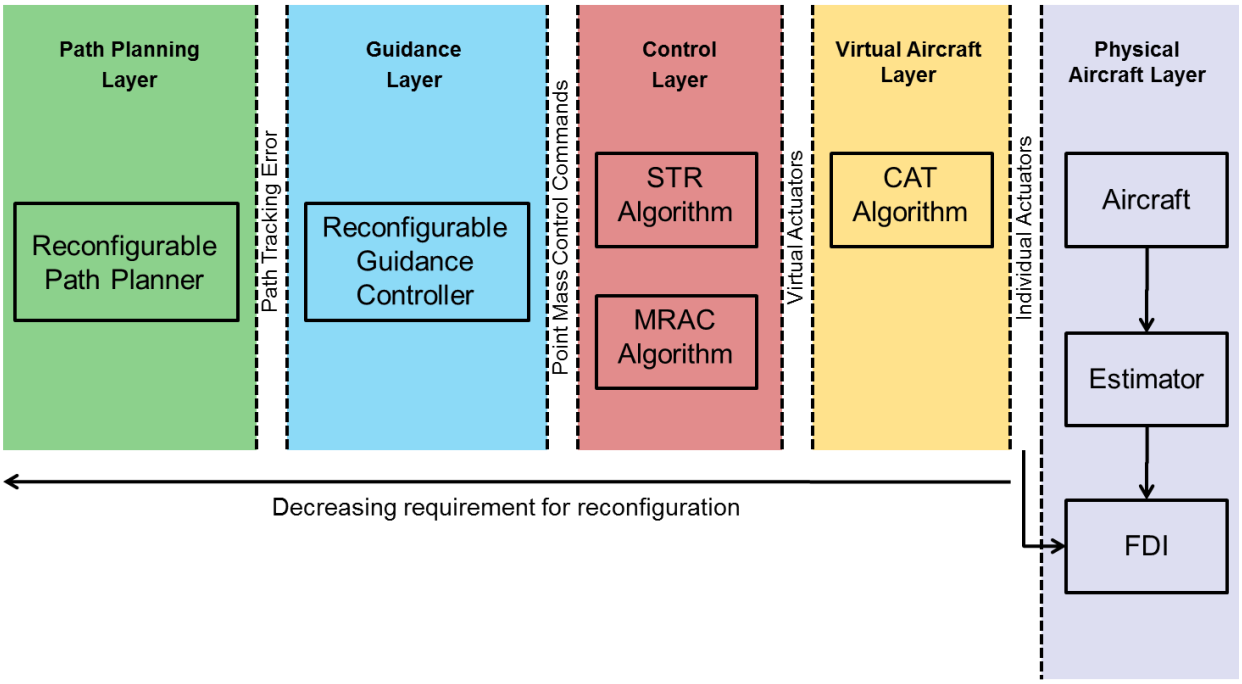

Figure 2: FTC Architecture Overview [2]

As illustrated in the figure above, the architecture used for FTC at the University of Stellenbosch, comprises of 5 entities or layers. These layers are described below:

- The *Physical Aircraft Layer* represents the physical aircraft with its actuators, measured states as well as its estimated states. The FDI or Fault Detection and Isolation block is responsible for determining and quantifying any changes to the physical configuration of the aircraft.
- The *Virtual Aircraft Layer* provides a simple mathematical representation (or mathematical model) of the physical aircraft to the *Control Layer*. This layer also provides the link between the *Virtual Actuators* (as commanded by the *Control Layer*) and the actuators of the physical aircraft (*Individual Actuators*). Current research at the University of Stellenbosch includes research into reconfiguring the actuator commands at this level (Control Allocation Techniques, CAT) to accommodate for actuator faults. Here, simple fixed gain controllers can be used in the *Control Layer*, as the reconfiguration for FTC happens in the *Virtual Aircraft Layer*.

- The *Control Layer* is responsible for the stabilization of the aircraft. Reconfiguration at this level, in the presence of a fault, is made possible through the use of MRAC (Model Reference Adaptive Control) and STR (Self Tuning Regulators). These techniques, amongst others, make the *Control Layer* adaptable to changes in the model, provided by the *Virtual Aircraft Layer*.
- "The Guidance Layer is responsible for guiding the aircraft back onto a kinematically feasible path given by the Path Planning Layer through the path tracking error. It then interfaces with the control layer through kinematic virtual actuators," [2].
- The outer Path Planning Layer provides kinematically feasible paths to the guidance layer. In this architecture used at the University of Stellenbosch, little to no reconfiguration, due to faults, occur at this level.

This thesis, as part of the FTC research at the University of Stellenbosch, investigates the implementation of System Identification algorithms (SID) for FTC of a UAV, with the view of implementing the algorithms in real-time. The research in this thesis thus focuses specifically on the Physical Aircraft Layer within this architecture, but more specifically, the FDI (Fault Detection and Isolation) block within this layer.

System Identification provides a means to determine and quantify a fault (i.e. fault detection) within the system. The information provided by the System Identification algorithms, the stability and control derivatives of the aircraft (hereafter also referred to as the aircraft parameters), are the parameters that make up the aircraft model in the Virtual Aircraft layer. The FDI block including System Identification can be seen as one of the first steps in FTC and is illustrated below:

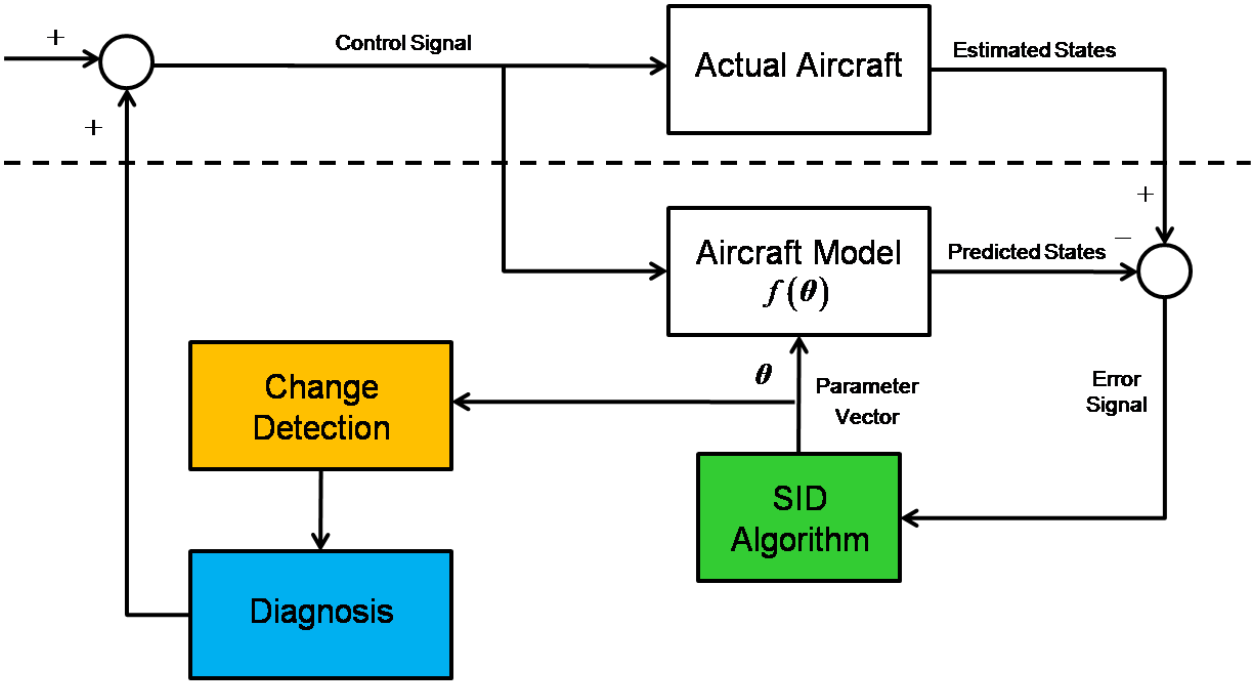

Figure 3: Fault Detection and Isolation Block Expanded [2]

Here the operation of the System Identification (SID) algorithm in the FTC architecture is made evident. In the event of a fault or failure, the model response (the *Virtual Aircraft model response*) and the actual response of the physical aircraft differ. This error is detected by the SID algorithm and a new set of model parameters are estimated, as to minimize this error. The change in aircraft parameters is then detected and diagnosed. In this diagnosis, the change in model parameters is related to a fault or failure. The source of the fault is identified and quantified and the necessary control inputs are provided by this block. This information is also used in the *Virtual Aircraft Layer* and *Control Layer* for reconfiguration of the actuators or flight controllers.

1.2 System Identification Background and Overview

System Identification (SID) can be described as a procedure to match the input-output response of a dynamic system by means of a proper choice of an input-output model and the physical parameters associated with this model. Simply put, it is a method used to develop a model that correctly describes the input-output relationship of a dynamic system.

In its application to aircraft, SID techniques have focused mainly on the field of Parameter Estimation (PEST). The main reason behind this is that the aerodynamic model of aircrafts is fairly well defined, and thus just the parameters that make up the model are of interest. Having said this, it must be noted that the complexity of the aerodynamic model used in Parameter Estimation is determined by the required accuracy of the model and is also limited by the amount and type of sensors that are available on the aircraft.

Much research has already been done into developing Aircraft System Identification and Aircraft Parameter Estimation techniques. Approaches for determining the static and dynamics parameters of aircrafts from flight data were developed as early as 1947, when Miliken (1947), published his works on "*Progress in stability and control research*". In this paper he focused on frequency response data and used a simple semi-graphical method for his analysis. In the years that followed, more general and rigorous ways to determine aerodynamic parameters from transient maneuvers were established through works done by Greenberg (1951) and Shinbrot (1951).

With the availability of digital computers increased since the time of Miliken, vast improvements in the field of aircraft aerodynamic modeling and parameter estimation was realized. An extensive bibliography of works related to Aircraft Parameter Estimation was published by Iliff and Maine (1986). This bibliography provides a source of potential references for any study into Aircraft Parameter Estimation.

Though this bibliography contains references to sources that focus on specific areas within aircraft parameter estimation, more broad overviews of aircraft system identification can be found in the works [8, 9, 10, 11, 12, 13].

1.3 Thesis Outline

This document starts off with Chapter 2 describing the aircraft model used in the analysis presented in this thesis. The chapter describes the inner-loop and outer-loop models that make up the 6 degree of freedom aircraft model. The inner-loop model, being the model that describes the specific forces and moments acting on the aircraft, and the outer-loop model which handles the point mass kinematics.

Chapter 3 gives a brief overview of the different system identification methods that were considered. It starts off by introducing 3 different models that could be used when performing system identification and then describes the general system identification approaches linked to each model.

Chapter 4 goes into more detail into one of the approach's described in chapter 3, specifically the Least-Square method (or Regression analysis). The chapter explores the method of applying the regression analysis to determine the aircraft parameters.

Chapter 5 covers the issue of parameter identifiability; how good the aircraft parameter estimates represent the true parameters. The chapter introduces methods and techniques to determine the accuracy of the estimates as well as methods to increase the probability of getting good parameter estimates.

Chapter 6 discusses methods of obtaining Angle-of-Attack (AoA) measurements. The chapter starts off with the design and calibration of a sensor made for purposes of this thesis. This is followed by describing methods that can be used to determine the AoA with existing instrumentation on the aircraft at the ESL.

Chapter 7 discusses methods of obtaining angular acceleration measurements. Two approaches are described, one being obtaining them through numerical differentiation, and the other by means of distributed sensors. The chapter describes the pros and cons of the different methods as well as the means of implementing them on an aircraft.

Chapter 8 shows how the methods introduced in the previous chapters are applied to a non-linear aircraft simulation. The analysis focuses specifically on the estimation of the aircraft parameters linked to the short-period mode and highlights the different issues that can be experienced when using actual flight data.

Chapter 9 shows the analysis performed on actual flight data. The chapter highlights the problems experienced during the analysis, and provides recommendations for further flight tests.

The document concludes with Chapter 10 summing up the issues presented in this thesis and provides recommendations for further works in the field of system identification.

Chapter 2

Aircraft Dynamics

2.1 Introduction

In this chapter the aircraft model used for simulation in this thesis is derived. The full derivation is not covered in this section as only the necessary information required for the understanding of the topic is presented. A full derivation of the classical longitudinal and lateral aircraft dynamics can be found in [1, 14, 15, 16 and 28].

2.2 Coordinate Systems and Notation

For the effective modeling of an aircraft a number of coordinate systems are required. These coordinate systems or axes are presented in this section.

2.2.1 Coordinate Systems

The following subsections define the axes needed for modeling purposes.

a. Inertial and Earth Axes

Newtonian mechanics can only be applied within an inertial reference frame and its corresponding axis system. Though the Earth or North-East-Down (NED) axis system is not inherently an inertial axis system, it can be approximated as one. For typical UAV applications the NED axis system assumes a non-rotating flat earth, which for all practical purposes can be assumed to be inertial.

The NED axis system is defined as follows (Figure 4):

1. The origin of the NED-axis system is chosen to coincide with a chosen reference point on the earth's surface. This is normally chosen to coincide with a point on the runway.
2. The x-axis (X_E) points in a northerly direction, the y-axis (Y_E) in an easterly direction and the z-axis (Z_E) completes the right handed orthogonal axis system and points towards the center of the earth.

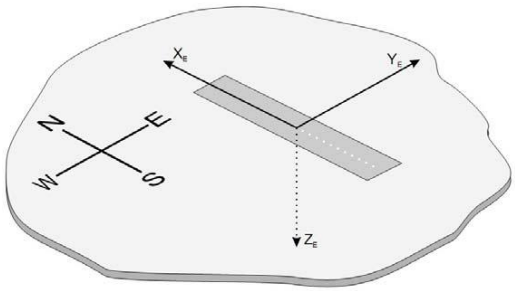

Figure 4: North East Down Axis System [1]

b. Body Axes

The body axis system is the coordinate system aligned with the aircrafts airframe. This coordinate system is particularly important as all the avionics and instrumentation, as well as the control surfaces of the aircraft are coordinated within this axis system.

The body axes are defined as follows (Figure 5):

1. The origin of the axes is chosen to coincide with the center of mass of the aircraft
2. The x-axis (X_B) lies in the plane of symmetry and points through the nose of the aircraft.
3. The y-axis (Y_B) lies perpendicular to the plane of symmetry and points in the direction of the right wing.
4. The z-axis (Z_B) completes the right handed orthogonal axis system and points downwards.

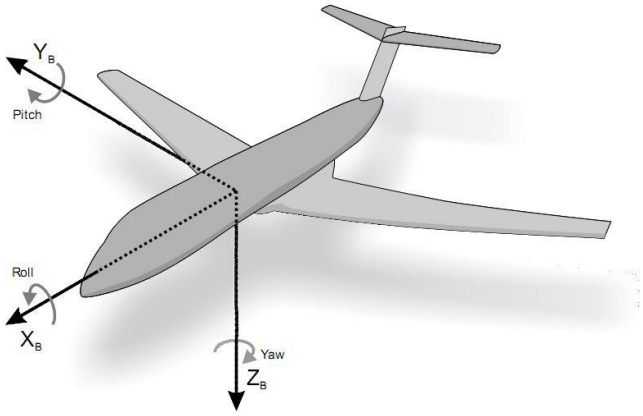

Figure 5: Aircraft Body Axis

c. Wind and Stability Axes

During flight, an aircraft experiences a relative wind over its body which gives rise to the aerodynamic forces experienced by the aircraft. A wind axis system is thus introduced; whose origin is aligned with the center of mass and its x-axis (X_W) is parallel and in the direction of the velocity vector of the center of mass of the aircraft.

To understand the orientation of the wind axes, it is best to describe it through its transformation from the body axes. Two angles are used to relate the orientation of the body axes to the wind axes; these angles are the angle of attack (α) and angle of sideslip (β) respectively.

The transformation is as follows:

1. The body axis is pitched negatively by α about the Y_B-axis. The resulting intermediate axis system is commonly referred to as the Stability Axes.
2. The Wind axis is then obtained by positively yawing the Stability axis about the Z_S-axis by the angle β.

This transformation is shown graphically in Figure 6.

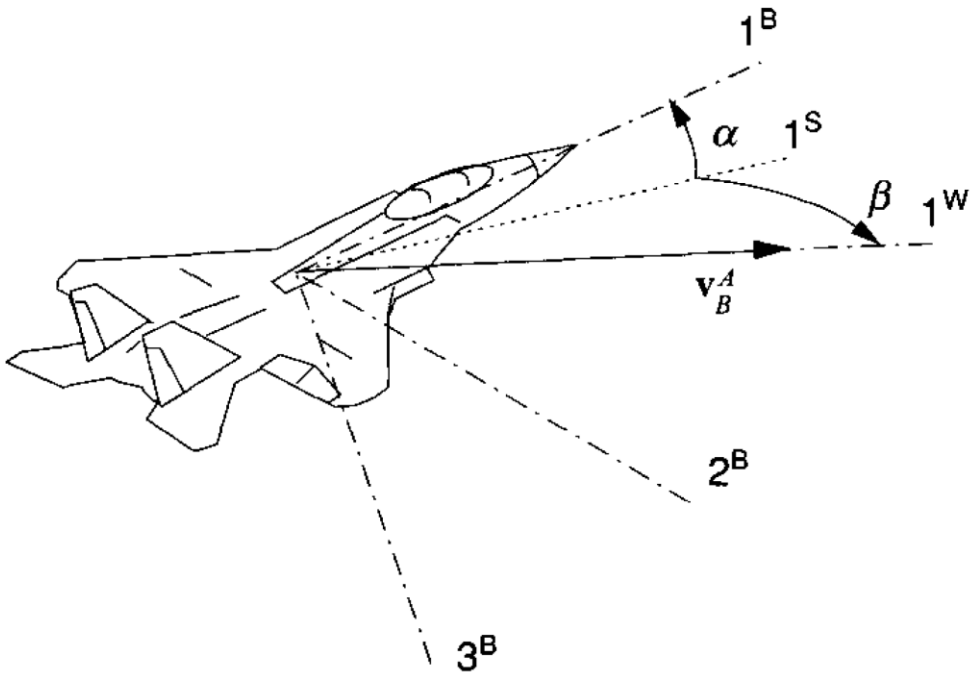

Figure 6: Wind axis transformation wrt Body coordinate system (Zipfel, 2006)

In Figure 6, the superscript B represents the Body coordinate system; the superscript S, the stability coordinate system and the superscript W, the Wind coordinate system. The figure has been obtained from Zipfel (2006); in this text $(1^B, 2^B, 3^B)$ is equivalent to (X_B, Y_B, Z_B).

2.3 Aircraft Model Overview

This section investigates the equations of motion for a rigid aircraft. An aircraft is well modeled as a six degree of freedom rigid body. The six degrees of freedom include 3 translational and 3 rotational degrees of freedom.

Aircraft dynamics, though coupled and non-linear in nature, can be simplified through a process called time-scale separation. The full aircraft model consists of a slower set and a faster set of dynamics. The faster or higher frequency dynamics being the angular rotations between the aircraft's body axes and the wind axes, whereas the slower or lower frequency dynamics, are the attitude and velocity dynamics of the aircraft relative to inertial space. The process of time-scale separation is touched on in this thesis but is explained in Peddle (2008).

The aircraft model used in this thesis separates these dynamics into two separate but linked models. The faster dynamics are put into an Inner Loop Model. This model includes the specific forces and moments that act on the aircraft body. The slower dynamics, or Outer Loop Model, contain the slower attitude dynamics of the aircraft. These two models are illustrated in Figure 7.

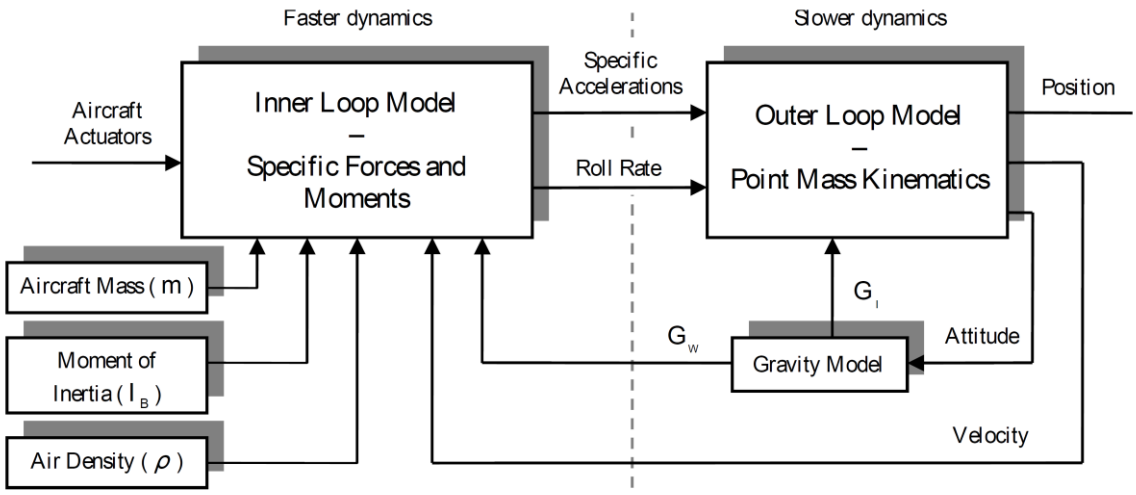

Figure 7: Aircraft Overview [3]

2.3.1 Inner Loop Model – Specific Forces and Moments

As mentioned earlier, the inner loop model encompasses the specific forces and moments acting on the aircraft. These forces and moments acting on the aircraft provide dynamic equations that relate the angular motion of the aircraft's body axes relative to its wind axes.

a. Rigid Body Rotational Dynamics

Modeling the aircraft as a rigid body implies that the dynamic effects due to structural deformation and the relative motion of the control surfaces are assumed to have negligible effect on the dynamics of the aircraft.

For the rest of this section the following assumptions have been made:

1. The aircraft is a rigid body symmetric about its XZ-plane, with constant mass
2. The earth is fixed in inertial space and is regarded as flat

The dynamic equations that describe the rotational dynamics of the aircraft's body axes relative to the aircrafts wind axes is derived through the transformation between the these two axis systems.

As described in Section 2.2.1, the orientation of the wind axes is defined by two rotations relative to the body axes. The transformation consists of a negative rotation through the angle of attack (α), followed by a positive rotation through the angle of sideslip (β). According to Gaum (2009), the attitude dynamics of the wind axes relative to the body axes, given the body axes angular rates and wind axes forces, can be expressed as:

$$\begin{bmatrix} \dot{\alpha} \\ \dot{\beta} \\ P_W \end{bmatrix} = \begin{bmatrix} -\cos\alpha\tan\beta & 1 & -\sin\alpha\tan\beta \\ \sin\alpha & 0 & -\cos\alpha \\ \cos\alpha\sec\beta & 0 & \sin\alpha\sec\beta \end{bmatrix} \begin{bmatrix} P \\ Q \\ R \end{bmatrix} + \frac{1}{m\bar{V}} \begin{bmatrix} \sec\beta & 0 \\ 0 & 1 \\ \tan\beta & 0 \end{bmatrix} \begin{bmatrix} Z_w \\ Y_W \end{bmatrix} \tag{2.1}$$

Note that the first two equations represent the attitude dynamics of the wind axes relative to the body axes, while the third equation provides a constraint that ensures the wind axes normal vector is in the aircrafts plane of symmetry.

In order to write the attitude dynamics of the wind axes in terms of the applied forces and moments, the dynamics of the angular rates in the above equation have to be obtained. Euler's law for rigid bodies states that the time derivative relative to the inertial reference frame of an objects angular momentum ($\mathbf{H_I}$), referenced to its center of mass, is equal to the externally applied moment ($\mathbf{M_I}$).

$$\boldsymbol{M} = \frac{d}{dt}\boldsymbol{H}\Big|_I \tag{2.2}$$

The time derivative of Equation 2.2 can be transformed to the aircraft's body axes using the Coriolis equation.

$$\boldsymbol{M} = \frac{d}{dt}\boldsymbol{H}\Big|_B + \boldsymbol{\omega}^{BI} \times \boldsymbol{H} \tag{2.3}$$

Equation 2.3 is as a result of the body axes not being an inertial frame. With the angular momentum coordinated into the body axes, the angular momentum vector is given by Gaum (2009) as,

$$\boldsymbol{H}_B = \boldsymbol{I}_B \boldsymbol{\omega}_B^{BI} \tag{2.4}$$

With $\boldsymbol{I}_B$ being the moment of inertia tensor referenced to the body axis system. Equation 2.3 can now be coordinated into the body axes and Equation 2.4 substituted for the angular momentum vector to yield,

$$\dot{\boldsymbol{\omega}}_B^{BI} = \boldsymbol{I}_B^{-1}\left(\boldsymbol{M}_B - \boldsymbol{S}_{\boldsymbol{\omega}_B^{BI}} \boldsymbol{I}_B \boldsymbol{\omega}_B^{BI}\right) \tag{2.5}$$

In the above equation $\boldsymbol{S}_{\boldsymbol{\omega}_B^{BI}}$ is the skew-symmetric form of $\boldsymbol{\omega}_B^{BI}$ given by Equation B.2.2, used to represent the cross product.

Expanding equation (2.5) and combining it with Equation 2.1, the full rigid body rotational dynamics is derived.

$$\begin{bmatrix} \dot{\alpha} \\ \dot{\beta} \\ P_W \end{bmatrix} = \begin{bmatrix} -\cos\alpha\tan\beta & 1 & -\sin\alpha\tan\beta \\ \sin\alpha & 0 & -\cos\alpha \\ \cos\alpha\sec\beta & 0 & \sin\alpha\sec\beta \end{bmatrix} \begin{bmatrix} P \\ Q \\ R \end{bmatrix} + \frac{1}{m\bar{V}} \begin{bmatrix} \sec\beta & 0 \\ 0 & 1 \\ \tan\beta & 0 \end{bmatrix} \begin{bmatrix} Z_w \\ Y_W \end{bmatrix} \tag{2.6}$$

$$\begin{bmatrix} \dot{P} \\ \dot{Q} \\ \dot{R} \end{bmatrix} = \boldsymbol{I}_B^{-1} \left(\begin{bmatrix} L_B \\ M_B \\ N_B \end{bmatrix} - \begin{bmatrix} 0 & -R & Q \\ R & 0 & -P \\ -Q & P & 0 \end{bmatrix} \boldsymbol{I}_B \begin{bmatrix} P \\ Q \\ R \end{bmatrix} \right) \tag{2.7}$$

Here L_B, M_B and N_B represents the moments about the X_B, Y_B and Z_B axes. The equations above include the constraint (as shown below), that ensures orthoganality.

$$P_W = [\cos\alpha\sec\beta \quad 0 \quad \sin\alpha\sec\beta] \begin{bmatrix} P \\ Q \\ R \end{bmatrix} + \frac{1}{m\bar{V}} [-\tan\beta \quad 0] \begin{bmatrix} Z_W \\ Y_W \end{bmatrix} \tag{2.8}$$

b. Specific Forces and Moments

This section investigates the specific forces and moments on the aircraft. The specific forces are all the forces acting on the aircraft, except for gravity. The specific forces can thus be defined as the sum of the aerodynamic forces acting on the aircraft and the thrust forces.

Aerodynamic Forces

The aerodynamic forces and moments acting on a rigid aircraft are the most complex to model and introduce most of the uncertainty into the aircraft model. This is due to the very nature of the aerodynamic coefficients, which are non-linear functions of several variables.

In this text the linear form of the Taylor's series formula will be considered, which implies that the second-order and higher-order partial derivatives will be ignored. Provided that the stall regions are not considered, wind-tunnel data has shown that this approximation is valid for many aircrafts Schmidt (1998).

Expanding the various coefficients for typical subsonic, pre-stall flight yields:

***Drag* (C_D), *Lift* (C_L) *and Side force* (C_y) coefficients:**

$$C_D = C_{D_0} + \frac{C_L^2}{\pi A e} \tag{2.9}$$

$$C_L = C_{L_0} + C_{L_\alpha}\alpha + \frac{\bar{c}}{2\bar{V}} C_{L_Q} Q + C_{L_{\delta_E}}\delta_E \tag{2.10}$$

$$C_y = C_{y_\beta}\beta + \frac{b}{2\bar{V}} C_{y_P} P + \frac{b}{2\bar{V}} C_{y_R} R + C_{y_{\delta_A}}\delta_A + C_{y_{\delta_R}}\delta_R \tag{2.11}$$

***Roll* (C_l), *Pitch* (C_m) *and Yaw* (C_y) moment coefficients**

$$C_l = C_{l_\beta}\beta + \frac{b}{2\bar{V}} C_{l_P} P + \frac{b}{2\bar{V}} C_{l_R} R + C_{l_{\delta_A}}\delta_A + C_{l_{\delta_R}}\delta_R \tag{2.12}$$

$$C_m = C_{m_0} + C_{m_\alpha}\alpha + \frac{\bar{c}}{2\bar{V}} C_{m_Q} Q + C_{m_{\delta_E}}\delta_E \tag{2.13}$$

$$C_n = C_{n_\beta}\beta + \frac{b}{2\bar{V}} C_{n_P} P + \frac{b}{2\bar{V}} C_{n_R} R + C_{n_n}\delta_A + C_{n_{\delta_R}}\delta_R \tag{2.14}$$

where C_{D_0}, C_{L_0}, and C_{m_0} are the parasitic drag, static lift and static pitching moment coefficients respectively. A is the aspect ratio of the wing, $\bar{c}$ is the mean aerodynamic chord, b is the wing span and e is the Oswald efficiency factor (which lies between 0.8 and 0.95 for conventional subsonic aircraft, (Schmidt, 2008).

The non-dimensional stability and control derivatives have the form:

$$C_{A_B} \equiv \frac{\partial C_A}{\partial B'} \tag{2.15}$$

where

$$B' = n_c B, \tag{2.16}$$

and n_c is the normalizing coefficient of B. The normalizing coefficient for pitch rate is $\frac{\bar{c}}{2\bar{V}}$, whereas for the roll and yaw rates it is $\frac{b}{2\bar{V}}$. The angles of incidence as well as the control surface deflections all have a unity normalizing coefficient.

It must be noted that the non-dimensional stability and control derivatives are calculated about a certain aircraft trim condition and thus the states (α, β, P, Q, R) as well as the control surface deflections $(\delta_E, \delta_A, \delta_R)$ used in this section are the sum of the trim states plus the perturbations about this trim condition. In addition to this, the non-dimensional stability and control derivatives are all coordinated with respect to the wind axes.

Aerodynamic force and moments

The aerodynamic force and moment contributions, coordinated in the wind axes, can thus be expanded as follows:

$$X_W^A = -qSC_D \tag{2.17a}$$

$$Y_W^A = qSC_y \tag{2.17b}$$

$$Z_W^A = -qSC_L \tag{2.17c}$$

$$L_W^A = qSbC_l \tag{2.18a}$$

$$M_W^A = qS\bar{c}C_m \tag{2.18b}$$

$$N_W^A = qSbC_n \tag{2.18c}$$

where q is the dynamic pressure, S is the wing area, b is the wing span and $C_{(.)}$ are the non-dimensional aerodynamic coefficients expressed in the wind axes. Substituting Equations 2.9 to 2.14 into Equations 2.17a to 2.18c, the Equations expressing the aerodynamic forces on the aircraft as a function of the angles, angular rates and control surface deflections can be determined.

The aerodynamic model presented in this section provides the forces and moments acting on the aircraft in the wind axes. The forces and moments acting on the aircraft are, however, required in the body axes (as per equation 2.4). This transformation between the wind axes and body axes can be achieved through the $\mathbf{DCM}^{\mathrm{BW}}$ transformation matrix.

$$\boldsymbol{M}_B = \boldsymbol{DCM}^{BW}\boldsymbol{M}_W \tag{2.19}$$

Where $\boldsymbol{DCM}^{BW}$ is given by [17]:

$$\boldsymbol{DCM}^{BW} = \begin{bmatrix} \cos\alpha\cos\beta & -\cos\alpha\sin\beta & -\sin\alpha \\ \sin\beta & \cos\beta & 0 \\ \sin\alpha\cos\beta & -\sin\alpha\sin\beta & \cos\alpha \end{bmatrix} \tag{2.20}$$

The transformations that make up the DCM matrix can be found in Zipfel (2006).

Thrust Forces

Assuming that the trust vector lies along the body axis X_B, which is the case for the UAVs used at the ESL (Electronics System Lab), the following thrust model holds:

$$X^T = T, \qquad Y^T = Z^T = 0 \tag{2.21}$$

$$L^T = M^T = N^T = 0, \tag{2.22}$$

Though complex propulsion models do exist, a first order lag model tends to be sufficient for most UAV applications. This first order lag models the band-limited nature of most propulsion sources and is provided below [2]:

$$\dot{T} = -\frac{1}{\tau}T + \frac{1}{\tau}T_c \tag{2.23}$$

where T is the thrust magnitude, T_c is the thrust command and the engine lag time is denoted by τ.

Total specific forces and moments

The total specific forces (X_W, Y_W, Z_W) and moments (L_W, M_W, N_W) acting on the aircraft, coordinated in the wind axes, are given by,

$$\begin{bmatrix} X_W \\ Y_W \\ Z_W \end{bmatrix} = qS \begin{bmatrix} -C_D \\ C_y \\ -C_L \end{bmatrix} + \begin{bmatrix} \cos\alpha\cos\beta \\ \cos\alpha\sin\beta \\ \sin\alpha \end{bmatrix} T \tag{2.24}$$

$$\begin{bmatrix} L_W \\ M_W \\ N_W \end{bmatrix} = qS \begin{bmatrix} b & 0 & 0 \\ 0 & \bar{c} & 0 \\ 0 & 0 & b \end{bmatrix} \begin{bmatrix} C_l \\ C_m \\ C_n \end{bmatrix} \tag{2.25}$$

with the dynamic pressure (q) given by,

$$q = \frac{1}{2}\rho \bar{V}_a^2 \tag{2.26}$$

Here $\bar{V}_a$ is the airspeed, ρ is the air density and T is the magnitude of the thrust vector. The thrust vector, the last term in Equation 2.23, has been coordinated into the wind axes.

2.3.2 Outer Loop Model – Point Mass Kinematics

Having defined the specific forces acting on the aircraft and deriving the corresponding dynamics associated with these forces, the focus of this section is on the motion of the aircraft's wind axes relative to a fixed inertial reference.

With the faster aircraft dynamics separated from the slower aircraft dynamics (through time-scale separation), it is possible to treat the aircraft as a point mass able to rotate and translate in free space (Peddle, 2008). This model, the Outer Loop Model, will thus describe the attitude, velocity and position dynamics of this point mass.

For this model it is assumed that the specific accelerations $(\mathrm{A_W}, \mathrm{B_W}, \mathrm{C_W})$ acting on the aircraft, as well as its roll rate $(\mathrm{P_W})$ are inputs to the system. These inputs are obtained from the Inner Loop model, making the Outer Loop Model completely aircraft independent.

a. Velocity Dynamics

The velocity dynamics, of the aircraft in the wind axes, can be obtained by taking the time derivative of its velocity vector.

$$\frac{d}{dt}\boldsymbol{V}^{WI}\Big|_I = \boldsymbol{A}^{WI} \tag{2.27}$$

The acceleration vector $\boldsymbol{A}^{WI}$ of the above equation can be expanded and written in terms of its two components, the specific acceleration vector ($\boldsymbol{A}^{WI^S}$) and the gravity vector ($\boldsymbol{G}$).

$$\frac{d}{dt}\boldsymbol{V}^{WI}\Big|_I = \boldsymbol{A}^{WI^S} + \boldsymbol{G} \tag{2.28}$$

Since the specific accelerations acting on the aircraft are modeled in the wind axes, it is preferred to have the velocity vector coordinated in the wind axes. By taking the time derivative of the velocity vector with respect to the wind axes, the velocity dynamics take the form of,

$$\tfrac{d}{dt}\boldsymbol{V}^{WI}\Big|_W = -\boldsymbol{\omega}^{WI} \times \boldsymbol{V}^{WI} + \boldsymbol{A}^{WI^S} + \boldsymbol{G}. \tag{2.29}$$

The above equation can now be coordinated into the wind axes. The cross product can be simplified by making use of the skew-symmetric form of $\boldsymbol{\omega}^{WI}$ and the gravity vector can be coordinated from the inertial to wind axes through the direction cosine matrix$\mathbf{DCM}^{\mathrm{WI}}$.

$$\begin{bmatrix}\dot{\bar{V}}\\0\\0\end{bmatrix} = -\begin{bmatrix}0 & -R_W & Q_W\\ R_W & 0 & -P_W\\ -Q_W & P_W & 0\end{bmatrix}\begin{bmatrix}\bar{V}\\0\\0\end{bmatrix} + \begin{bmatrix}A_W\\B_W\\C_W\end{bmatrix} + \mathbf{DCM}^{\mathrm{WI}}\begin{bmatrix}0\\0\\g\end{bmatrix} \tag{2.30}$$

Here $\overline{\mathrm{V}}$ is the magnitude of the aircraft's velocity vector and g is the magnitude of the gravity vector in the inertial space. Equation 2.29 can be split into three equations, the first being the dynamic equation for the velocity magnitude in the wind axes, and the other two being algebraic constraint equations.

$$\dot{\bar{V}} = A_W + ge_{13}^{WI} \tag{2.31}$$

$$\begin{bmatrix}R_W\\Q_W\end{bmatrix} = \frac{1}{\bar{V}}\begin{bmatrix}ge_{23}^{WI}\\ge_{33}^{WI}\end{bmatrix} + \frac{1}{\bar{V}}\begin{bmatrix}B_W\\-C_W\end{bmatrix} \tag{2.32}$$

Here e_{xy}^{WI} corresponds to the element in row x and column y of the $\mathbf{DCM}^{\mathrm{WI}}$ matrix [2].

The constraints of Equation 2.31 can be written in a different form. The process of deriving the alternate form is described in Peddle (2008), and the results are shown below.

$$R_W = \frac{1}{m\bar{V}}Y_W \tag{2.33}$$

$$Q_W = \frac{1}{m\bar{V}}Z_W \tag{2.34}$$

The constraints above are the constraints used in the Inner Loop Model.

b. Position Dynamics

The position dynamics are obtained by taking the time derivative of the position vector with respect to the inertial space.

$$\frac{d}{dt}\boldsymbol{P}^{WI}\Big|_I = \boldsymbol{V}^{WI} \tag{2.35}$$

Because, in this model, the velocity vector is coordinated in the wind axes, the positional dynamics can be rewritten such as to account for this. The velocity vector is thus coordinated into the inertial space, though the DCM matrix.

$$\boldsymbol{P}_I^{WI} = [\mathbf{DCM}^{\mathrm{WI}}]^T\boldsymbol{V}_W^{WI} \tag{2.36}$$

c. Attitude Dynamics

The attitude dynamics relate the rate of change of the Euler angles to the angular velocity components in the wind axes. The relationship can be found by rotating the body axis through a Euler 3-2-1 angle sequence, the resulting equations are thus shown below:

$$\dot{\phi} = P_w + \tan\theta\,(Q_W \sin\phi + R_w \cos\phi) \tag{2.37a}$$

$$\dot{\theta} = Q_W \cos\phi - R_W \sin\phi \tag{2.37b}$$

$$\dot{\psi} = \frac{Q_W \sin\phi + R_W \cos\phi}{\cos\theta} \tag{2.37c}$$

The full derivation of the attitude dynamics (Rotational Kinematic Equations) can be found in Klein and Morelli (2006). It should be noted that the Equations 2.37a to 2.37c are the attitude dynamics as a result of the specific moments.

Similar derivations exist for the Quaternion representation of the attitude dynamics, (Gaum, 2009). The Quaternion attitude dynamics are preferred as these dynamics have no inherent singularities, as with the case of the Euler angles. The Quaternion dynamics are represented below,

$$\begin{bmatrix} \dot{q_0} \\ \dot{q_1} \\ \dot{q_2} \\ \dot{q_3} \end{bmatrix} = \frac{1}{2} \begin{bmatrix} 0 & -P_W & -Q_W & -R_W \\ P_W & 0 & R_W & -Q_W \\ Q_W & -R_W & 0 & P_W \\ R_W & Q_W & -P_W & 0 \end{bmatrix} \begin{bmatrix} q_0 \\ q_1 \\ q_2 \\ q_3 \end{bmatrix} \tag{2.34}$$

2.3.3 Non-Linear Simulation

The two models derived, the Outer Loop Model and the Inner Loop model are combined to form a full non-linear aircraft model. It is this model that is used for simulation throughout this thesis.

This model was implemented in Simulink®, together with an Autopilot model. The Autopilot model consists of control algorithms as well as a Sensor Model and a Servo Model. The Simulink® model is shown in the figure to follow.

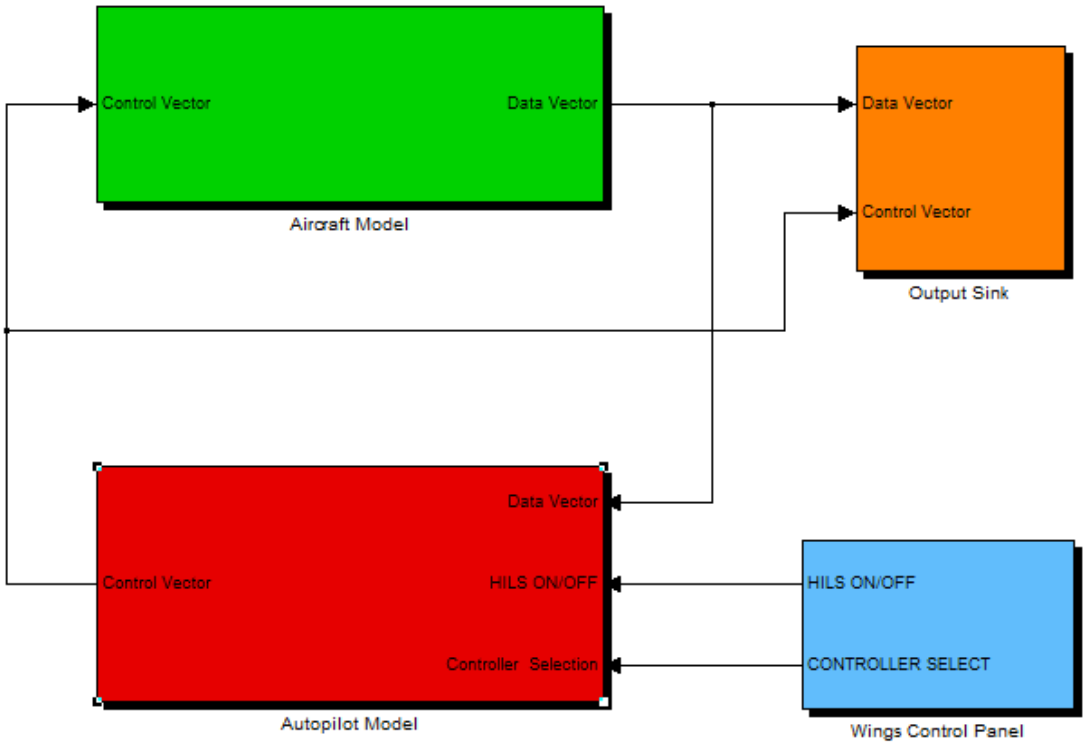

Figure 8: Simulink® Model used for simulation

Chapter 3

System Identification Methods

Several texts cover system identification for both parametric and non-parametric models. In this thesis, only the methods for the estimation of parametric models are covered.

The advantage of using a parametric model is that each parameter has physical meaning. For example in aircraft modeling, C_{L_0} is the static lift coefficient which is characteristic of the amount of lift the aircraft experiences at trim. Non-parametric models on the other hand have no specific or predefined form, and its purpose is to match the resulting output of the model with the measured output of a plant well. Since this thesis forms part of a greater control problem (Fault Tolerant Control) in which the aerodynamic coefficients are required, the parametric model approach was taken.

It must be noted that methods which use the combination of non-parametric and parametric models do exist, such as used in many frequency domain methods of System Identification. These methods are however more computationally expensive and are not ideal for its implementation on the low power processors used for testing in this thesis.

According to Klein (2006) , parameter estimation requires the specification of the following:

1. A model structure with unknown parameters ($\boldsymbol{\theta}$) to be estimated
2. Observations, or measurements, ($\boldsymbol{z}$)
3. A mathematical model for the measurement process
4. Assumptions about the uncertainty in the model parameters ($\boldsymbol{\theta}$) and he measurement noise ($\boldsymbol{v}$)

3.1 Parameter Estimation Models

In chapter 2, the dynamic equations relating the state derivatives to the state and control variables were derived. For the purpose of parameter identification, the relation between the measured outputs and the model parameters are however of more importance. Depending on the model chosen, the measurement equations can be linear or non-linear in the parameters:

$$\boldsymbol{z} = \boldsymbol{H\theta} + \boldsymbol{v} \tag{3.1}$$

Or

$$\boldsymbol{z} = \boldsymbol{h}(\boldsymbol{\theta}) + \boldsymbol{v} \tag{3.2}$$

For the linear case, the output matrix $\boldsymbol{H}$ is assumed to be known and for the non-linear case the function $\boldsymbol{h}(\boldsymbol{\theta})$ has known form.

Based on the uncertainties in the model parameters ($\boldsymbol{\theta}$) and the measurements (quantified by the measurement noise $\boldsymbol{v}$), 3 models were designated by Schweppe (1973). These models include the Bayesian model, the Fisher model and the Least-Squares model.

The characteristics of the three models are shown below [8]:

Bayesian Model

1. $\boldsymbol{\theta}$ is a vector of random variables with probability density $\mathrm{p}(\boldsymbol{\theta})$
2. $\boldsymbol{v}$ is a random vector with probability density $\mathrm{p}(\boldsymbol{v})$

Fisher model

1. $\boldsymbol{\theta}$ is a vector of unknown constant parameters
2. $\boldsymbol{v}$ is a random vector with probability density $\mathrm{p}(\boldsymbol{v})$

Least-squares model:

1. $\boldsymbol{\theta}$ is a vector of unknown constant parameters
2. $\boldsymbol{v}$ is a random vector of measurement noise

Of the above mentioned models the Bayesian model is not commonly used in aircraft parameter estimation. The primary reason behind this is that it is difficult to characterize the probability density of the parameters, $\mathrm{p}(\boldsymbol{\theta})$.The focus of this section is thus on the Fisher and Least-squares models only.

3.1.1 Fisher Model

As previously mentioned, the Fisher model assumes that the measurements are corrupted by additive noise with a known probability density. Fisher (1925) formulated the method called the maximum-likelihood (ML) method to handle such a problem. The ML method is able to handle both process and measurement noise and has the characteristic of being an asymptotically unbiased estimator, i.e.

$$\lim_{N\to\infty} \mathrm{E}\left(\widehat{\boldsymbol{\theta}}_{\mathrm{ML}}\right) = \boldsymbol{\theta} \tag{3.3}$$

Where $\boldsymbol{\theta}$ represents the true parameters of the system, $\widehat{\boldsymbol{\theta}}_{\mathrm{ML}}$ is the ML estimate and N is the sample size. Other characteristics of the ML method that make it a "good" estimator include (Jategaonkar, 1996):

1. The ML estimate $\widehat{\boldsymbol{\theta}}_{\mathrm{ML}}$ converges in probability to the true value of $\boldsymbol{\theta}$.
2. The ML estimates $\widehat{\boldsymbol{\theta}}_{\mathrm{ML}}$ obtained from different sets of data samples are asymptotically normally distributed about the true value of $\boldsymbol{\theta}$.
3. The ML estimates $\boldsymbol{\theta}_{\mathrm{ML}}$ are asymptotically efficient i.e. they attain the Cramér-Rao lower bounds, which indicates the theoretically maximum achievable accuracy of the estimates.

The ML method can be implemented in two ways. The simpler version, in which the process noise is neglected, is called the Output Error method whereas the more complex Filter error method, takes both the process and measurement noise into consideration. Both these methods belong to a general class of output error or response curve fitting methods.

In the output error class, the model parameters are adjusted to minimize the error between the estimated output and the measured output. Methods from this class however lead to a non-linear optimization problem as it consists of a state estimator represented by a Kalman filter and a nonlinear parameter estimator. In the case of the filter error method, the Kalman filter is necessary as in the presence of process noise, the states are random variables. Though the output error method is commonly used, it has been shown to yield poor parameter estimates in the presence of turbulence and measurement inaccuracies. Because of this, the filter error method has found popularity as it handles measurement inaccuracies as well as turbulent effects well.

Maximum Likelihood Estimation

As mentioned previously, the ML method is used to solve the parameter estimation problem when dealing with a fisher model. The ML method is implemented by maximizing the "likelihood function" which can be defined as:

$$\boldsymbol{p(z|\theta)} = \prod_{\boldsymbol{k=1}}^{\boldsymbol{N}} \boldsymbol{p(z_k|\theta)} \tag{3.4}$$

Where $\boldsymbol{p(z|\theta)}$ is the probability of $\boldsymbol{z}$ given $\boldsymbol{\theta}$. The likelihood function represents the probability density of the measurements ($\boldsymbol{z}$) and not of the parameters. The parameters are assumed to be independent of chance.

Because of the exponential nature of many density functions, the logarithm of the likelihood function is preferred. By using the logarithm of the likelihood function (log-likelihood function) the problem is converted into a minimization problem, where:

$$\boldsymbol{\hat{\theta}_{ML}} = \mathbf{arg}\left\{\boldsymbol{\min_{\theta} ln}\, p(\boldsymbol{z|\theta})\right\} \tag{3.5}$$

The process of obtaining the maximum likelihood estimate of both the Filter error and Output error methods are covered in Klein (2006) and Jategaonkar (1996). This estimation process is a two step process:

1. Determine and propagate the states as well as determine the mean and covariance of the innovations $\boldsymbol{v(i)}$, by means of Kalman filtering.
2. Minimize the negative log-likelihood function through optimization algorithms such as the Newton-Raphson or the simplified Gauss-Newton or modified Newton-Raphson methods.

In its simplest form the optimization problem can be reduced to the minimization of the cost function:

$$\mathrm{J}(\boldsymbol{\theta}) = \frac{1}{2}(\mathrm{z} - \mathbf{H}\boldsymbol{\theta})^{\boldsymbol{T}}\boldsymbol{R^{-1}}(z - \boldsymbol{H\theta}) \tag{3.6}$$

Where R is the measurement noise covariance matrix and is assumed to be known.

Practical Issues

The Filter error method as introduced above has many advantages over other methods, such as its superior handling of measurement errors and turbulence effects. The filter error method offers more advantages as it leads to a nearly linear optimization problem, with fewer local minima and has a fast convergence rate. Practically however the filter error method is complex to implement and is computationally expensive.

The flow diagram shown below shows the complexity of implementing the filter error method on a linear system. This flow diagram has been obtained from Jategaonkar (1996).

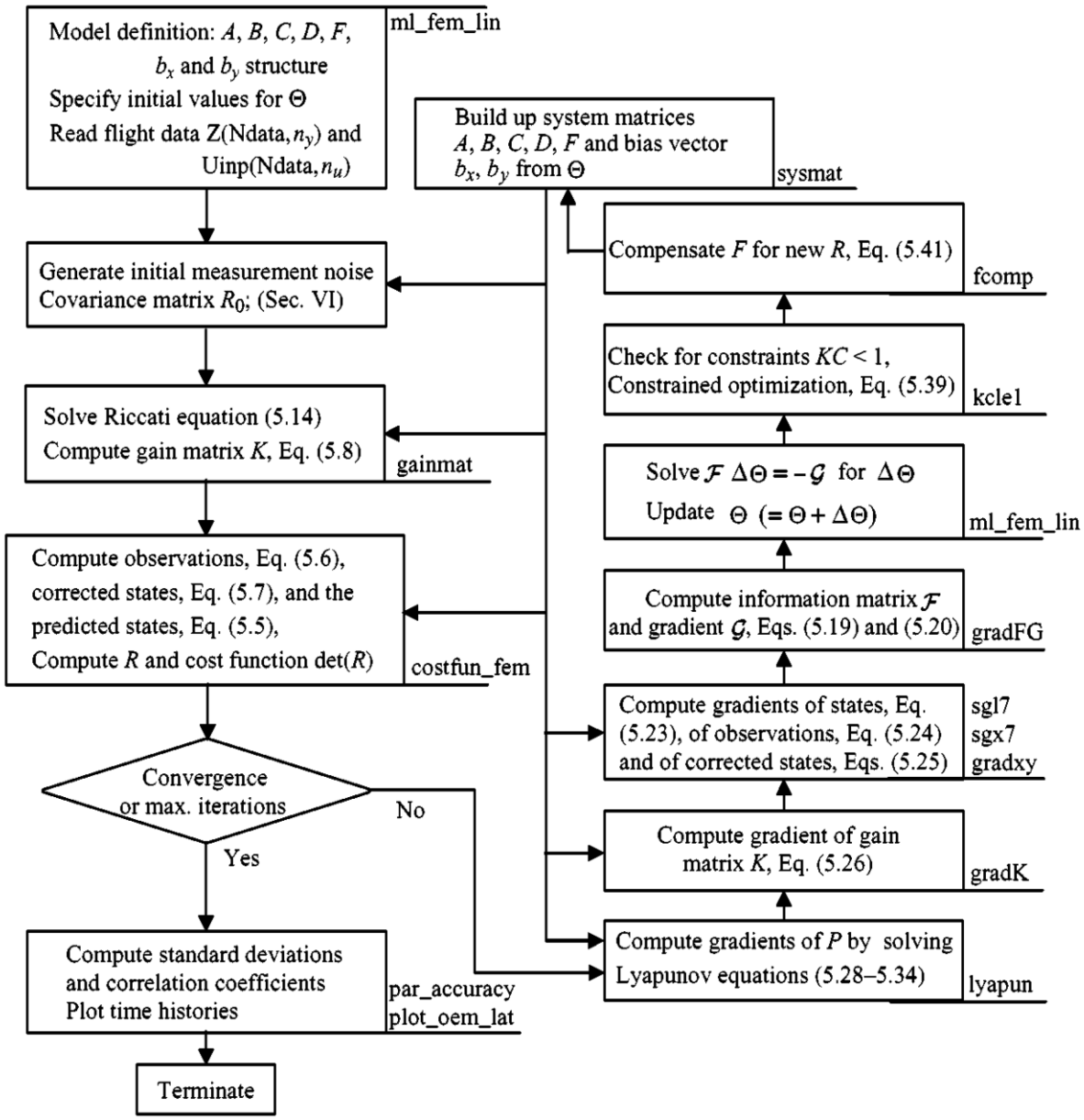

Figure 9: Details of Implemented Filter Error method for linear systems

Though the output error method is a simplified version of the filter error method shown above, it still follows a similar procedure. Due to the complexity of this class of methods the maximum likelihood methods are not suitable for online implementation on the low power processors used on the aircrafts at the ESL. Other downfalls of the method include:

1. Convergence of the optimization algorithm is not assured.
2. The algorithm can converge to a local minimum and not the global minimum.
3. The maximum likelihood method can be sensitive to starting values

3.1.2 Least-Squares Model

The Least-squares model (also known as Regression Methods), where the noise ($\boldsymbol{v}$) is regarded as random vector of measurement noise, is typically solved by means of regression techniques or least-squares methods. These methods form part of a general class of Equation Error methods which have the characteristic of minimizing a cost function, defined directly in terms of an input-output equation. These methods solve the cost function by means of matrix algebra. The input-output equation, as referred to, can be formulated as:

$$z = \theta_1 h_1 + \theta_2 h_2 + \cdots + \theta_n h_n + \varepsilon \tag{3.7}$$

Here $\boldsymbol{z}$ represents the measurements, $\boldsymbol{\theta} = [\theta_1 \theta_2 \ldots \theta_n]$ the unknown parameters, $\boldsymbol{H} = [h_1, h_2, \ldots, h_n]^T$ the independent variables and $\boldsymbol{\varepsilon}$ the model discrepancies and measurement noise. In matrix notation, with several measurement outputs, the input-output equations can be formulated as:

$$\mathbf{z} = \mathbf{H\theta} + \boldsymbol{\varepsilon} \tag{3.8}$$

By minimizing the sum of squares of the errors between the measured output and the output of the model, the „best' parameter estimate ($\boldsymbol{\theta}$) can be obtained. The cost function can thus be represented as:

$$J(\boldsymbol{\theta}) = \frac{1}{2}\sum_{k=1}^{N} \varepsilon^2(k) = \frac{1}{2}\boldsymbol{\varepsilon}^{\mathbf{T}}\boldsymbol{\varepsilon} \tag{3.9}$$

Where N is the amount of samples and k denotes the current sample. $\boldsymbol{\varepsilon}$, which represents the uncertainty in the model can be defined as:

$$\boldsymbol{\varepsilon} = \mathbf{z} - \mathbf{H\theta} \tag{3.10}$$

By substituting Equation 3.10 into Equation 3.9, the general form of the least-squares cost function is obtained:

$$J(\boldsymbol{\theta}) = \frac{1}{2}(\mathbf{z} - \mathbf{H\theta})^{\boldsymbol{T}}(\boldsymbol{z} - \boldsymbol{H\theta}) \tag{3.11}$$

Since the Least-Squares method maps the input-output response solely in terms of the independent (the measured states) and dependent (measured output) variables, the performance and accuracy of the estimated parameters are highly dependent on:

1. The quality of measurements,
2. The assumptions made about the noise,
3. The availability of the necessary states.

Equation 3.11 represents the cost function of the ordinary least squares (OLS) method. The OLS method assumes that the measured states are error and noise free and that the measured outputs are corrupted by uniformly distributed noise. In the case in which the measured outputs have different noise characteristics, the weighted least squares (WLS) method is more commonly used. The WLS cost function is shown below:

$$\mathrm{J}(\boldsymbol{\theta}) = \frac{1}{2}(\mathbf{z} - \mathbf{H}\boldsymbol{\theta})^{\boldsymbol{T}}\boldsymbol{W}(\boldsymbol{z} - \boldsymbol{H}\boldsymbol{\theta}) \tag{3.12}$$

Where $\boldsymbol{W}$ is a weighting matrix reflecting the degree of confidence in the measured outputs. It is common to choose the weighting matrix, such that the weights are inversely proportional to the variance of each of the corresponding measurements, i.e.

$$\mathrm{diag}(\mathbf{W}) = \left[\frac{1}{{\sigma_1}^2} \quad \frac{1}{{\sigma^2}_2} \quad . \quad . \quad . \quad \frac{1}{{\sigma^2}_{\mathrm{n}}}\right] \tag{3.13}$$

Where $\sigma_{()}$ represents the variance of each measurement and n is the number of measurements.

Since the error $\boldsymbol{\varepsilon}$ is a linear function of the parameters $\boldsymbol{\theta}$ (as can be seen from Equation 3.11), the solution to the minimization of the cost function defined above, can be obtained by setting the derivative of $\mathrm{J}(\Theta)$ with respect to Θ to zero, i.e.

$$\frac{\mathrm{J}(\boldsymbol{\theta})}{\boldsymbol{\partial\theta}} = -\mathbf{z}^{\mathbf{T}}\mathbf{H} + \boldsymbol{\theta}^{\boldsymbol{T}}(\boldsymbol{H}^{\boldsymbol{T}}\boldsymbol{H}) = \mathbf{0} \tag{3.4}$$

The solution to the above equation assumes that $(\boldsymbol{X}^{\boldsymbol{T}}\boldsymbol{X})$ is invertible and can be represented as:

$$\widehat{\boldsymbol{\theta}} = (\mathbf{H}^{\mathbf{T}}\mathbf{H})^{-1}\mathbf{H}^{\mathbf{T}}\mathbf{z} \tag{3.1}$$

Where $\widehat{\boldsymbol{\theta}}$ represents the best estimate of the parameters. $\widehat{\boldsymbol{\theta}}$ represents a unique solution to the least-squares model, given that the information matrix ($\mathbf{H}^{\mathbf{T}}\mathbf{H}$) is non-singular. For parameter estimation purposes, specifically aircraft parameter estimation, the information matrix is generally non-singular during specific flight maneuvers. Issues regarding the information matrix such as its inversion as well maintaining its non-singularity are covered in Chapter 5.

Practical Issues

The main limitation of the regression or least-squares methods is its dependence on the dependent variables (the aircraft measured states). In the formulation of the method, it is assumed that the necessary states are exact. Practically, these states are generally obtained through measurement instrumentation and are thus susceptible to both sensor biases and sensor noise.

In order to apply the regression methods to a specific model, it is thus required for the sensor measurements to be pre-processed as to minimize the variance on the measured states. The pre-processing procedures needed to be performed to assure accurate parameter estimates are covered in Chapter 5.

Another limitation is that the information matrix ($\mathbf{H^T H}$) can be singular and not invertible. In this case the parameters estimated will not represent that of the aircraft. Even if invertible, the information matrix still poses a problem for real time applications. Depending on the amount of data sampled, the information can be a large matrix that needs to be inverted. Implementing the Regression method as presented, on the hardware at the ESL, is thus not the most efficient and practical method of System Identification. To overcome the problem of inverting the information matrix, a recursive implementation of the Regression method is presented in Section 4.2. The recursive method alleviates the need to invert the information matrix.

3.1.3 Model Choice

From the above set of arguments it can be seen that for the online estimation of the aircraft parameters, the least-squares model is the preferable choice. The main reasons behind the choice of this model are that the equation error methods used to solve this parametric model are easier to implement and are less computationally expensive than the output error methods of the Fisher model.

The chapters to follow make use of the regression methods to solve the estimation problem. Chapter 4 covers the setting up of the regressors for aircraft parameter identification, while Chapter 5 covers issues relating to the identifiabilty of the parameters for a given aircraft setup.

Chapter 4

Applying Regression Techniques

Regression analysis, as described in the previous chapters, relies on the definition of input-output equations. This section covers the setting up of the regression equations for the identification of the stability and control derivatives used in aircraft modeling and control.

4.1 Input-Output Equations

The classical formulation of the regression equations used for aircraft parameter estimation are based on the aerodynamic force and moment equations. These equations have been presented in Chapter 2 and are repeated below:

***Aerodynamic Force Equations*:**

$$C_D = C_{D_0} + \frac{C_L^2}{\pi A e} \tag{4.1a}$$

$$C_L = C_{L_0} + C_{L_\alpha}\alpha + C_{L_Q}\bar{Q} + C_{L_{\delta_E}}\delta_E \tag{4.1b}$$

$$C_y = C_{y_\beta}\beta + C_{y_P}\bar{P} + C_{y_R}\bar{R} + C_{y_{\delta_A}}\delta_A + C_{y_{\delta_R}}\delta_R \tag{4.1c}$$

Aerodynamic Moment Equations:

$$C_l = C_{l_\beta}\beta + C_{l_P}\bar{P} + C_{l_R}\bar{R} + C_{l_{\delta_A}}\delta_A + C_{l_{\delta_R}}\delta_R \tag{4.2a}$$

$$C_m = C_{m_0} + C_{m_\alpha}\alpha + C_{m_Q}\bar{Q} + C_{m_{\delta_E}}\delta_E \tag{4.2b}$$

$$C_n = C_{n_\beta}\beta + C_{n_P}\bar{P} + C_{n_R}\bar{R} + C_{n_n}\delta_A + C_{n_{\delta_R}}\delta_R \tag{4.2c}$$

Where $\bar{P}, \bar{Q}$ and $\bar{R}$ are the non-dimensional roll, pitch and yaw moments respectively and are defined by:

$$\bar{P} = \frac{b}{2\bar{V}}P \tag{4.3a}$$

$$\bar{Q} = \frac{c}{2\bar{V}} Q \tag{4.3b}$$

$$\bar{R} = \frac{b}{2\bar{V}} R \tag{4.3c}$$

Equations 4.1 and 4.2 are written in the form of the input-output equation of Section 3.1.2. The inputs $(\alpha, \beta, P, Q, R, \delta_E, \delta_R, \delta_A)$ are assumed to be known exactly with the outputs $(C_L, C_y, C_l, C_m, C_n)$ being corrupted by measurement noise. In the case of the pitching moment equation, the regression equation for N samples can be formulated as:

$$\boldsymbol{z} = [C_m(1) \quad C_m(2) \quad \ldots \quad C_m(N)]^T \tag{4.4a}$$

$$\boldsymbol{H} = \begin{bmatrix} 1 & \alpha(1) & \bar{Q}(1) & \delta_E(1) \\ 1 & \alpha(2) & \bar{Q}(2) & \delta_E(1) \\ . & . & . & . \\ . & . & . & . \\ . & . & . & . \\ 1 & \alpha(N) & \bar{Q}(N) & \delta_E(N) \end{bmatrix} \tag{4.4b}$$

$$\boldsymbol{\theta} = \begin{bmatrix} C_{m_0} & C_{m_\alpha} & C_{m_Q} & C_{m_{\delta_E}} \end{bmatrix} \tag{4.4c}$$

where the unknown stability and control derivatives can be calculated as:

$$\hat{\boldsymbol{\theta}} = (\mathbf{H^T H})^{-1} \mathbf{H^T z} \tag{4.5}$$

Before Equations 4.1, 4.2 and 4.3 can be used to find the aircraft parameters, it is necessary to define the aerodynamic force and moment coefficients in terms of measurable quantities. By using the force and moments defined in Chapter 2, the aerodynamic force and moments can be calculated as follows, Jategaonkar (1996):

$$C_x = \frac{1}{qS}(ma_x - T) \tag{4.6a}$$

$$C_y = \frac{m}{qS} a_y \tag{4.4b}$$

$$\mathrm{C_z} = \frac{\mathrm{m}}{\mathrm{qS}} \mathrm{a_z} \tag{4.6c}$$

$$C_L = -C_z \cos\alpha + C_x \sin\alpha \tag{4.6d}$$

$$C_D = -C_x \cos\alpha - C_z \sin\alpha \tag{4.6e}$$

$$C_l = \frac{1}{qSb}[\, I_x\dot{P} + (I_z - I_y)QR] \tag{4.6f}$$

$$C_m = \frac{1}{qSc}[I_y\dot{Q} + (I_x - I_z)PR] \tag{4.6g}$$

$$C_n = \frac{1}{qSb}\left[I_z\dot{R} + (I_y - I_z)PQ\right] \tag{4.6h}$$

Where a_x, a_y and a_z are the accelerometer measurements in the body axis; P, Q and R are the gyroscope measurements in the body axis; I_x, I_y and I_z are the moment of inertia of the aircraft and T is the thrust force.

The aerodynamic force and moment equations represented above, require the rate of change of the gyroscope measurements ($\dot{P}, \dot{Q}, \dot{R}$). Two methods of producing these measurements have been considered: (1) through the differentiation of the gyroscope measurements and (2) by means of distributed sensors. Both these methods are presented in Chapter 7.

By defining each moment equation in terms of its input-output relation, all the unknown stability and control derivatives can be estimated.

4.2 Recursive Implementation

Because of its ease of implementation, the Regression technique was chosen. The problem with the Least-Squares method presented is that all the measurements would have to be taken before estimation takes place.

This is not a big problem, as the algorithm presented can be implemented in such a way that data is collected for a time period, followed by the estimation of the aircraft parameters. This process can then be repeated for the whole duration of flight or when needed.

In the case where the parameters are constantly but slowly changing or it is necessary to update the parameters constantly, a recursive implementation of the algorithm is needed. This section presents the recursive implementation of the Least-Squares method.

4.2.1 Recursive Least Squares (RLS)

Form Section 3.1.2, the least square estimate of the parameters is given as

$$\widehat{\boldsymbol{\theta}} = (\mathbf{H}^{\mathbf{T}}\mathbf{H})^{-1}\mathbf{H}^{\mathbf{T}}\mathbf{z} \tag{4.7}$$

Given a set of k samples of independent variables $\boldsymbol{h} = (h_1, h_2, \ldots h_n)^T$ and dependent variable $\mathbf{y}$, the least squares estimates of $\boldsymbol{\theta}$ are obtained as

$$\widehat{\boldsymbol{\theta}}(\mathbf{k}) = \left(\mathbf{H_k}^{\mathbf{T}}\mathbf{H_k}\right)^{-1}\mathbf{H_k}^{\mathbf{T}}\mathbf{z_k} \tag{4.8}$$

For the sake of simplicity the inverse of the information matrix can be represented by $P(k)$, such that

$$\widehat{\boldsymbol{\theta}}(\mathbf{k}) = \mathbf{P}(\mathrm{k})\mathbf{H_k}^{\mathbf{T}}\mathbf{z_k} \tag{4.9}$$

By following the procedures in Jategoankar (1996), the recursive formulation of the Least Squares method is summarized below,

$$\widehat{\boldsymbol{\theta}}(\mathrm{k}+1) = \widehat{\boldsymbol{\theta}}(k) + \boldsymbol{K}(k+1)\left[\mathbf{y}(\mathrm{k}+1) - \boldsymbol{h}^{\boldsymbol{T}}(k+1)\widehat{\boldsymbol{\theta}}(k)\right] \tag{4.10}$$

$$\mathbf{K}(\mathrm{k}+1) = \frac{\mathbf{P}(\mathrm{k})\mathbf{h}(\mathrm{k}+1)}{1 + \boldsymbol{h}^{\boldsymbol{T}}(k+1)\boldsymbol{P}(k)\boldsymbol{h}(k+1)} \tag{4.11}$$

$$\mathbf{P}(\mathrm{k}+1) = \boldsymbol{P}(k) - \boldsymbol{K}(k+1)\boldsymbol{h}^{\boldsymbol{T}}(k+1)\boldsymbol{P}(k) \tag{4.12}$$

From the previous equations, it must be noted that the term $\boldsymbol{h^T}(k+1)\boldsymbol{P}(k)\boldsymbol{h}(k+1)$ is a scalar term. Thus we note that the matrix inversion required in the algorithm presented in Section 3.1.2, has been replaced through scalar division at each step in the recursive version.

To start the algorithm, initial values need to be specified for the parameters $\widehat{\boldsymbol{\theta}}$ and the matrix **P** (which refers to the covariance matrix of the estimated states). In the absence of prior knowledge, zero initial values for the parameters can be chosen. The initial **P** can be assumed to be a diagonal matrix with large values (normally chosen to be in the order of 10^6).

4.2.2 Exponential Forgetting Method

The RLS algorithm presented in Equations 4.7.1 to 4.12, is the simplest of the recursive procedures. However, in practice the convergence of RLS to changing parameters is generally poor. In the classical RLS the covariance vanishes to zero with time, losing its capability to keep track of changes in the parameter. In order to improve the convergence of RLS and to allow the RLS to adapt rapidly with time, the past information must be quickly discarded. This can be achieved through the use of a forgetting factor, λ, which introduces exponentially decaying weights on the past measurement, Wihan (2008). The cost function with the forgetting factor included, is formulated as,

$$\mathrm{J}(\boldsymbol{\theta}) = \frac{1}{2}\sum_{\mathrm{k}=1}^{\mathrm{N}} \lambda^{k-1}\varepsilon^2(\mathrm{k}), \qquad 0 < \lambda \leq 1 \tag{4.13}$$

The estimation algorithm that minimizes the cost function in Equation 3.1 can be developed in a similar manner to that of RLS algorithm in Equations 4.7 to 4.12. The resulting equations given by [2] as

$$\widehat{\boldsymbol{\theta}}(\mathrm{k}+1) = \widehat{\boldsymbol{\theta}}(k) + \boldsymbol{K}(k+1)\left[\mathbf{y}(\mathrm{k}+1) - \boldsymbol{h^T}(k+1)\widehat{\boldsymbol{\theta}}(k)\right] \tag{4.14}$$

$$\mathbf{K}(\mathrm{k}+1) = \frac{\mathbf{P}(\mathrm{k})\mathbf{h}(\mathrm{k}+1)}{\lambda + \boldsymbol{h^T}(k+1)\boldsymbol{P}(k)\boldsymbol{h}(k+1)} \tag{4.15}$$

$$\mathbf{P}(\mathrm{k}+1) = \frac{1}{\lambda}\{\boldsymbol{P}(k) - \boldsymbol{K}(k+1)\boldsymbol{h^T}(k+1)\boldsymbol{P}(k)\} \tag{4.16}$$

For $\lambda = 1$, the above equation reduces to the RLS equations. It is observed that smaller values of λ tend to neglect more and more data points in the farther past.

4.2.3 Covariance Resetting

Though the exponential forgetting method allows for a system with changing parameters, it suffers from a problem known as covariance wind-up or blow-up. This occurs during periods when the excitation of the system is poor. During poor excitations old data is continuously being neglected while little new dynamic information is available to the estimator. This could lead to the exponential growth of the covariance matrix and as a result the estimator becomes extremely sensitive and therefore susceptible to numerical and computational errors [22].

Methods used to address the problem of covariance wind-up, include limiting the growth of the covariance matrix by introducing an upper-bond. Another method, the one presented in this section, is to reset the covariance matrix during low excitation periods. Covariance resetting is achieved by setting the matrix **P** to a diagonal matrix with large values (normally chosen to be in the order of 10^6).

4.3 Pre-processing Flight Data

As regression methods assume that the input states are known without error, any noise or biases on the accelerometer or gyroscope measurements result in errors on the estimated parameters.

The pre-processing procedure of flight data is two-fold:

1. Checking the data consistency
2. Characterizing the noise and biases of the sensors

4.3.1 Measurement Errors

As measurement errors affect the quality of the estimated parameters, it is necessary to account for these errors. Measurement errors can be put into two broad categories: deterministic (systematic) and non-deterministic (random) errors.

a. Deterministic Errors

Deterministic errors commonly arise due to biases, scale factors and drift. These errors can arise from either the misalignment of the measurement instrumentation with respect to the body axis (position errors) or from steady-state or growing offsets in the measurements.

Position errors normally occur when the measuring instrumentation are not placed on the center of gravity (c.g) of the aircraft, or they are misaligned with respect to the principle axes of the aircraft. One effect of position errors is the cross-coupling of the measurements. To illustrate this, consider accelerometers placed an offset (x_{off}, y_{off}, z_{off}) from the c.g. The resulting measurement as read by the accelerometers will include the effects of acceleration of the aircraft as well as the rotation dynamics of the aircraft. This can be seen in the resulting equations, Cook (1997):

$$a_x^{'} = \dot{U} - RV + QW - x_{off}(Q^2 + R^2) + y_{off}(PQ - \dot{R}) + z_{off}(PR + \dot{Q}) \quad (4.17)$$

$$a_y^{'} = \dot{V} - PW + RU + x_{off}(PQ + \dot{R}) - y_{off}(P^2 - R^2) + z_{off}(PR + \dot{P}) \quad (4.18)$$

$$a_y^{'} = \dot{W} - QU + PV + x_{off}(PR + \dot{Q}) - y_{off}(QR + \dot{P}) + z_{off}(P^2 + Q^2) \quad (4.19)$$

Biases, scale factors and drift are normally associated with the measuring instrumentation themselves. Scale factor errors generally arise when converting the measurements from a voltage or current measurement to the corresponding acceleration, position or velocity value. Biases and drift are offsets or growing offsets in the measurements caused by temperature variations or error build-ups in the sensor. These can either be a constant effect or as in the case of gyroscope biases, the biases can vary slowly over time (random walk biases).

Another source of deterministic errors, time-shifts, can arise from the asynchronous sampling of data or from the non-uniform filtering of the measurements. The effects of deterministic errors on a measured signal are illustrated in Figure 10.

b. Non-Deterministic Errors

Non-deterministic errors are random in nature. The three most common non-deterministic errors include drop out, disturbance errors and quantization errors. Drop out is caused by an unpredictable loss of measured data, which could be caused by a temporary failure in the instrumentation or the failure to log all the data of a maneuver. Disturbance errors on the other hand are caused by mechanical, electrical or atmospheric interferences on the measurement instrumentation. The last source, quantization errors, is as a result of the finite resolution that sensors have. These three non-deterministic errors are illustrated in the Figure 11.

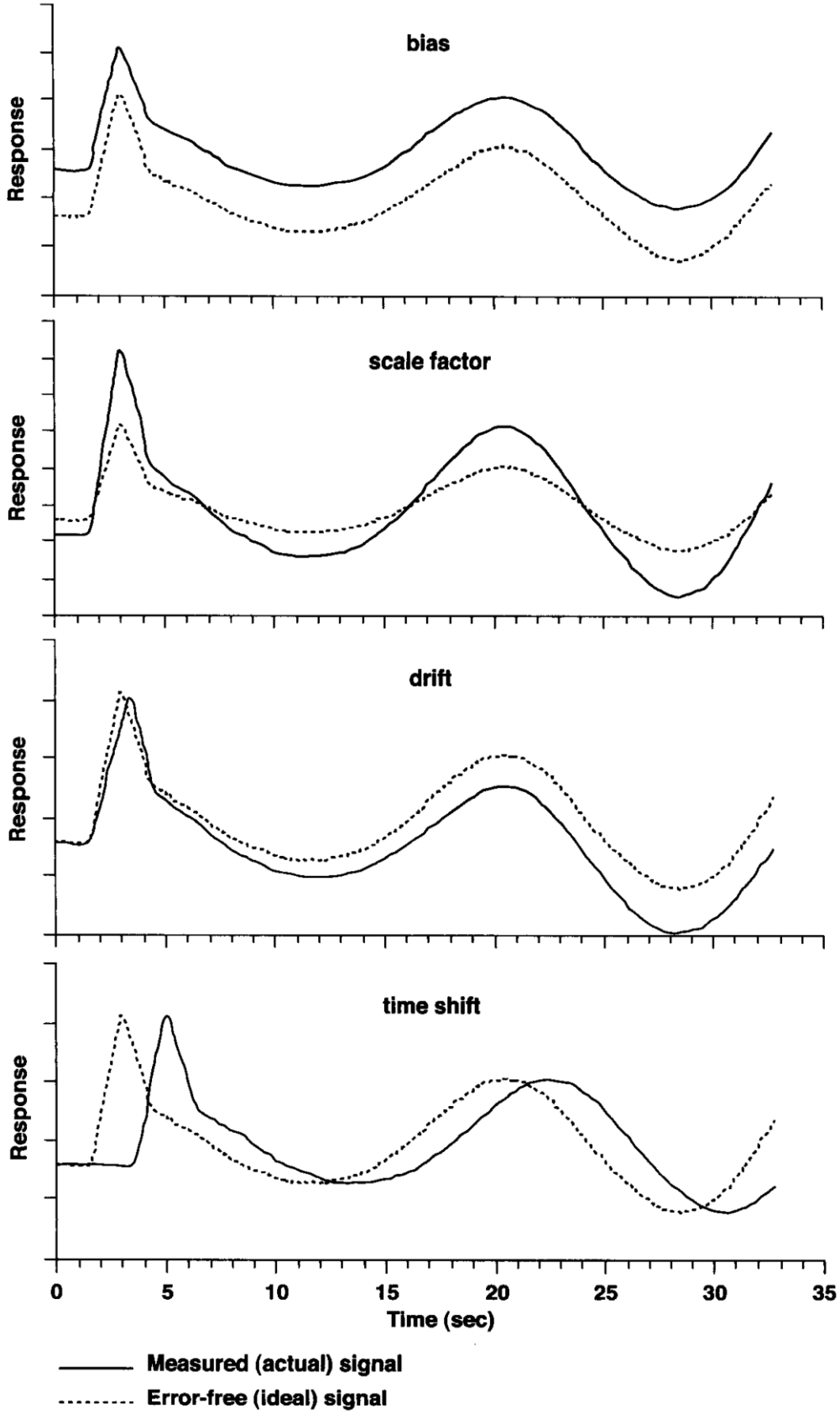

Figure 10: Deterministic Measurement Errors (Tischler, 2006)

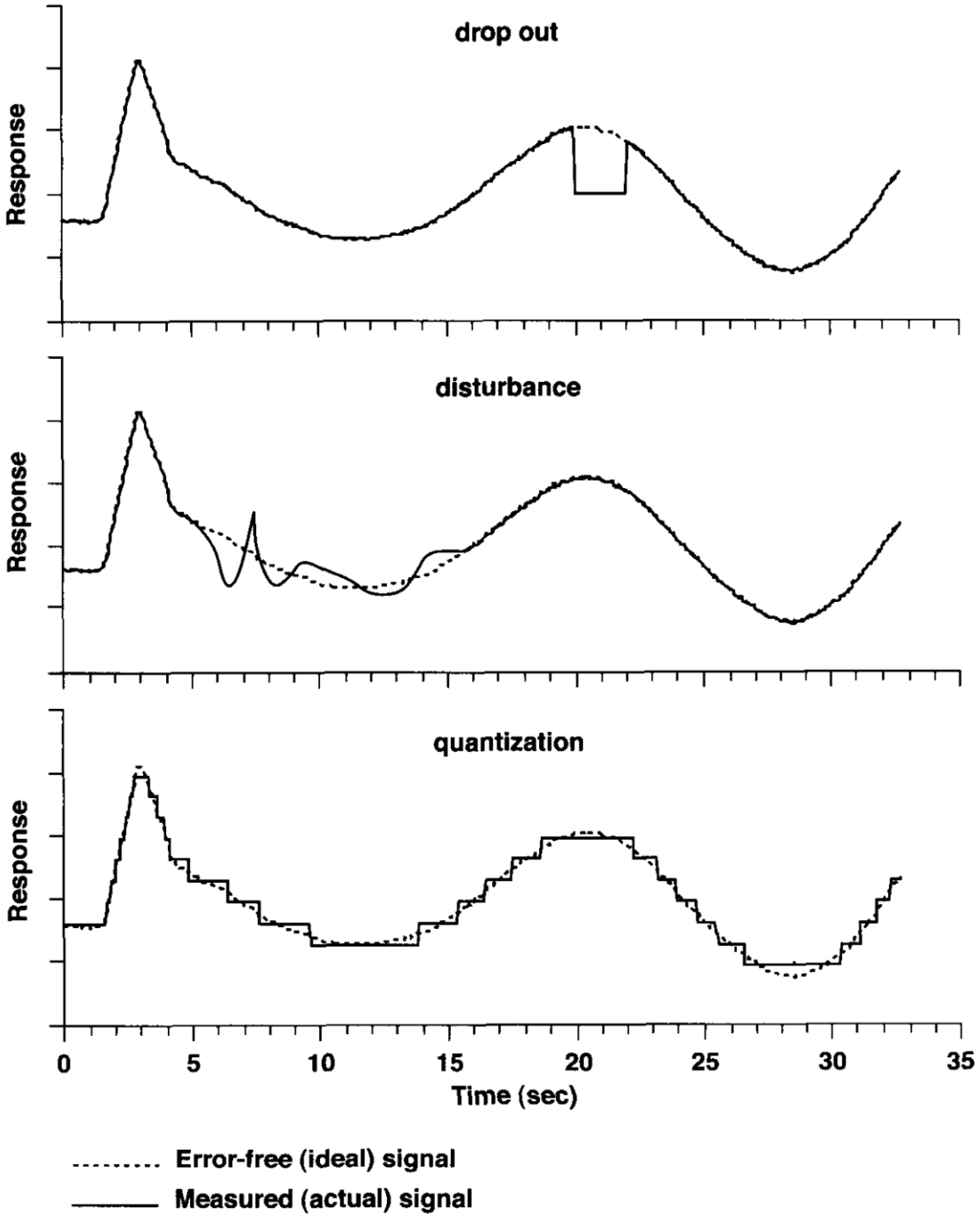

Figure 11: Non-deterministic Measurement Errors (Tischler, 2006)

4.3.2 Data Consistency Check

As measurement data are susceptible to being corrupted, a means to check the validity of the data is needed. By checking the kinematic consistency of the measurement data, it is not only possible to detect whether systematic errors do exist within in the measurement data, but it is also possible to isolate and quantify these errors.

From a System Identification standpoint, it is necessary for the measurement data to be kinematicaly consistent, as this is needed to ensure a consistent mathematical model. The kinematic model that is to be used for the data compatibility check is derived in this section.

a. The Kinematic model for data compatibility checks

The dynamic equations that make up the kinematic model used for data compatibility checks are coordinated in the body axes for the main reason that the angular rate measurements, linear acceleration measurements and velocity measurements are taken in the body axes.

The first set of equations is derived from the translational equations of motion. From Newton's Second law,

$$\sum \boldsymbol{F_B} = \frac{d}{dt}(m\boldsymbol{V})\Big|_B \tag{4.20}$$

Here $\sum \boldsymbol{F_B}$ is the sum of all the forces acting on the aircraft, referenced to the body axes. Since the body frame is not an inertial frame, Equation 4.20 becomes,

$$\sum \boldsymbol{F_B} = m\dot{\boldsymbol{V}} + \boldsymbol{\omega^{BI}} \times m\boldsymbol{V} \tag{4.21}$$

Expanding Equation 2.3 and separating the specific forces and gravitation forces from $\sum \boldsymbol{F_B}$, the translational equations of motion in the body axes can be written as,

$$X_B{}^{\Sigma} - = m\left(\dot{U} + QW - RV\right) - \ mg\sin\theta \tag{4.22a}$$

$$Y_B{}^{\Sigma} = m\left(\dot{V} + RU - PW\right) + \ mg\cos\theta\sin\phi \tag{4.22b}$$

$$Z_B{}^{\Sigma} = m\left(\dot{W} + PV - QU\right) + \ mg\cos\theta\cos\phi \tag{4.22c}$$

Here $X_B{}^{\Sigma}$, $Y_B{}^{\Sigma}$ and $Z_B{}^{\Sigma}$ are the external specific forces acting on the aircraft, P,Q and R the measured angular rates in the body axes and U,V and W, the velocity components coordinated in the body axes and the angles θ and ϕ denote the roll and pitch angles respectively.

The previous equation can be further simplified by noting that the specific forces $\left({X_B}^{\Sigma},\ {Y_B}^{\Sigma},\ {Z_B}^{\Sigma}\right)$ can be written in terms of the accelerations $\left(a_x, a_y, a_z\right)$ along the three body axes.

$$\begin{bmatrix} {X_B}^{\Sigma} \\ {Y_B}^{\Sigma} \\ {Z_B}^{\Sigma} \end{bmatrix} = m \begin{bmatrix} a_x \\ a_y \\ a_z \end{bmatrix} \tag{4.23}$$

Substituting Equation 4.22 into Equation 4.23 and rewriting the equations into a state variable form yields,

$$\dot{U} = -QW + RV - g\sin\theta + a_x \tag{4.24a}$$

$$\dot{V} = RU - PW + g\cos\theta\sin\phi + a_y \tag{4.24b}$$

$$\dot{W} = PV - QU + mg\cos\theta\cos\phi + a_z \tag{4.24c}$$

In addition to the above kinematic equations, there are kinematic equations relating the attitude of the aircraft (ϕ, θ and ψ) to the angular rates P, Q and R. These kinematic equations have been derived in Section 2.3.2 and shown below:

$$\dot{\phi} = P + \tan\theta\,(Q\sin\phi + R\cos\phi) \tag{4.25a}$$

$$\dot{\theta} = Q\cos\phi - R\sin\phi \tag{4.25b}$$

$$\dot{\psi} = Q\sin\phi\sec\theta + R\cos\phi\sec\theta \tag{4.25c}$$

The last set of kinematic equations is obtained from the position dynamics. The kinematic relations for the position are given by

$$\begin{aligned} \dot{X_E} = {} & U\cos\psi\cos\theta + V(\cos\psi\sin\theta\sin\phi - \sin\psi\cos\phi) \\ & + W(\cos\psi\sin\theta\sin\phi - \sin\psi\sin\phi) \end{aligned} \tag{4.26a}$$

$$\begin{aligned} \dot{Y_E} = {} & U\sin\psi\cos\theta + V(\sin\psi\sin\theta\sin\phi - \cos\psi\cos\phi) \\ & + W(\sin\psi\sin\theta\sin\phi - \cos\psi\sin\phi) \end{aligned} \tag{4.26b}$$

$$\dot{Z_E} = U\sin\theta - V\cos\theta\sin\phi - W\cos\theta\cos\phi \tag{4.26c}$$

Equations 4.24 to 4.26 represent the complete set of kinematic relationships that will be used for data compatibility checks.

b. Flight Path Reconstruction

Flight Path Reconstruction (FPR) is the method used to check the kinematic consistency of the measured aircraft data, [12]. The equations presented in the previous section are exact in terms of motion variables (U, V, W), (ϕ, θ, φ), (X_E, Y_E, Z_E), (P, Q, R) and (a_x, a_y, a_z).

The FPR model is formulated by treating the first three triples as state variables with the state equations represented by Equations 4.24 to 4.26. The measurements of the last two triples are assumed to be available, and thus known. This is a valid assumption as these measurements are obtained from the gyroscopes and accelerometers on the aircraft. Given the states, the state equations and the measurements, all the required information for state estimation is available.

Once the states of the aircraft's motion are knowN, it is possible to derive other measured variables such as angle of attack α, angle of sideslip β, true airspeed $\bar{V}$, and dynamic pressure $\bar{q}$.

$$\bar{V} = \sqrt{U^2 + V^2 + W^2} \tag{4.27}$$

$$\alpha = \tan^{-1}\left(\frac{W}{U}\right) \tag{4.28}$$

$$\beta = \sin^{-1}\left(\frac{V}{\bar{V}}\right) \tag{4.29}$$

$$\bar{q} = \frac{1}{2}\rho\bar{V}^2 \tag{4.30}$$

The FPR estimator is thus summarized as below:

1. The state and input vectors are given by:

$$\mathbf{x} = [U \quad V \quad W \quad \phi \quad \theta \quad \varphi \quad X_E \quad Y_E \quad Z_E]^T \tag{4.31}$$

$$\mathbf{u} = [a_x \quad a_y \quad a_z \quad P \quad Q \quad R]^T \tag{4.32}$$

2. The state equation is represented by Equations 4.24 to 4.26, where

$$\dot{\mathbf{x}} = f(\mathbf{x}, \mathbf{u}) \tag{4.33}$$

3. The output equation **y** is calculated from Equations 4.27 to 4.30

$$\mathbf{y} = [\bar{V} \quad \alpha \quad \beta \quad \phi \quad \theta \quad \varphi \quad Z_E] \tag{4.34}$$

As the kinematic relationships presented here are exact, any discrepancies between the variables (α, β, $\bar{V}$,$\bar{q}$) estimated by means of FPR and their actual measured values, are as a result of measurement errors (as discussed in Section 4.2.1). These errors need to be accounted for before the measurements can be used in the System Identification algorithms.

4.3.3 Sensor bias determination

As mentioned in Section 4.3.1, measurement devices are susceptible to many sources of errors. As the system identification algorithms are highly dependent on the quality of the measurements used for the regressors, it is necessary to account for these errors. Because the non-deterministic errors are random in nature, it is not possible to account for these beforehand. The deterministic errors as described in Section 4.3.1 can however be accounted for and is thus the discussion of this section.

Though this section provides a method to account for scale factors, biases and drift by using flight data, it is always best to calibrate the sensors as best as possible prior to flight. Accelerometers and gyroscopes can be calibrated on vibration tables and rate tables, prior to flight. In this way, the biases and scale factors can be more accurately determined. It is sometimes not possible to fully calibrate some sensors prior to flight. Sensors such as AoA sensors and AoS sensors are highly dependent on their position on the aircraft, and thus wind-tunnel tests are not always sufficient to calibrate these types of sensors.

By paying particular attention to the placement and alignment of sensors, the effects of dynamic cross-coupling can be minimized or quantified. In this way, the placement of the sensors does not have to be estimated from flight data.

a. Bias and Scale Factor estimation

In the estimation of the biases of the measured quantities some assumptions have to be made. The main assumption being that though the biases on measured quantities are not always constant, they can be assumed to be constant over the period of the aircraft maneuvers performed for system identification.

One method of estimating the biases and scale factors of the measured quantities is to augment the states of the FPR model presented in the previous section, with the biases to be estimated. By making use of an extended Kalman filter (EKF), the biases and scale factors can then be estimated. It has been found, however, that though the EKF implementation is more rigorous, the method is quite involved and requires prior knowledge of the noise covariance matrices and noise statistics. Without good knowledge of the noise statistics, the EKF has been shown to perform poorly and in some cases cause convergence problems. The process of applying the EKF algorithm to estimate the measurement biases and scale factors is presented in Jonkers (1976).

A simpler method of determining these biases and scale factors is to augment the states of the FPR model with the biases and scale factors, and then using the Output-Error method (maximum likelihood methods) to estimate the biases and scale factors. This method has been obtained from Jategoankar (1996), and is summarized below:

b. Bias and Scale factor determination: The Output error method

To implement the Output-Error method to determine the bias and scale factors, as done in Jategoankar (2006) and Goes, Hemerly and Maciel (2004), the following needs to be defined:

1. The state equations,
2. The observation equations
3. Input variables
4. The parameters to be estimated
5. The method used for integration
6. An optimization method and convergence criteria

The method of implementing the output equation is described in Jategaonkar (1996), while the equations and methods used are stated below:

State Equations:

In setting up the state equations, the following assumptions were made:

1. The airspeed and altitude measurements ($\bar{V}$ and Z_E) are well known, and do not have any bias or scale factor errors.
2. The accelerometer ($a_x \quad a_y \quad a_z$) and gyroscope ($P \quad Q \quad R$) measurements are scaled correctly and thus only have bias errors
3. The AoA (α) and AoS (β) are corrupted by both scale factor and bias errors. As mentioned earlier this is because the wind-tunnel calibration of these quantities is not always reliable.

Including the above mentioned biases and scale factors into the kinematic model presented in the previous section (Section 4.3.2), the following kinematic state equations are determined as [24]:

Velocity Dynamics:

$$\dot{U} = -(Q - \Delta q\ )W + (R - \Delta r)V - g\sin\theta + \ a_x - \ \Delta a_x \tag{4.35a}$$

$$\dot{V} = (R - \ \Delta r)U - (P - \Delta p)W + \ g\cos\theta\sin\phi + \ a_y - \Delta a_y \tag{4.35b}$$

$$\dot{W} = (P - \Delta p)V - (Q - \Delta q)U + \ mg\cos\theta\cos\phi + \ a_z - \ \Delta a_z \tag{4.35c}$$

Attitude Dynamics:

$$\dot{\phi} = (P - \Delta p) + \ (Q - \Delta q)\sin\phi\tan\theta + (R - \ \Delta r)\cos\phi\tan\theta \tag{4.36a}$$

$$\dot{\theta} = \ (Q - \Delta q)\cos\phi - \ (R - \ \Delta r)\sin\phi \tag{4.36b}$$

$$\dot{\psi} = (Q - \Delta q)\sin\phi\sec\theta + \ (R - \ \Delta r)\cos\phi\sec\theta \tag{4.36c}$$

Altitude Dynamics

$$\dot{Z_E} = U\sin\theta - \ V\cos\theta\sin\phi - \ W\cos\theta\cos\phi \tag{4.37a}$$

Here the gyroscope biases are represented by Δp, Δq, and Δr; and the accelerometer biases represented by Δa_x, Δa_y, Δa_z. The state vector can thus be determined from the above equations as:

$$\boldsymbol{X} = \begin{bmatrix} U & V & W & \phi & \theta & \phi & Z_E \end{bmatrix}^T \tag{4.38}$$

Observation Equations

The observation vector is given as:

$$\mathbf{y} = [\bar{V} \quad \alpha \quad \beta \quad \phi \quad \theta \quad \varphi \quad Z_E]^T \tag{4.39}$$

Where the AoA and AoS can be determined from:

$$\alpha = K_\alpha \tan^{-1}\left(\frac{W}{U}\right) + \Delta\alpha \tag{4.40}$$

$$\beta = K_\beta \sin^{-1}\left(\frac{V}{\bar{V}}\right) + \Delta\beta \tag{4.41}$$

Here the bias and scale factors of the AoA and AoS measurements are given by K_α and $\Delta\alpha$ for the AoA; and K_β and $\Delta\beta$ for the AoS. The velocity $\bar{V}$, the attitude and the altitude variables can be determined as determined in the FPR method.

FPR Input Variables

The input variables used are the gyroscope and accelerometer measurements. The input vector is thus given as:

$$\mathbf{u} = [a_x \quad a_y \quad a_z \quad P \quad Q \quad R]^T \tag{4.42}$$

Parameters to be estimated

The parameters that are to be estimated include the gyroscope and accelerometer biases, as well as the AoA and AoS scale factors and biases. The parameter vector is thus given as:

$$\boldsymbol{\Theta} = [\Delta a_x \quad \Delta a_y \quad \Delta a_z \quad \Delta p \quad \Delta \mathrm{q} \quad \Delta r \quad K_\alpha \quad \Delta\alpha \quad K_\beta \quad \Delta\beta]^T \tag{4.43}$$

Method of Integration

The method of integration chosen to integrate the sates was the 4th order Runge-Kutta method. This method was chosen as it is more accurate than using the Euler integration method and produces adequate results [24].

Optimization method

Jategoankar (2006), introduces several optimization methods that can be used to solve the Output-Error method. A matlab program „ml_oem.m' was obtained from Jategoankar (2006) and edited for the purposes of estimating the parameters as stated before. In this program two methods of optimization are available:

1. The Gauss-Newton method
2. Levenberg-Marquardt method

In this thesis, the Gauss-Newton method was used. For more details on the method and its implementation, refer to [12].

Implementation of the Output Error method

The implementation of the Output-Error method is described in more detail in [12, 23]. The results of using the Output-Error method for bias and scale factor determination can be found in Chapter 8, where it is applied to simulation data obtained from a non-linear simulation of the Modular UAV aircraft.

Chapter 5

Parameter Identifiability

In the previous chapters, different SID methods were introduced. It was made evident that the more accurate the sensor measurements, the better the estimate of the aircraft parameters produced by these methods. Though having accurate methods of performing SID, as well as having accurate measurements are key in estimating the aircraft parameters, it does not ensure that the estimated parameters converge to their true values.

This chapter covers different aspects that need to be considered in order to ensure that the parameters converge to their true values. The chapter also presents methods to quantify how well the estimated parameters represent the true parameters.

5.1 Modeling Errors

In the determination of the model used for SID, many assumptions have been made. The model presented in this thesis, makes use of the first order terms of the Taylor expansion of the aerodynamic coefficients. Including higher order terms such as the effects of $\dot{\alpha}$ and $\dot{\beta}$ on the aerodynamic coefficients have been used in some sources, as their effects can be prominent. For the purpose of this thesis, however, these terms have been ignored for two reasons. The first reason being the availability of these measurements themselves, and the second being the fact that the model on which the control system for the aircraft is built does not include these effects.

Another assumption made, was that the airframe of the aircraft in question was modeled as a rigid body. For the application of SID to model aircrafts, this assumption is assured through the construction of the aircraft itself. In bigger aircrafts however, wing effects are more prominent. Flexible wings, introduce flexible structural modes which in turn introduce significant effects on the measured response of the aircraft.

In determining the complexity of the model to be used for SID, one must select a model that is complex enough to be realistic, but at the same time not over paramatized so as to cause

identifiability problems. For parameters to be accurately estimated, each parameter must be able to produce a significant and unique change in the measured response.

It is clear that errors are inherent in the modeling processes. The process of determining the correct model is an iterative approach and can prove to be a lengthy process. In order for the error to be accounted for, it must be first modeled and thus this process can result in circular reasoning. For purposes of this thesis the model chosen has been adapted from [12,13,18].

5.2 Estimate Statistics

When applying the Regression techniques to solve the Parameter estimation problem, it is necessary to determine how well the estimates represent the true parameters. In most cases, the true parameters are not known and so a direct comparison is not possible. There do, however, exist a few criteria by which the estimated regression can be assessed in terms of accuracy and efficiency. These include [25]:

1. Residual Sum of Squares
2. Squared Multiple correlation coefficient
3. Prediction sum of squares
4. Autocorrelation coefficient
5. F-Statistic
6. Partial-F statistic
7. Residual mean and variance
8. Normal quantile-quantile plot

These criteria thus form part of a pre-check when performing a regression analysis. Though not all covered in this thesis, Stuckey (1991), gives more details to what these criteria involves. In this chapter, however, Two main problems associated with regression analysis are discussed; this includes the problems of scaling and collinearity. Both these problems can result in numerical problems which in turn lead to inaccurate estimates of the aircraft parameters and their variance.

5.2.1 Scaling

Improperly scaled regressors and response variables can cause a loss in computational accuracy and as result, errors in the parameters being estimated. One method of scaling the regressors and response variable is through *unit length scaling***.** This entails adjusting the variables such that their sample variances equal 1.

In regression analysis it is common to use standardized variables, this means that the variables are not only scaled using unit length scaling, but are also centered. Centering involves the subtraction of its mean.

The standardized regressor matrix H^*, has components given by

$$h_j^* = \frac{\boldsymbol{h}_j}{s(h_j)} \tag{5.1}$$

Where the variance is calculated as,

$$s^2(x_j) = \frac{(\boldsymbol{H}^T\boldsymbol{H})_{jj}}{p} \tag{5.2}$$

Here p is the number of parameters in the model. It is now possible to obtain estimates from the standardized regression model,

$$z = \boldsymbol{H}^*\boldsymbol{\theta}^* + \boldsymbol{\varepsilon} \tag{5.3}$$

The least-squares solution can then be determined as before:

$$\widehat{\boldsymbol{\theta}}^* = (\boldsymbol{H}^{*\,\boldsymbol{T}}\boldsymbol{H}^*)^{-\mathbf{1}}\boldsymbol{H}^{*\,\boldsymbol{T}}\boldsymbol{z} \tag{5.4}$$

These standardized parameters can be related to the actual parameters by

$$\theta_j = \frac{\widehat{\theta}_j^{\,*}}{s(h_j)} \tag{5.5}$$

From the above discussion, the standardized Information Matrix $\boldsymbol{H}^{*\,\boldsymbol{T}}\boldsymbol{H}^*$ takes the form of the correlation matrix

$$\boldsymbol{H^{*T}H^{*}} = \begin{bmatrix} 1 & r_{12} & \dots & r_{1k} \\ r_{21} & 1 & \dots & r_{2k} \\ \dots & \dots & \dots & \dots \\ r_{j1} & r_{j2} & \dots & 1 \end{bmatrix} \tag{5.6}$$

where

$$r_{jk} = \frac{\boldsymbol{h_j}^T \boldsymbol{h_k}}{\sqrt{(\boldsymbol{H^T H})_{jj}\,(\boldsymbol{H^T H})_{kk}}} \tag{5.7}$$

Here r_{jk} represents the pair-wise correlation between parameters and is used to determine collinearity in the data (as discussed in the next section).

5.2.2 Data Collinearity

Collinearity concerns the relationship between the regressors. As mentioned earlier (Chapter 3), it was shown that in order for a unique set of parameters to be estimated, the information matrix ($\mathbf{H^T H}$) must be non-singular and invertible. This is only achievable if the independent variables, or regressors, are linearly independent, i.e. there does not exist a set of non-zero constants k_j whereby

$$\sum_{j=1}^{\boldsymbol{p}} k_j \boldsymbol{h_j} = 0 \tag{5.8}$$

Here p is the number of parameters to be estimated.

Practically, the problem of collinearity often exists. This is because the assumption that the regressors are linearly independent is only approximately true. In the presence of collinearity, the information matrix ($\mathbf{H^T H}$) is ill-conditioned which can cause computational problems and in turn reduce the accuracy of the estimates.

Common sources of collinearity include:

1. The design of the experiment;
2. constraints in the data, and
3. the model used

An incorrectly designed experiment, can result in one or more of the variables, corresponding to the parameters being estimated, not being sufficiently excited and in turn result in collinearity. This can be as a result of a control input that is not properly designed, and thus does not excite the dynamics of a specific aircraft mode sufficiently. The design of control inputs that sufficiently stimulates the specific aircraft modes for System Identification is covered in Section 5.3.

Constraints in the data arise when various control inputs are actuated together. An aircraft having aileron-to-rudder interconnection, where an automatic rudder deflection follows an aileron input will fall in this category. In such a configuration, the controls will have a near linear dependence and thus cause collinearity. Likewise, an over-paramatised model can also cause collinearity. In this case, the information content in the data available is not sufficient to estimate all the parameters of the model in question.

To detect collinearity, the information matrix can be used. The information matrix is best used in its standardized form (as discussed in the previous subsection), such as to alleviate the problems associated with scaling.

It can be shown that the Variance-Covariance Matrix of the estimated parameters can be expressed as [25],

$$cov(\widehat{\boldsymbol{\theta}}) = \begin{bmatrix} var(\hat{\theta}_1) & cov(\hat{\theta}_1, \hat{\theta}_2) & \dots & cov(\hat{\theta}_1, \hat{\theta}_k) \\ cov(\hat{\theta}_2, \hat{\theta}_1) & var(\hat{\theta}_2) & \dots & cov(\hat{\theta}_2, \hat{\theta}_k) \\ \dots & \dots & \dots & \dots \\ cov(\hat{\theta}_k, \hat{\theta}_1) & cov(\hat{\theta}_k, \hat{\theta}_2) & \dots & var(\widehat{\theta_k}) \end{bmatrix} \tag{5.9}$$

Here the diagonal of this matrix represents the variance of the estimated parameters. This matrix can be written in terms of the information matrix and the variance as [26],

$$cov(\widehat{\boldsymbol{\theta}}) = \sigma^2 (\boldsymbol{H^T H})^{-1} \tag{5.10}$$

Where σ^2 is the variance and can be approximated as,

$$\sigma^2 = \frac{\boldsymbol{\varepsilon^T \varepsilon}}{N - k} \tag{5.11}$$

Here N is the number of samples and k is the amount of parameters to be estimated. Though covariance and correlation are related, they are not equivalent. However, when using the standardized Information Matrix, i.e. the normalized Information matrix, the normalized covariance is calculated, which is a measure of correlation. Generally it is acceptable to assume that if the correlation between two parameters are greater than 0.9, there is a high degree of correlation and thus the estimated parameters might not be accurate.

5.2.3 Model fit statistics

A common measure used to determine how well the model fits the data is the coefficient of determination (R^2). The coefficient of determination is given by:

$$R^2 = \frac{\sum_{k=1}^{N}[\hat{z}(k) - \bar{z}]^2}{\sum_{k=1}^{N}[z(k) - \bar{z}]^2} = \frac{\widehat{\boldsymbol{\theta}}^T \boldsymbol{H}^T \boldsymbol{z} - N\bar{z}^2}{\boldsymbol{z}^T \boldsymbol{z} - N\bar{z}^2} \tag{5.12}$$

Here $\hat{z}$ represents the predicted output using the estimated model parameters $\widehat{\boldsymbol{\theta}}$, z is the measured data samples, $\bar{z}$ is the mean value of **z**, and N is the amount of samples. The R^2 statistic gives an indication of the proportion of the variation in the measured output **z** that is explained by the regression model. The larger the value of R^2 the better the model fit is. The coefficient lies between 0 and 1.

Some problems associated with this coefficient includes the fact that it tends to be overestimated when the number of samples is not large compared with the number of independent variables. Increasing the number of independent variables, even when they do not sufficiently influence the output of the estimator, still causes the coefficient of determination to increase.

In some cases, the adjusted coefficient of determination $AdjR^2$ is used, as it corrects for the number of parameters (p) being estimated, and does not necessarily increase when extra variables are added. The $AdjR^2$ is related to the R^2 by:

$$AdjR^2 = 1 - (1 - R^2)\frac{N - 1}{N - p - 1} \tag{5.13}$$

5.3 Optimal Input Design

The estimation of the stability and control derivatives is carried out primarily from the dynamic response of an aircraft to specific control inputs. It is thus important when designing the experiment, to excite the natural modes of the aircraft. If not properly excited, the measured variables do not contain enough information which in turn results in collinearity problems and incorrect parameter estimates.

This section explores different types of control inputs that are able to excite the aircraft dynamics for the purposes of SID.

5.3.1 Types of inputs

There are generally two approaches to designing inputs for System Identification purposes. The first approach is when it is assumed that no prior knowledge of the aircraft parameters or aircraft dynamics is known. In this case the control signals are chosen so that they excite a broad range of frequencies. These types of inputs include impulse inputs, frequency sweeps (such as Chirp or Fresnel chirp input signals) and multi-sine inputs. These inputs are generally more complex to implement and are not possible for a pilot to manually implement. For this reason, they have not been considered for use in this thesis.

The second approach is when it assumed that some information regarding the natural modes or eigenfrequencies of the aircraft are known. In this case control signals such as a pulse input, doublets or multi-step inputs are used. These inputs are designed to excite the aircraft around a specific frequency, and are explained more in detail below:

a. Pulse Input

The pulse input is the simplest type to excite the aircraft dynamics. It involves some control input for a specified period of time, after which the control is released (or returned to its previous state). This is indicated in the figure below:

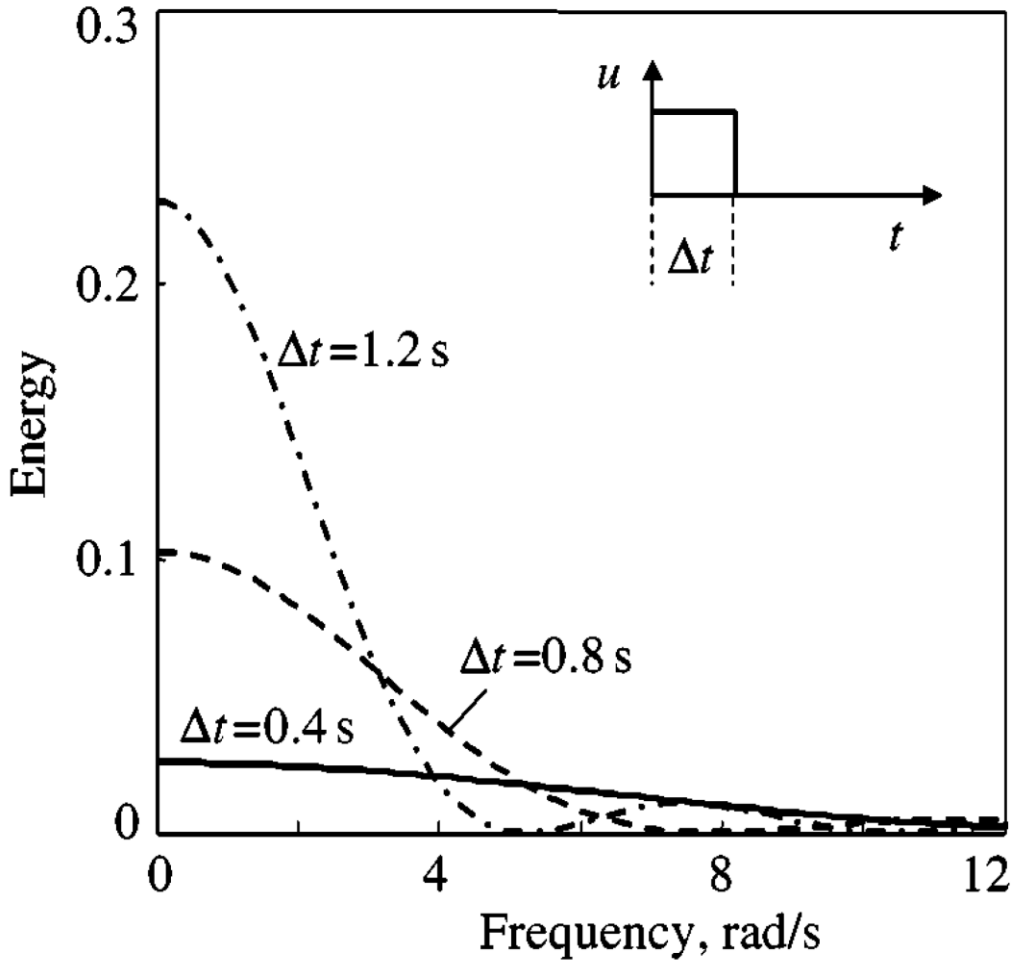

Figure 12: Energy Spectra of pulse inputs (Jategoankar, 1996)

The figure above also shows the energy spectra of a typical pulse input u for different pulse lengths Δt. There are two major points that need to be noted with regards to the energy spectrum of a typical pulse input, these include:

1. The greater the pulse length, the larger the input energy content but the lower the energy spread over the higher frequencies.
2. The pulse input has non-zero energy at the zero frequency. This is as a results of the pulse input being asymmetric about its starting trim value.

With these two points in mind, the pulse input is not ideal for use in a system identification framework. Considering point 1, for the faster or higher frequency modes of the aircraft like the short period mode or Dutch roll mode, the one would need a pulse input with a very short period. Though a pulse input with a short period will have an energy spread over the higher

frequencies, as indicated by the figure above, the energy content is low and in most cases proves not to be sufficient enough to excite the short period or Dutch roll modes.

The second consideration is the fact that a pulse input is asymmetric about the starting trim point. This can cause the aircraft's states to deviate from the initial trim conditions. Because the aircraft parameters to be determined are dependent on the trim condition, with a new trim position after the maneuver, the aircraft parameters will be different. In the case that this deviation is not too significant, this change can be shown to be insignificant and thus be ignored.

The energy spectrum of aseries of pulse inputs signal can be calculated as follows:

$$E(\omega) = 2\Delta t^2 \frac{2 - \cos\Omega}{\Omega^2}\left[\sum_{i=1}^{N} V_i^2 + \sum_{j=1}^{N-1} \cos j\Omega \sum_{i=1}^{N-j} V_i V_{i+j}\right] \tag{5.14}$$

Here $\Omega = \omega\Delta t$ is the normalized frequency, N is the number of pulses and V_i is the amplitude for the current pulse. This formula was derived in Jategoankar (1996), and can be used to determine the energy spectra of the Doublet input.

b. Doublet Input

The Doublet input is very similar to the pulse input, as it can be seen as a two sided pulse. For a doublet input, the control is moved abruptly in one direction, kept for a certain time period and then moved to another position (in the opposite direction) for the same period, before moving the control to its neutral position. A doublet and its energy spectrum is shown in the figure below:

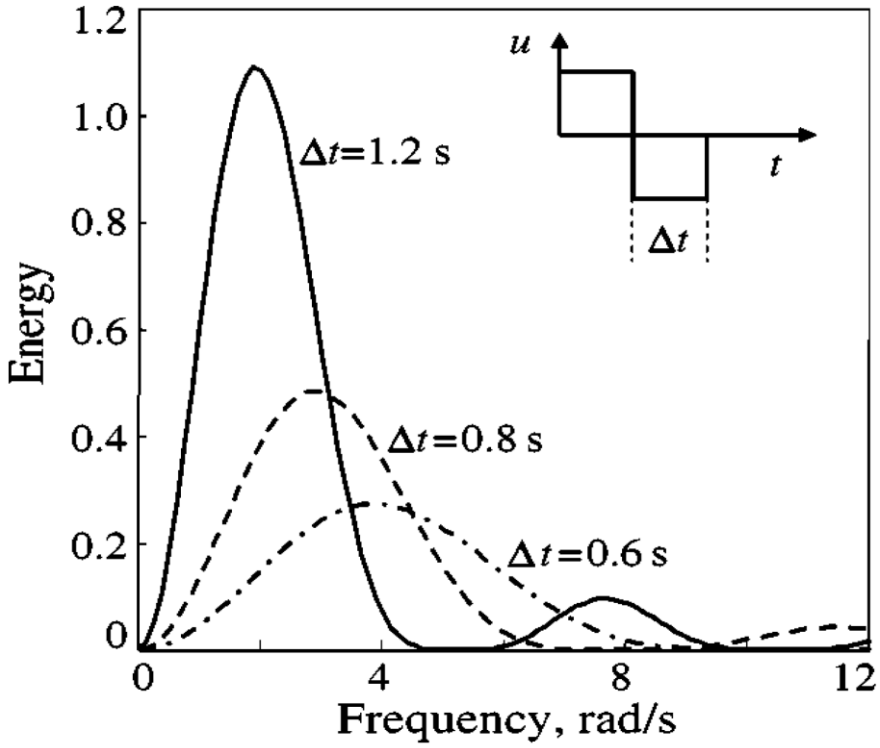

Figure 13: Energy Spectra of doublet inputs(Jategoankar, 1996)

Comparing the energy spectrum of a doublet input to that of the pulse input, there is one notable change. It can be seen that since the doublet is a symmetrical input, it results in an energy spectrum with zero energy at zero-frequency. This, as discussed earlier, is an ideal property.

Though the energy levels of a doublet input are much higher than those of a simple pulse input, they still have the same property in that the longer the pulse length the more concentrated the energy. For the longer period doublets, the energy content drops relatively fast around the peak. The shorter period doublet has a lower total energy, but the spread of energy across the frequency spectrum is greater than for a longer period doublet.

It is possible to relate the frequency at which the energy peaks to the period of the doublet. This can be done by looking at the normalized frequency spectra around the peak of a doublet input. This is shown below:

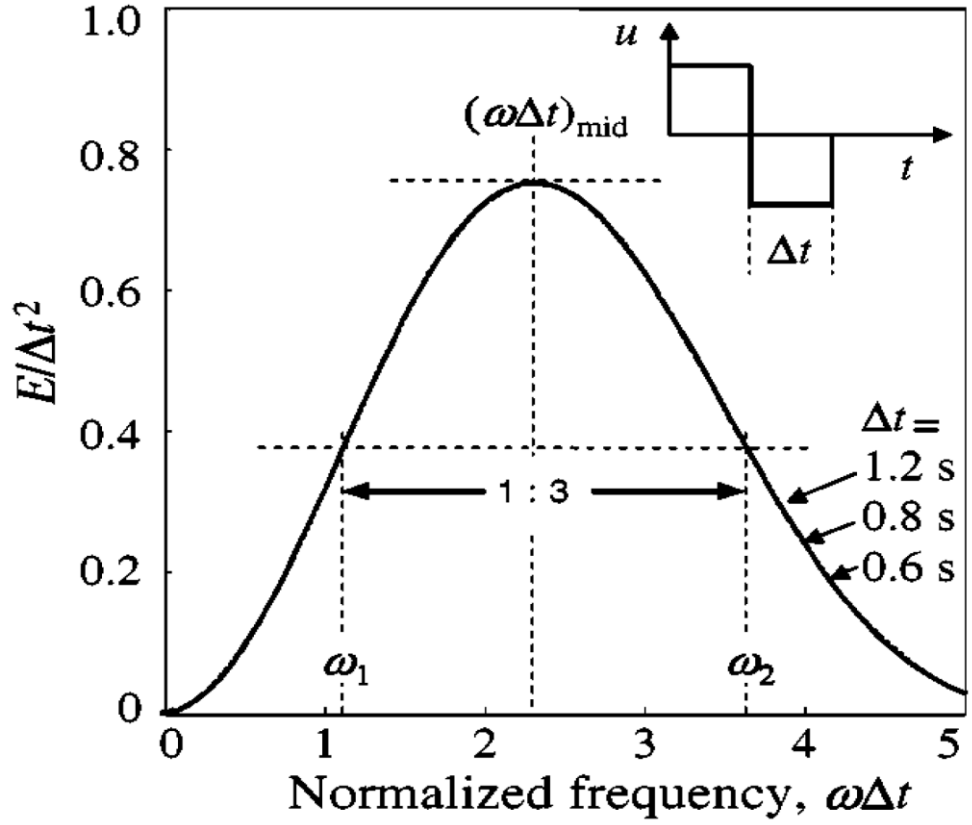

Figure 14: Normalized Energy Spectra of a Doublet (Jategoankar, 1996)

From this figure it is evident that the normalized frequency $\omega\Delta t$ for the peak is roughly 2.3. The time period of a doublet can be related to the normalized peak frequency as [12]:

$$\omega_n \Delta t \approx 2.3 \tag{5.15}$$

Therefore

$$\Delta t_{doublet} \approx \frac{2.3}{\omega_n} \approx \frac{2\pi}{2.7\ \omega_n} \approx \frac{1}{2.7} \text{ . period of oscilation} \tag{5.16}$$

Though Equation 5.16 shows that the period of the pulse is related to the peak frequency by a factor of 1/2.7, in practice the factor of 0.5 is generally used. In this case, the full period ($2\Delta t$) of the doublet is chosen to be equal to the period of the aircraft mode that is to be excited.

In Figure 14, the ratio 1:3 is an indication of the bandwidth. It is the ratio of upper and lower cut-off frequencies. These frequencies are indicated by ω_2 and $\omega_1$in the figure and are the frequencies at which the energy is half that of the peak energy.

c. Multistep Inputs

Extending the doublet input to include more pulses i.e. creating a multistep input, has further benefits. These benefits include increasing the bandwidth of the response of the input. What this means is that higher energy across a broader range of frequencies is achievable. One such multistep input, is the 3-2-1-1 input designed by Koehler (cited by Jategoankar (1996)). This input consists of alternating positive and negative pulses with relative periods of 3, 2, 1 and 1. The total period of the input is thus $7\Delta t$.

By comparing the energy spectra of a step input, a Doublet input and a multistep input, the increase in bandwidth is clearly evident. This is shown in the figure below:

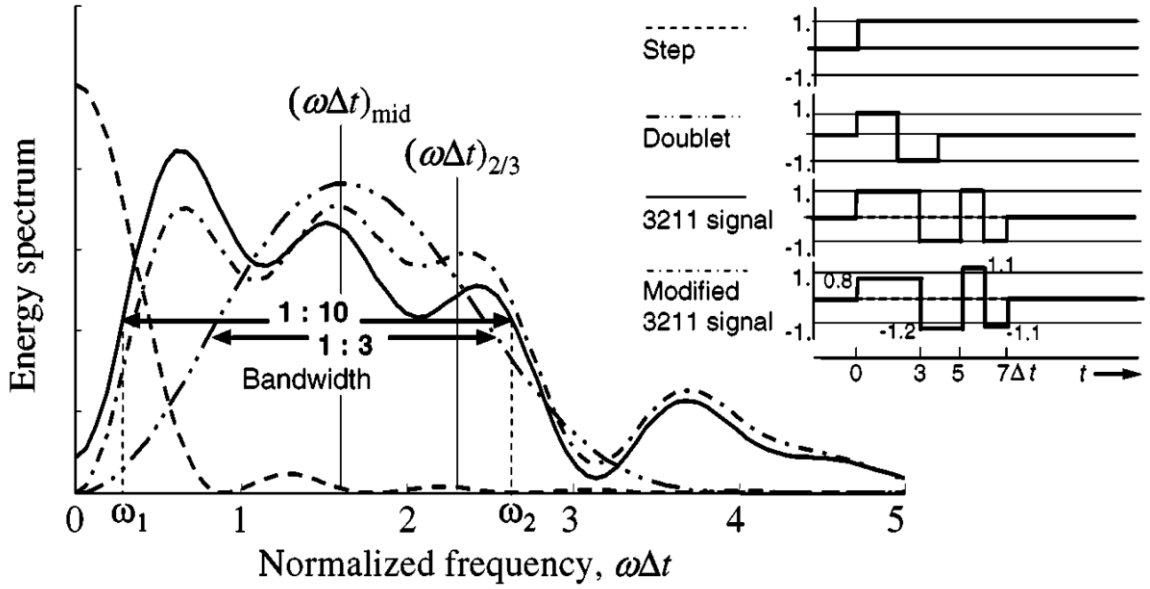

Figure 15: Energy Spectra Comparison (Jategoankar, 1996)

From the energy spectrum of the 3-2-1-1 multistep input, it must be noted that the response has non-zero energy at zero frequency. This shows that the input is asymmetrical about the trim condition. As discussed earlier this can cause the aircraft's trim conditions after the maneuver to differ from its initial trim condition. This effect can be minimized by modifying the 3-2-1-1 signal as shown in the figure above.

As a rule of thumb, time period for the 3-2-1-1 multistep input is given as

$$\Delta t_{3211} \approx \frac{1}{3} \,.\, \text{period of oscilation} \tag{5.17}$$

5.3.2 Natural Frequencies

To obtain good estimates of the aircraft parameters, it is necessary for the aircraft dynamics to be sufficiently excited. The best means to excite the aircraft dynamics is to excite the natural modes of the aircraft. This section describes the different modes of the aircraft.

a. The Short Period Mode

The short period mode, contains the pitch rate and angle of attack dynamics and can be described by the characteristic equation given by Peddle (2008) as,

$$p(s) = s^2 + \left(\frac{L_\alpha}{m\bar{V}} - \frac{M_Q}{I_{yy}}\right)s - \left(\frac{L_\alpha}{m\bar{V}}\frac{M_Q}{I_{yy}} + \frac{M_\alpha}{I_{yy}}\right) \tag{5.18}$$

The natural frequency of the short period mode can thus be estimated as:

$$\omega_{n\ (short\ period\ )} = \sqrt{-\left(\frac{L_\alpha}{m\bar{V}}\frac{M_Q}{I_{yy}} + \frac{M_\alpha}{I_{yy}}\right)} \tag{5.19}$$

Where

$$L_\alpha = qSC_{L_\alpha} \tag{5.20}$$

$$M_Q = qS\bar{c}\frac{\bar{c}}{2\bar{V}}C_{m_Q} \tag{5.21}$$

$$M_\alpha = qS\bar{c}C_{m_\alpha} \tag{5.22}$$

It must be noted that the resonant frequency of the short period mode is dependent on not only the parameters that make up the aircraft model, but also the airspeed $\bar{V}$ as well as the dynamic pressure q. This entails that when exciting the short period mode, the velocity of the aircraft as well as its altitude should remain relatively constant.

The short period mode is generally excited by means of the 3-2-1-1 multistep input as described, although the doublet input is also often used, mainly due to its simplicity.

b. The Roll Mode

The roll mode is excited through a bank-to-bank maneuver (also referred to as a rapid-roll maneuver). This maneuver consists of a series of aileron pulses that causes the aircraft to roll to a bank angle, followed by rolling in the opposite direction to the same bank angle before returning to a wings-level condition. The roll dynamics of a typical aircraft is given by Peddle (2008) as:

$$\dot{P} = \left[\frac{L_P}{I_{xx}}\right] P + \left[\frac{L_{\delta_A}}{I_{xx}}\right] \delta_A + \left[\frac{L_{\delta_R}}{I_{xx}}\right] \delta_R \tag{5.23}$$

Where

$$L_P = qSb\frac{b}{2\bar{V}} C_{l_P} \tag{5.24}$$

$$L_{\delta_A} = qSbC_{l_{\delta_A}} \tag{5.25}$$

$$L_{\delta_R} = qSbC_{l_{\delta_A}} \tag{5.26}$$

Given the above equation, the natural frequency of the roll mode can be given by:

$$\omega_{n\ (roll\ mode\ )} = \sqrt{-\frac{L_P}{I_{xx}}} \tag{5.27}$$

or

$$\omega_{n\ (roll\ mode\ )} = \sqrt{-\frac{\rho\bar{V}Sb^2C_{l_P}}{4I_{xx}}} \tag{5.28}$$

According to Jategoankar (1996), the doublet is generally the preferred input choice (over the multistep input) for roll mode excitation.

c. The Dutch Roll Mode

The Dutch roll mode is a mode that encapsulates the side-slip and lateral acceleration dynamics of an aircraft. This mode is generally excited by means of rudder inputs. The characteristic equation pertaining to this mode is given by

$$p(s) = s^2 + \left(\frac{Y_\beta}{m\bar{V}} + \frac{N_R}{I_{zz}}\right)s + \left(\frac{Y_\beta}{m\bar{V}}\frac{N_R}{I_{zz}} + \frac{N_\beta}{I_{zz}}\right) \tag{5.29}$$

Where

$$Y_\beta = qSC_{y_\beta} \tag{2.30}$$

$$N_R = qSb\frac{b}{2\bar{V}}C_{n_R} \tag{5.31}$$

$$N_\beta = qSbC_{n_\beta} \tag{5.32}$$

Given the above equation, the natural frequency of the Dutch roll mode can be given by:

$$\omega_{n\ (Dutch\ roll\ mode)} = \sqrt{\left(\frac{Y_\beta}{m\bar{V}}\frac{N_R}{I_{zz}} + \frac{N_\beta}{I_{zz}}\right)} \tag{5.33}$$

Or

$$\omega_{n\ (Dutch\ roll\ mode)} = \bar{V}\sqrt{\left(\frac{(\rho Sb)^2 C_{y_\beta} C_{n_R}}{8mI_{zz}} + \frac{\rho SbC_{n_\beta}}{2I_{zz}}\right)} \tag{5.34}$$

The Dutch roll mode can be excited by means of a rudder doublet input as this mode is relatively lightly damped. This mode is typically excited so that the variation in the angle of side slip is in the order of ± 4 deg or 0.1g lateral acceleration.

5.3.3 Considerations

The previous sections covered the design of control inputs that will excite specific dynamic modes of an aircraft. Exciting these modes are key to estimating the aircraft parameters. The better the mode is excited, the better the estimate of the parameters that pertain to that mode.

It must be noted that when exciting the modes, the variations in the angle of attack and angle of sideslip should not render the aircraft unstable. The variation of these parameters, about the trim condition, should be kept within ± 4 deg.

The excitation of the modes should also be done independently. This is to ensure that the effects of the other modes do not influence the estimate of the parameters being estimated. In the development of the model used for System Identification, many assumptions (refer to Peddle (2008)) have been made with regards to cross-coupling terms that couple the longitudinal dynamics (the dynamics that pertain to the angle of attack and pitch rate) and the lateral dynamics (the dynamics that pertain to the angle of sideslip, roll and yaw rates). To ensure that these assumptions hold, during a certain mode excitation, the other modes should be suppressed by means of implementing a control algorithm i.e. during a short-period mode excitation, the roll mode and Dutch-roll mode will be suppressed by means of a control system.

Though only the short-period mode, the roll mode and the Dutch roll mode have been mentioned, there does exist 2 other modes, the phugiod or long-period mode and the spiral mode. The phugoid mode is a long-duration mode that describes the velocity dynamics of the aircraft. Aircraft parameters associated with this mode is primarily those related to aircraft lift and aircraft drag. This mode can be excited by means of an elevator pulse or through thrust variations.

The spiral mode, is a slow lateral mode, linked to the yaw-dynamics of the aircraft. The spiral mode is generally stabilized through aircraft design and is not excited in System Identification schemes.

Chapter 6

Angle of Attack Estimation and Sensing

The angle of attack (AoA) and angle of sideslip are important states required for system identification. This chapter provides two methods of obtaining the angle of attack, (1) through the design of an AoA probe and (2) through estimation.

6.1 Sensor Design

This chapter discusses the design and calibration of an angle of attack sensor needed for system identification. Though angle of attack sensors are available for commercial aircrafts as well as for larger UAVs, these sensors are not well suited for smaller UAVs such as those used at the ESL.

The reasons why these commercially available sensors are not well suited for the application of this thesis include:

1. The sensors are too expensive.
2. The sensors are too large, and thus will have an effect on the dynamics of flight.
3. Commercial sensors commonly have heating elements and thus require large power sources.

Given the abovementioned reasons, an AoA sensor was designed. For the design of the AoA sensor, several different sensing devices were considered. These devices include:

1. Pivoted vanes
2. Differential pressure probes

Of the above mentioned sensing devices, the pivoted vane is the most common device and can be seen on many commercial aircrafts. The differential pressure probe on the other hand is more commonly used on smaller UAVs such as the M^2AV Carolos [29,30,31] and NASA EAV002 [32].

More complicated systems such as the null-seeking differential pressure tube, used almost exclusively in the service operation of aircrafts, do exist but have not been considered due to their complexity[33].

a. Pivoted Vanes

A pivoted vane is a mass balanced wind vane that is free to align itself in the direction of airflow. Connected to this vane is an angular displacement sensor, which measures the change in angular displacement of the vane in the presence of airflow. A typical AoA sensor with an imbedded angular displacement sensor is show below.

Figure 16: Pivoted Vane for AoA sensing (Photo by Francois Roche)

By aligning itself with the wind vector, the vane is able to determine the relative angular displacement of the wind vector relative to the aircrafts body. Thus with the vane mounted perpendicular to the X_b-axis, the angle of attack can be determined.

Advantages of using a Pivoted Vane

- Because of the simple manner in which the vane operates, it can be easily incorporated into any existing aircraft system.
- The system consists of one sensor which needs to be calibrated together with the vane; this simplifies the calibration process.

Disadvantages of using a Pivoted Vane

- Asymmetry of the vane because of manufacturing defects will cause the vane to be aerodynamically imbalanced resulting in floating angles.
- If mounted on a boom, any flow distortions caused by the boom will result in inaccurate readings. The bending of the boom support due to air loads, will also influence the measured reading.
- If mounted onto the fuselage of the aircraft, flow distortions caused by the fuselage will influence the flow field around the sensor, causing inaccuracies in the measurement.

b. Differential Pressure probe

AoA sensors using differential pressure tubes make use of two orifices located at equal angles on either side of the longitudinal axis of the sensor. By measuring the difference in pressure across these two orifices, in the presence of airflow, the angle of attack can be determined.

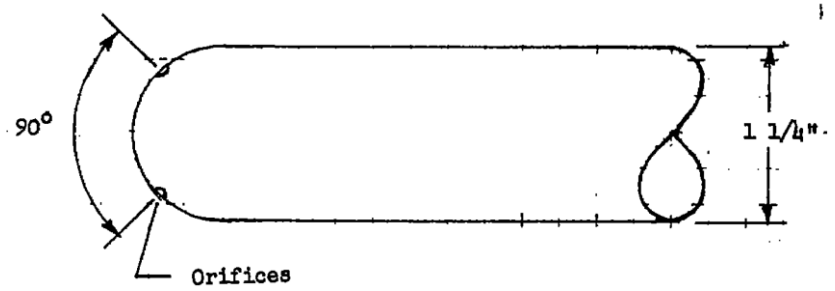

Figure 17: Illustration of a differential pressure probe

The magnitude of this pressure difference is dependent on the Mach number, the Reynolds number, the relative angle between the orifices as well as the shape of the nose of the tube. Gracey (1958) describes the effects of these dependencies on the measured angle of attack.

Advantages of using differential pressure probe

- The probe can be easily and cheaply manufactured.
- The probe can be easily mounted onto any aircraft.
- The probe can be easily calibrated in a small wind-tunnel.

Disadvantages of using differential pressure probe

- In order to minimize the effect of the change in velocity on the AoA measurement, more than one pressure transducer is required. This results in a longer calibration process than that of the pivoted vane.

6.1.1 Probe Design

Due to the ease of its construction, and the ease of implementing the system into the current avionics pack, the differential-pressure-probe type sensor was chosen.

A 3-hole pressure probe was designed, consisting of 3 alluminium tubes mounted on top of each other, with their longitudinal axes parallel (as shown in Figure 18). The outer tubes were cut at 45 degrees as it was shown according to Gracey (1958) that when the orifices are at 90 degrees with respect to each other, the best combination of sensitivity and resolution can be achieved.

Figure 18: AoA probe mounted on the aircraft

6.1.2 Avionics and Sensors

This section discusses the hardware required for the measuring of the AoA. A block diagram overview of the system is shown in Figure 19.

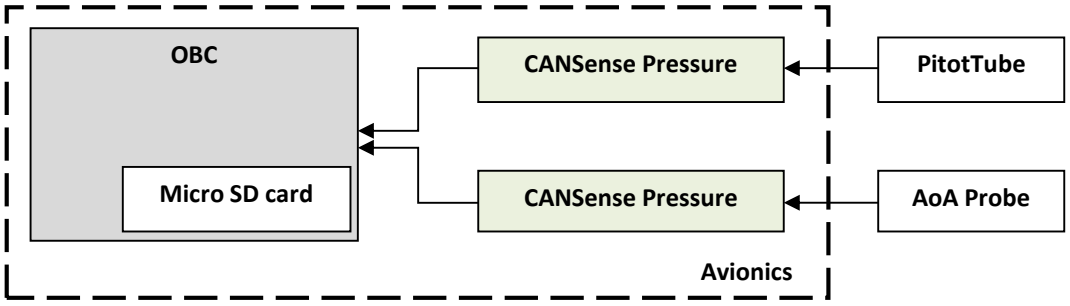

Figure 19: Overview of the Avionics used for AoA Sensoring

As can be seen from Figure 19, the avionics pack used for angle of attack sensoring comprises of two main components: the OBC and the CANSense pressure board. In the sections to follow a brief overview of these two components will be given. Refer to Hough (2007), for a full description of these components.

CANSense Pressure Board

The CANSense pressure board is used to convert the pressure readings measured by the Pitot tube and AoA probe into analog signals. These analog signals are then sent to the CANSense Base board, which performs the digitilisation of the signals, via the CAN bus to the OBC (SensorBoard).

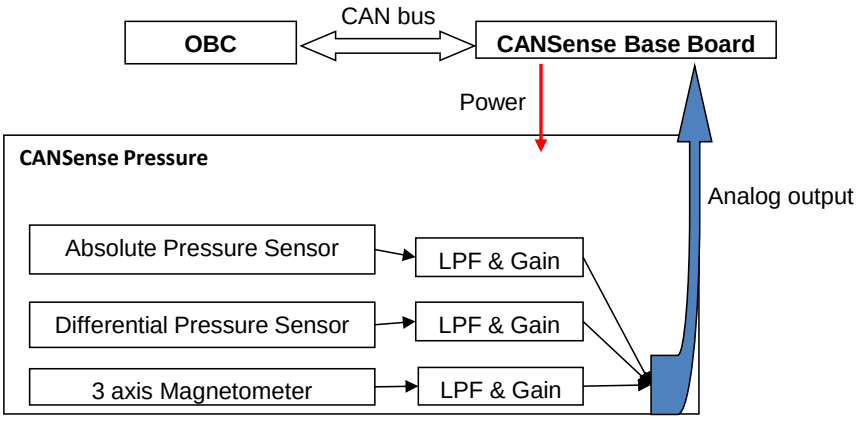

Figure 20: Conceptual operation of CANSense Pressure board

The CANSense Pressure board consists of:

- 1 Absolute Pressure sensor (MPXA4115A)
- 1 Differential Pressure sensor (MPXV5004G)
- 1 Magnetometer

Before the measurements of the above mentioned sensors are sent to the OBC, the signals are conditioned. The pressure sensors are filtered at 588Hz to reduce the high frequency noise and are then multiplied by a gain of 0.819 as the ADC (analogue to digital converter) on the CANSense Base board has a voltage reference of 4.0964V. The magnetometer's outputs are filtered at 103Hz and multiplied by a gain of 3. This output swings about a reference voltage supplied by the magnetometer, and the difference between the reference voltage and output is amplified by a gain of 0.819 as in the case of the pressure sensors.

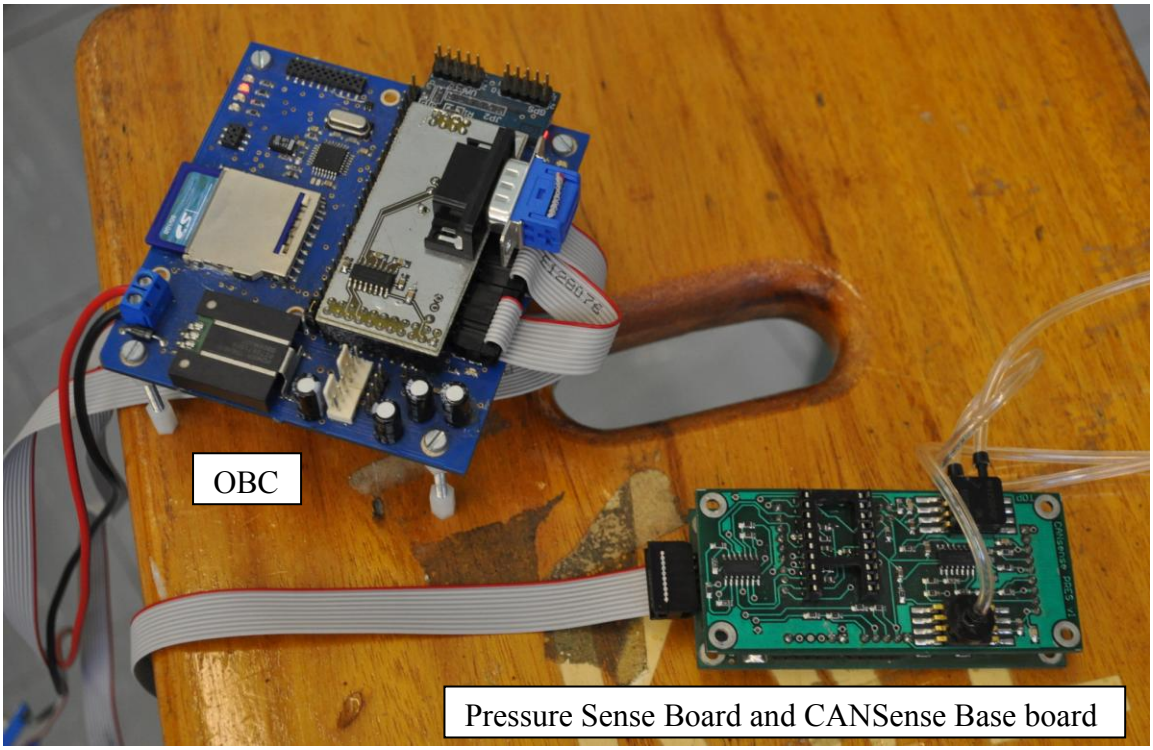

Figure 21: Pressure Sense board and OBC

For the purpose of AoA sensing, only the differential pressure sensors on the CANSense pressure board are used. The aircrafts used at the ESL currently have a pressure board which is used for the calculation of the airspeed and altitude and thus only one extra pressure board is required.

OBC (onboard computer)

Once the sensor measurements are digitalized they are sent via the CAN bus to the OBC as indicated in Figure 21. The OBC then processes the measurement into pressure readings which are either logged directly onto a Micro SD card for post processing, or used for the online determination of the AoA.

6.2 AoA Calibration

The AoA sensor was calibrated in the wind-tunnel of the M&M department at Stellenbosch University. This section covers the calibration procedure followed and is divided into 4 sections: the calibration procedure overview, the formulation of the calibration curves, the wind-tunnel setup and finally the results obtained after calibration.

6.2.1 Calibration Procedure Overview

The calibration was done at 5 different wind speeds, with the probe calibrated over an angular range of $-20°$ to $20°$. At each wind speed the probe was rotated through its full angular range with increments of $5°$, while recording pressure data at each angle. No dynamic effects of angular change was tested or characterized, as the probe's angular orientation was set manually and the data recorded was taken while the probe was static. A flow diagram of the calibration procedure is shown below.

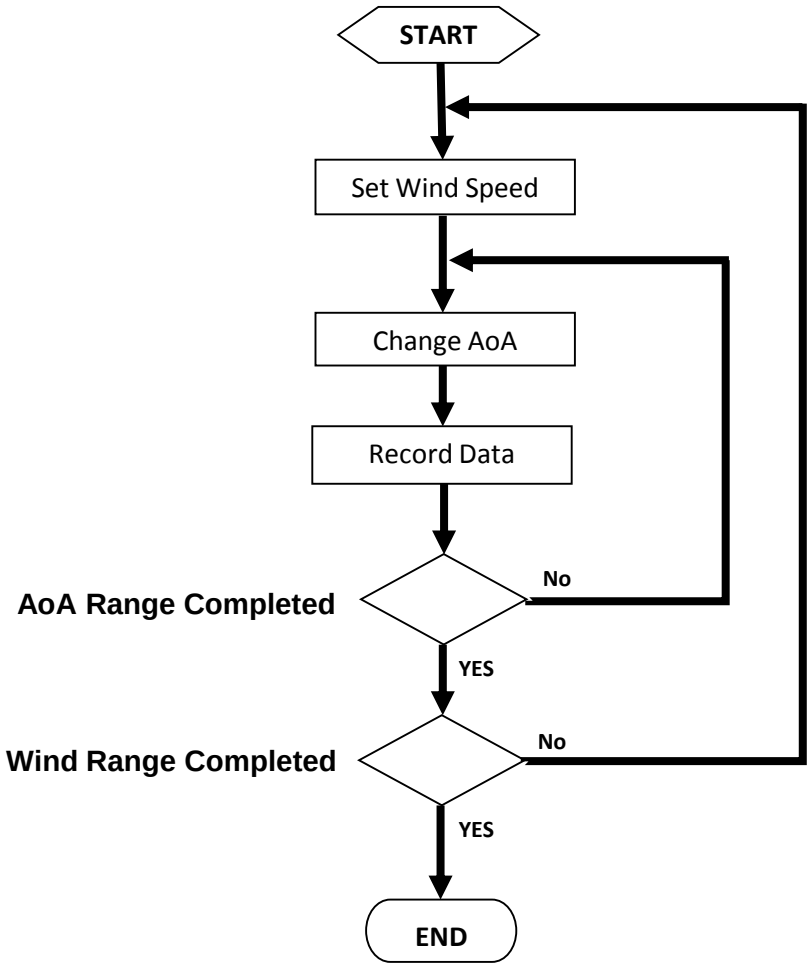

Figure 22: Flow diagram of AoA calibration procedure

6.2.2 Formulation of the Calibration Curves

It has been shown in Gracey (1958), Jategaonkar (1996) and Ippolito (2006) that there exists a fairly linear relationship between the pressure difference across the orifices on the AoA probe and the angular orientation of the probe itself. It has been further shown that by scaling this pressure difference (ΔP) with the dynamic pressure (q) measured by the pitot tube, the measurement of the AoA can be made less dependent on the wind velocity.

The resulting expression for the AoA as a function of the pressure difference and dynamic pressure is shown below:

$$\alpha = K_\alpha \frac{\Delta P}{q} + C_\alpha \tag{6.1}$$

Where K_α is the proportional constant and C_α is the zero bias caused by inaccuracies in the probe construction and pressure sensor biases.

6.2.3 Wind-Tunnel Setup

The following apparatus' were used in the calibration of the AoA sensor:

- Wind-Tunnel with variable speed drive
- Bets Micro-manometer
- Pitot Static Tube
- AoA probe
- AoA calibration rig
- CANSense Pressure board
- OBC and voltage supply
- Thermometer
- Mercury Barometer
- Laptop running the ground station

The Bets Micromanometer, the thermometer and the mercury barometer were used to calibrate the pressure transducers of the CANSense Pressure board and to determine the wind speed in the wind-tunnel. Figure 23 and Figure 24 shows the wind-tunnel with the variable speed drive and calibration setup respectively.

Figure 23: Wind-tunnel with variable speed drive

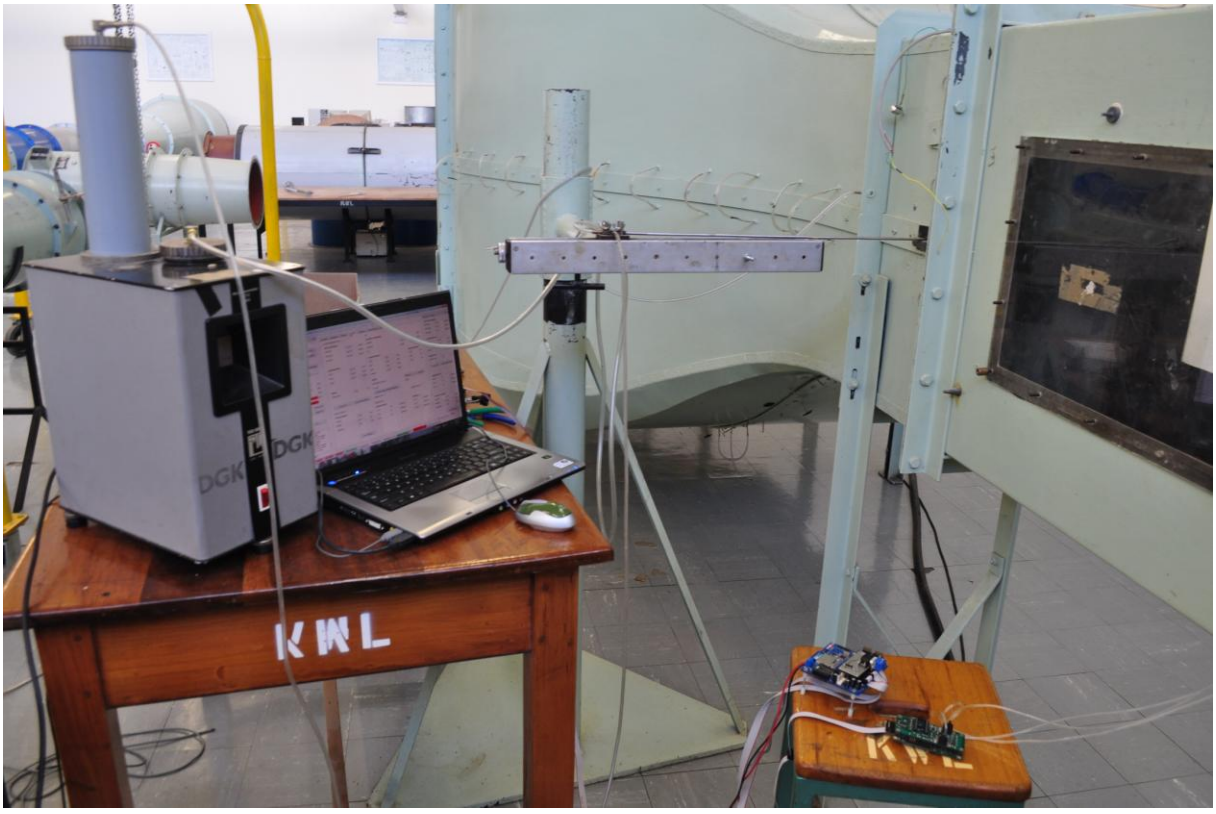

Figure 24: Calibration setup

The AoA calibration rig was designed such as to have minimal interference or obstruction to the flow in the wind-tunnel in which it was mounted. The calibration rig allowed the AoA probe to be swept through the angular range $-20°$ to $20°$, at intervals of $5°$. Figure 25 shows the calibration rig in the wind-tunnel.

Figure 25: AoA calibration rig in the wind-tunnel

6.2.4 Calibration Results

The calibration process was carried over a 3 day period. Due to improper setup on the first day, the results obtained over the last 2 days are shown in the figure below:

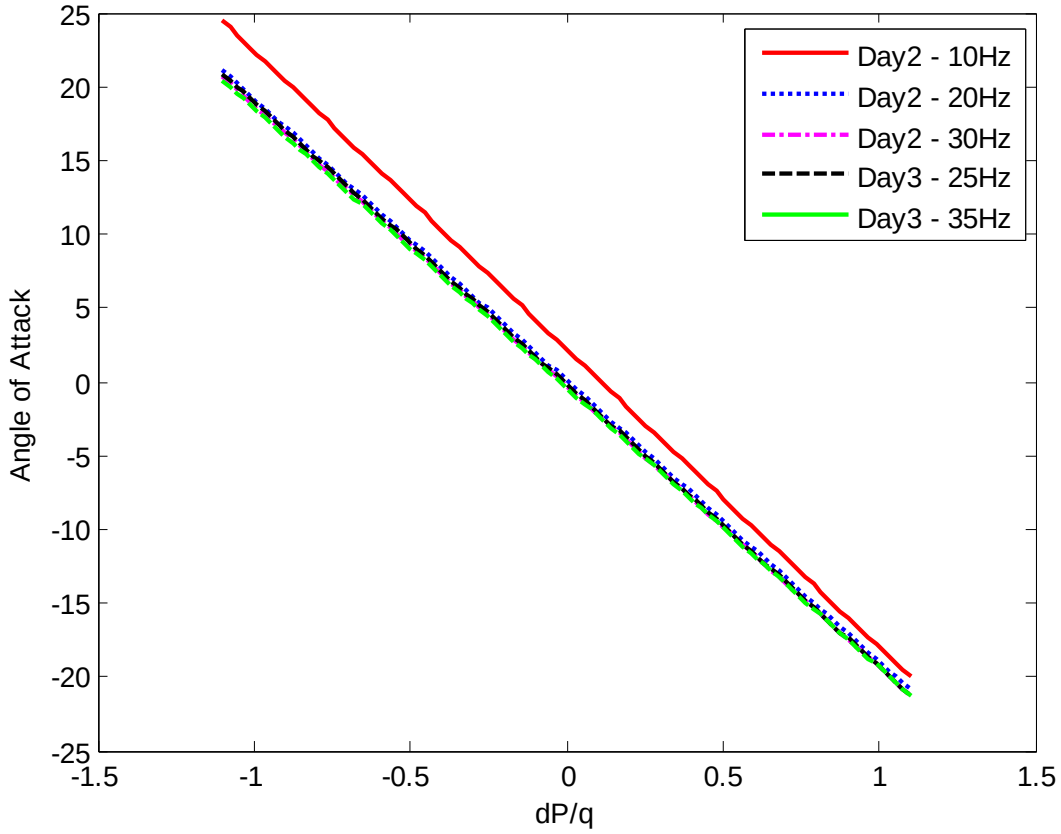

Figure 26: Calibration Curves

Here, the variac setting relates to the measured airspeed as follows:

Variac Setting	Measured Airspeed
Day 2 – 10 Hz	7.5 m/s
Day 2 – 20 Hz	15.6 m/s
Day 2 – 30 Hz	23.7 m/s
Day 3 – 25 Hz	20.0 m/s
Day 3 – 35 Hz	28.1 m/s

Table 1: AoA calibration speeds

It can be seen from Figure 26, the curves obtained for each experiment match well with each other, except for the curve obtained at 10Hz. At this variac setting (10Hz) the airspeed was measured to be approximately 7.5 m/s. Because the cruise speed of the aircrafts being considered for SID is much higher than 7.5m/s, it was decided to ignore this curve. Comparing the rest of the curves, these results also compare well with the calibration curves in Gracey (1958). The final curve used for angle of attack sensing takes into consideration the whole range of tests and is also plotted below:

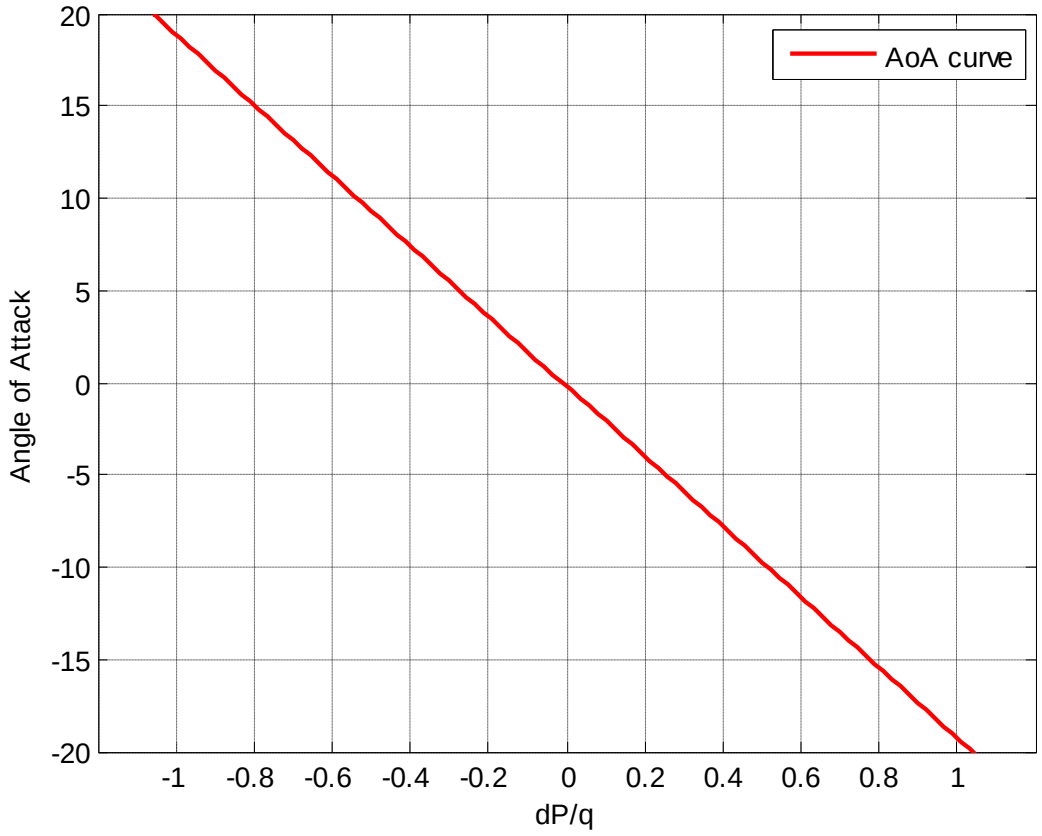

Figure 27: Final calibration curve

To quantify the accuracy of the sensing system, the following needs to be taken into account:

1. The variation in the zero measurement bias (C_α)
2. The variation in the gradients of the calibration curves (K_α)
3. The variation in AoA measurement due to sensor noise.

To quantify the above, a closer look at the calibration curves of Figure 26 is needed. Figure 28 shows the curve zoomed in about zero differential pressure ($\Delta P = 0$).

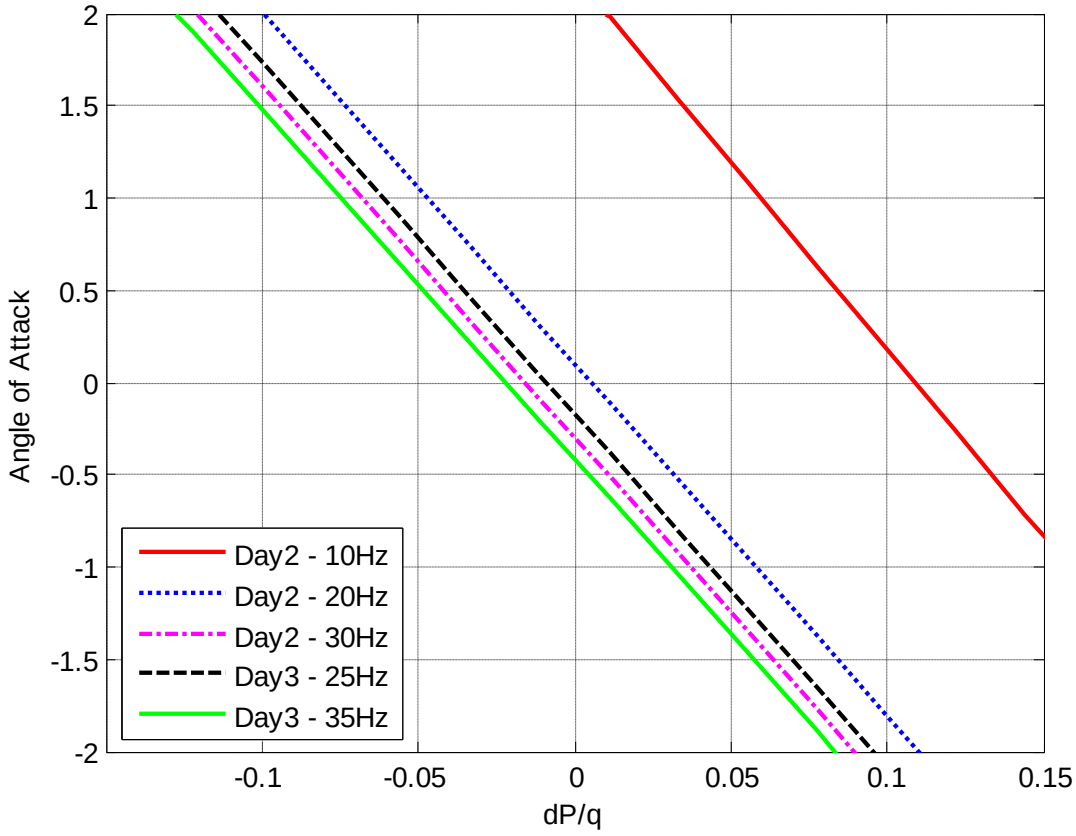

Figure 28: Calibration curves zoomed in about ΔP=0

The following statistics have been obtained from the measured data:

Parameter	Min	Max	Mean	Std.
C_α	-0.4177	0.1039	-0.1955	0.233
K_α	-19.127	-18.939	-19.039	0.0784

Table 2: AoA curve statistics

Note that the statistics ignore the data obtained from the 10Hz curve.

The variation in the AoA measurement due to sensor noise can be seen on the following figure. The figure shows how the measured AoA varies when the AoA probe is kept at static angle of 10° with a wind speed of 20 m/s.

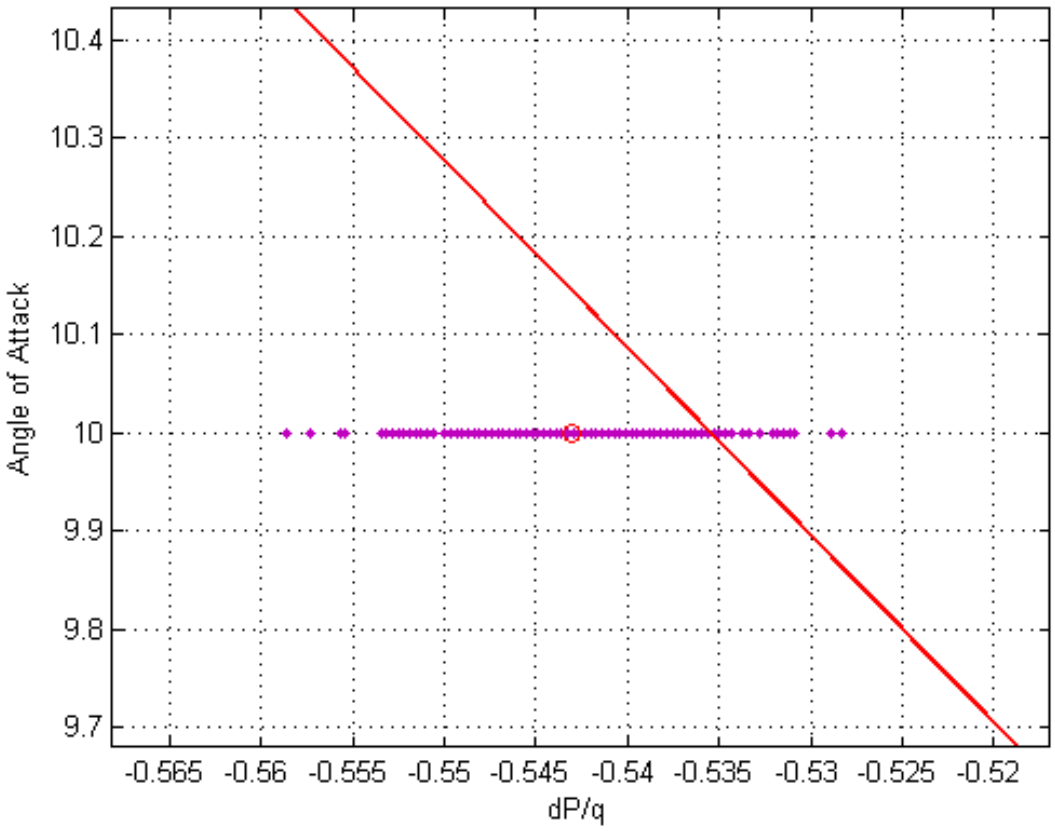

Figure 29: Variation in pressure readings at 10deg

From the figure above it can be seen that the measured quantity dP/q, has a standard deviation of 0.0049 with a bias error (relative to the calibration curve) of 0.08 when the probe is kept at 10°. This deviation is fairly constant across the whole measurement range of AoA, but the bias error increases as the measured AoA reaches the extremes of its measuring range ($-20°$and $20°$). The variation in the pressure readings results in a variation of about 0.6 degrees in the angle of attack measurement.

6.2.5 Summary

Subsection 6.3 covered the calibration of the AoA measuring system. From the wind-tunnel tests the following calibration curve was derived:

$$\alpha = -19.039\frac{\Delta P}{q} - 0.1955 \tag{6.2}$$

It was also shown that the variation in AoA due to measurement noise was approximately 0.6 degrees. Though higher accuracy commercial angle of attack sensors are available, the

variation and the bias errors associated with the angle of attack measurements presented in this section were found to be acceptable for the intended purpose of the AoA probe.

To increase the accuracy of the AoA sensoring system, the following can be done:

1. Replace the pressure transducers of the CANSense Pressure board with transducers that have less noise
2. Use better machining methods for the manufacturing of the AoA probe.

6.3 Estimator Development

Two approaches are taken to estimate the AoA. The first approach is based on an estimator derived from an aerodynamic stand point, the second approach is based on the kinematic relationship between the AoA and other measured aircraft states.

6.3.1 Aerodynamic Based Estimator

Few texts cover the estimation of AoA using an aerodynamic model. The lack in popularity of this method can be attributed to the fact that the accuracy of the estimate is highly dependent on the aerodynamic model of the aircraft, specifically the longitudinal dynamics. The aerodynamic coefficients are merely linear approximations and constantly change over the flight envelope of a conventional aircraft. This in turn introduces uncertainty into the estimated AoA.

The aim of this chapter is to develop an estimator that is robust to changes in the aerodynamic model of the aircraft as well as biases and noise on measurements that form part of the estimation process. The main reason for developing an AoA estimator is that the AoA probe has only been tested and calibrated statically and thus to obtain the dynamic response to the change in AoA, an estimator is required.

a. Estimator Dynamics

The longitudinal dynamics of a conventional aircraft have two different modes. These modes, which include the short-period and phugoid (long-period) mode have different bandwidths. Of these two modes the faster short-period mode contains the AoA dynamics needed for the derivation of the estimator.

The short period mode can be described as a damped pitching oscillation about the Y_B axis. One characteristic of this mode is that when disturbed, the speed of the aircraft remains approximately constant. This is due to the inertial and momentum effects of the aircraft which ensures that the speed response in the time scale of this mode is negligible.

Assuming that the velocity as well as the attitude of the aircraft is constant over the time-scale of the short period mode, the following equation (as derived in Peddle, 2008) describing the short period mode or normal dynamics is derived.

$$\begin{bmatrix}\dot{\alpha}\\ \dot{Q}\end{bmatrix} = \begin{bmatrix}-\frac{qS}{mV}C_{L_\alpha} & 1-\frac{qS}{mV}\frac{c}{2V_a}C_{L_Q}\\ \frac{qSc}{I_{yy}}C_{m_\alpha} & \frac{qSc}{I_{yy}}\frac{c}{2V_a}C_{m_Q}\end{bmatrix}\begin{bmatrix}\alpha\\ Q\end{bmatrix} + \begin{bmatrix}-\frac{qS}{mV}C_{L_{\delta_E}}\\ \frac{qSc}{I_{yy}}C_{m_{\delta_E}}\end{bmatrix}\delta_E + \begin{bmatrix}-\frac{qS}{mV}C_{L_0}\\ \frac{qSc}{I_{yy}}C_{m_0}\end{bmatrix} + \begin{bmatrix}\frac{g}{V}\\ 0\end{bmatrix}e_{33}^{WI} \quad (6.3)$$

Here e_{33}^{WI} is an element of the inertial to wind axes DCM, where the DCM is given as:

$$\boldsymbol{DCM^{WI}} = \begin{bmatrix}e_{11}^{WI} & e_{12}^{WI} & e_{13}^{WI}\\ e_{21}^{WI} & e_{22}^{WI} & e_{23}^{WI}\\ e_{31}^{WI} & e_{32}^{WI} & e_{33}^{WI}\end{bmatrix} \quad (6.3)$$

b. Output Equations

The output equations for AoA estimation are determined by the available measurements. In addition to the newly designed angle of attack sensor, the avionic system includes a pitch rate (Q) measurement, obtained from the gyroscopes, and a normal acceleration measurement (C), obtained by the accelerometers.

Since the angle of attack and pitch rate are states of the normal dynamics, only the normal acceleration needs to be defined in terms of the given states. According to [3], the normal acceleration coordinated in the wind axis system can be represented by:

$$C_W = \begin{bmatrix}-\frac{qS}{m}C_{L_\alpha} & -\frac{qS}{m}\frac{c}{2V_a}C_{L_Q}\end{bmatrix}\begin{bmatrix}\alpha\\ Q\end{bmatrix} + \begin{bmatrix}-\frac{qS}{m}C_{L_{\delta_E}}\end{bmatrix}\delta_E + \begin{bmatrix}-\frac{qS}{m}C_{L_0}\end{bmatrix} \quad (6.19)$$

The normal acceleration C_W can be related to the acceleration as measured by the accelerometers in the body axis as follows:

$$\begin{bmatrix}A_w\\ B_W\\ C_w\end{bmatrix} = DCM^{WB} \times \begin{bmatrix}A\\ B\\ C\end{bmatrix} \quad (6.20)$$

Where A_W, B_W and C_W are the axial, side and normal velocity in the wind axis respectively, DCM^{WB} is the directional cosine matrix relating the body axis to the wind axis and A, B and C are the accelerations in the body axis.

With the DCM^{WB} represented as:

$$DCM^{WB} = \begin{bmatrix} \cos\alpha\cos\beta & \sin\beta & \sin\alpha\cos\beta \\ -\cos\alpha\sin\beta & \cos\beta & -\sin\alpha\sin\beta \\ -\sin\alpha & 0 & \cos\alpha \end{bmatrix} \tag{6.21}$$

The normal acceleration in the wind axis as a function of the accelerometer readings in the body axis can be formulated as:

$$C_w = -A\sin\alpha + C\cos\alpha \tag{6.22}$$

Thus for small angle of attacks the normal acceleration in the wind axis can be approximated as the normal acceleration as measured by the accelerometers in the body axis

$$\therefore\ C_w \cong C \tag{6.23}$$

Therefore given the normal acceleration, the pitch rate and the angle of attack the full output equation is given as:

$$y = \begin{bmatrix} C \\ Q \\ \alpha \end{bmatrix} = \begin{bmatrix} -\frac{qS}{m}C_{L_\alpha} & -\frac{qS}{m}\frac{c}{2V_a}C_{L_Q} \\ 0 & 1 \\ 1 & 0 \end{bmatrix} \begin{bmatrix} \alpha \\ Q \end{bmatrix} + \begin{bmatrix} -\frac{qS}{m}C_{L_{\delta_E}} \\ 0 \\ 0 \end{bmatrix} \delta_E + \begin{bmatrix} -\frac{qS}{m}C_{L_0} \\ 0 \\ 0 \end{bmatrix} \tag{6.24}$$

c. Discretization

Though the continuous estimator model as presented in Section 6.3.1a and 6.3.1b is sufficient for simulation purposes, it is desirable for a discrete equivalent to be derived. The discrete equivalent makes running the estimator on the OBC of the aircraft a possibility.

The MATLAB function **c2d** is a means by which the discrete equivalent can be derived before implementing the estimator on the avionics. This however is not ideal as the estimator model is a function of the airspeed and dynamic pressure, which vary during a typical flight test. In order for the discretization process to be implemented online, the first order Taylor series approximation of the discretization process is proposed. The system matrices and bias terms can thus be discretized as follows:

$$\Phi = I + A\,T_s\left(I + A\frac{T_s}{2}\right) \tag{6.25a}$$

$$\Gamma = T_s\left(I + A\frac{T_s}{2}\right)B \tag{6. 25b}$$

$$Bias_d = T_s\left(I + A\frac{T_s}{2}\right)Bias \tag{6. 25c}$$

Where Φ is the discretized system matrix A. Γ is the discretized system matrix B and $Bias_d$ is the discretized bias terms

Though the estimator model is dependent on the airspeed and dynamic pressure, the model can be made independent of these parameters. A method proposed by Peddle 2008, in which Normalized Non-dimensional Time (NNDT) is used to assure this independence can be used to make the estimator applicable over the whole flight envelope of the aircraft.

d. Gain calculation

The dynamics and convergence of the estimator is highly dependent on the choice of gain. Optimal methods of obtaining the estimator gain do exist. This is commonly done by solving the Riccati equation as shown below.

$$P(k) = [M(k)^{-1} + H^T R_k^{-1} H]^{-1} \tag{6.26}$$

$$\mathrm{M(k+1)} = \Phi \mathrm{P(k)} \Phi^{\mathrm{T}} + \Gamma_1 \mathrm{Q_k} \Gamma_1^{\mathrm{T}} \tag{6.27}$$

Where $M(k)$ is the covariance matrix associated with the state estimate before the measurement update, and $P(k)$ is the covariance matrix associated with the state estimate after the measurement update.

The solving of the Riccati equation is computationally expensive and thus a modified version of the covariance update step is shown below. This method provides the optimal gain that ensures the minimal mean-square error estimate.

$$P(k) = M(k) - M(k)H^T[HM(k)H^T + R_k]^{-1}HM(k) \tag{6.28}$$

$$M(k+1) = \Phi \mathrm{P(k)} \Phi^{\mathrm{T}} + \Gamma_1 Q_k \Gamma_1^T \tag{6.29}$$

with the gain calculated as

$$L(k) = P(k)H^T R_k^{-1} \tag{6.30}$$

Given Equations 6.28 to 6.40, it must be noted that the gain calculation is dependent on both R_K and Q_K which are the noise and process covariance matrices respectively. The noise covariance matrix (R_K) is a known quantity determined by the sensor noise on the measurements, whereas the process noise covariance matrix (Q_K) is not known. The process noise matrix however can be used to tune the estimator. By tuning the estimator with the process noise, the estimator poles can be placed such that the desired estimator response is obtained. It must be noted that the gain obtained after this tuning process is now sub-optimal. Online methods of determining this unknown process noise has been presented in [39, 40] but is not covered in this thesis.

In order to quantify the effect that the change in process noise has on the estimator dynamics, it is necessary to look at the estimator pole locations as a function of the optimal steady state estimator gain. For SISO (single input, single output) systems it can be shown that the optimal estimator poles lie on the symmetric root locus defined by the characteristic equation:

$$1 + \frac{Q_k}{R_k} G_e(z^{-1}) G_e(z) = 0 \tag{6.31}$$

Where,

$$G_e(z) = H(zI - \Phi)^{-1}\Gamma_1 \tag{6.32}$$

And H is the output matrix, Φ is the discretized system matrix and $\Gamma_1$is the process noise gain matrix.

It should be noted that the estimator gain is determined using the system matrices. These matrices have been shown to be dependent on the dynamic pressure and airspeed. For a change in altitude or airspeed, the gain would thus have to be recalculated. In order to design an estimator that is independent of the dynamic pressure and airspeed .i.e. to operate over the whole flight envelope of the aircraft, the NNDT method as proposed by Peddle (2008) can be used.

Implementation of the estimator

The basic form of the AoA estimator can be derived using the discussions presented in the previous subsections (Section 6.3.1 through to Section 6.3.4). In its basic form the estimator is found to yield unsatisfactory results. The AoA measurement as derived through estimation is shown to be susceptible to bias errors in the presence of:

1. Sensor biases (pitch rate, and normal acceleration measurements)
2. Inaccuracies or deviations in the aerodynamic coefficients

In order to make the estimator immune or less susceptible to bias errors, the following methods are proposed:

1. Adding bias states to the estimator
2. Using the Proportional Integral form of the Kalman Filter

This section presents the pros, cons and limitations of the above-mentioned methods.

Bias estimation

In the presence of sensor biases, bias states can be added to the estimator. As the estimated AoA converges to the actual AoA, the bias states converge to the sensor biases. Bias terms can also be augmented to the state vector to account for changes or errors in the aerodynamic coefficients. The equations below show changes to the estimator model as a result of adding bias terms.

$$\begin{bmatrix} \dot{\alpha} \\ \dot{Q} \\ \dot{\Delta\alpha} \end{bmatrix} = \begin{bmatrix} -\frac{qS}{mV}C_{L_\alpha} & 1-\frac{qS}{mV}\frac{c}{2V_a}C_{L_Q} & \frac{qS}{mV}C_{L_\alpha} \\ \frac{qSc}{I_{yy}}C_{m_\alpha} & \frac{qSc}{I_{yy}}\frac{c}{2V_a}C_{m_Q} & -\frac{qSc}{I_{yy}}C_{m_\alpha} \\ 0 & 0 & 0 \end{bmatrix} \begin{bmatrix} \alpha \\ Q \\ \Delta\alpha \end{bmatrix} + \begin{bmatrix} -\frac{qS}{mV}C_{L_{\delta_E}} \\ \frac{qSc}{I_{yy}}C_{m_{\delta_E}} \\ 0 \end{bmatrix} \delta_E + \begin{bmatrix} -\frac{qS}{mV}C_{L_0} \\ \frac{qSc}{I_{yy}}C_{m_0} \\ 0 \end{bmatrix} + \begin{bmatrix} \frac{g}{V} \\ 0 \\ 0 \end{bmatrix} e_{33}^{WI} + \begin{bmatrix} 0 \\ 0 \\ 1 \end{bmatrix} \eta_{\Delta\alpha} \tag{6.33}$$

It must be noted the derivative of the bias terms are zero with just a noise component ($\eta_{\Delta\alpha}$). Gyroscopes and accelerometers have fairly constant biases or at most can be characterized as a random walk of low frequency. Using this property, the bias terms can be assumed to be

constant over the sampling period of the estimator and thus the derivative of the bias term can be approximated as just the noise.

The amount of bias terms that can be augmented into the estimator is however limited by the amount of sensors available and the observibility of the system. To assure that the system is observable, the observability matrix shown below must have full rank.

$$O = \begin{bmatrix} CA \\ CA^2 \\ . \\ . \\ CA^{n-1} \end{bmatrix} \tag{6.34}$$

Where C is the output matrix, A is the system matrix and n is the amount of states.

Besides being limited by the amount of bias states that can be estimated, another problem associated with bias estimation exists. Bias estimation does not ensure convergence of the estimated and measured variables.

Proportional Integral Kalman Filter

The Proportional Integral Kalman Filter (PIKF), originally developed by Kim, Shafai, and Kappos (1989), is a modified version of the Kalman filter that includes an integral term. The integral term improves the robustness of the estimator to external disturbances and ultimately ensures a better estimate.

The PIKF method can be formulated as follows:

$$\begin{bmatrix} x(k+1) \\ d(k+1) \end{bmatrix} = \begin{bmatrix} A & D_i \\ 0 & D_f \end{bmatrix} \begin{bmatrix} x(k) \\ d(k) \end{bmatrix} + \begin{bmatrix} L_p(k) \\ L_I(k) \end{bmatrix} (y(k) - Cx(k)) \tag{6.35}$$

Where $x(k)$ and A are the original state vector and system matrix, $d(k)$ is the added integral states, D_i is the integral gain and D_f is the fading coefficient. $L_p(k)$ and $L_I(k)$ are the proportional and integral Kalman filter gains respectively.

Research done by Linder and Shafai (1997), explore the proportional (L_p) and integral (L_I) gain calculation of the PIKF and propose methods to obtain optimal gains as well as to increase the robustness of the filter. The constant matrices D_I and D_f are designed prior to

operation and determine the performance criteria of the filter. The selection of these parameters are discussed in the sources mentioned earlier and summarized below:

- D_I determines the extent of the effect of the integral term on the estimate and should be of full rank to ensure observability of the overall system
- A larger D_I results in smaller estimation error, but increases the overshoot problem inherent to the PI filter at startup.
- $D_f = \alpha \boldsymbol{I}$ is the fading constant, $0 < \alpha \leq 1$. The fading constant determines to what extent old measurements are ignored. The smaller D_f the less influence the older measurements have on the current estimated state.

It has been shown that by including the fading coefficient D_f, the filter is made more robust by increasing the stability margin of the filter while rejecting transitory disturbances with unknown distribution matrices.

One drawback of using the PIKF or any Kalman filter based estimator, is that measurement noise matrix R_K and the process noise matrix Q_K of the system needs to be known. Though the measurement noise characteristics can easily be determined from the measurement instrumentation, the process noise is not as easy to determine. In most cases, the process noise is not known and is thus assumed. This results in an sub-optimal estimator as the pole placements of the estimator is effected by the choice of Q_K.

e. Estimator Comparison through Simulation

To compare the effectiveness of the estimators described in the previous section, the estimators were tested on a linearized model of the Modular UAV aircraft. The estimators were tested to see their ability to handle:

1. Added sensor biases (AoA and pitch rate biases and accelerometer)
2. Added Noise
3. Errors in the aerodynamic model

Several variants of the estimators were also tested, these included:

1. AoA estimator with measurements Q, C_w
2. AoA estimator with bias estimation and measurements Q, C_w
3. AoA estimator with measurements Q, C_w and α
4. AoA estimator with bias estimation and measurements Q, C_w and α
5. PIKF filter (here the integral term was manually chosen)

The Simulink model used to simulate the effectiveness of the estimators is shown on the page to follow, followed by some of the simulation results obtained:

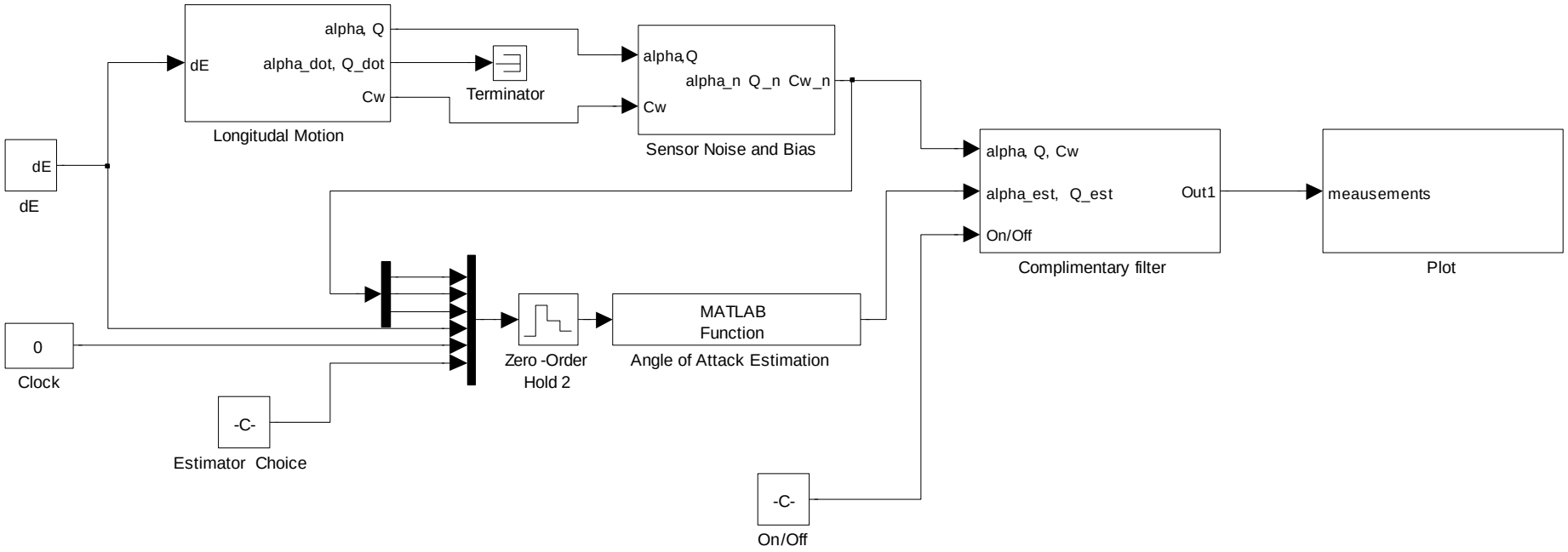

Figure 30: AoA estimator Simulink Simulation

Results

In this section, not all the results obtained from the comparison study is shown. Only those cases that illustrate the downfall or superiority of the different methods are shown.

Test Case 1: simulation with added pitch rate measurement bias added

In this test case, a measurement bias was added to the pitch rate measurement. The estimators that are tested are the estimators 3, 4 and estimator 5. Where the tuning parameters for estimator 5 was chosen to be:

1. $D_i = -q * S * C_{L_a}/(m * V_a)$
2. $D_f = 0.01$
3. $Q_c = 0.1$

The results of this analysis are shown below:

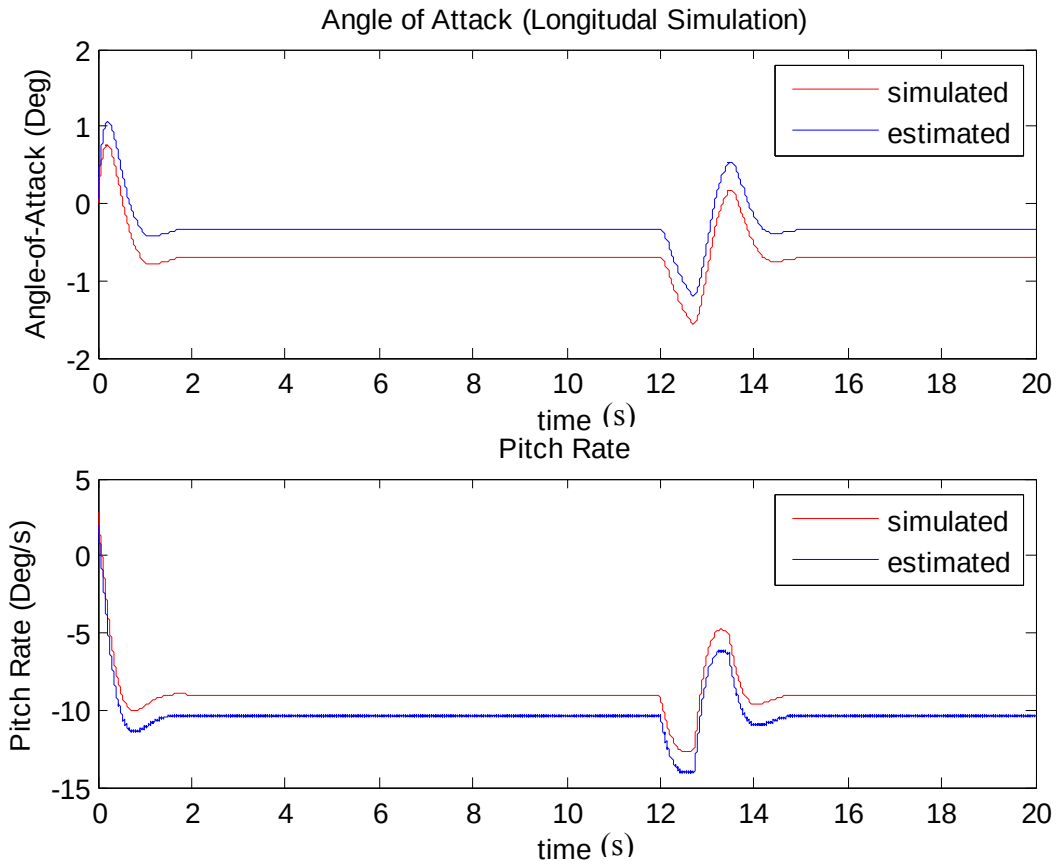

Figure 31: AoA estimator with pitch rate bias

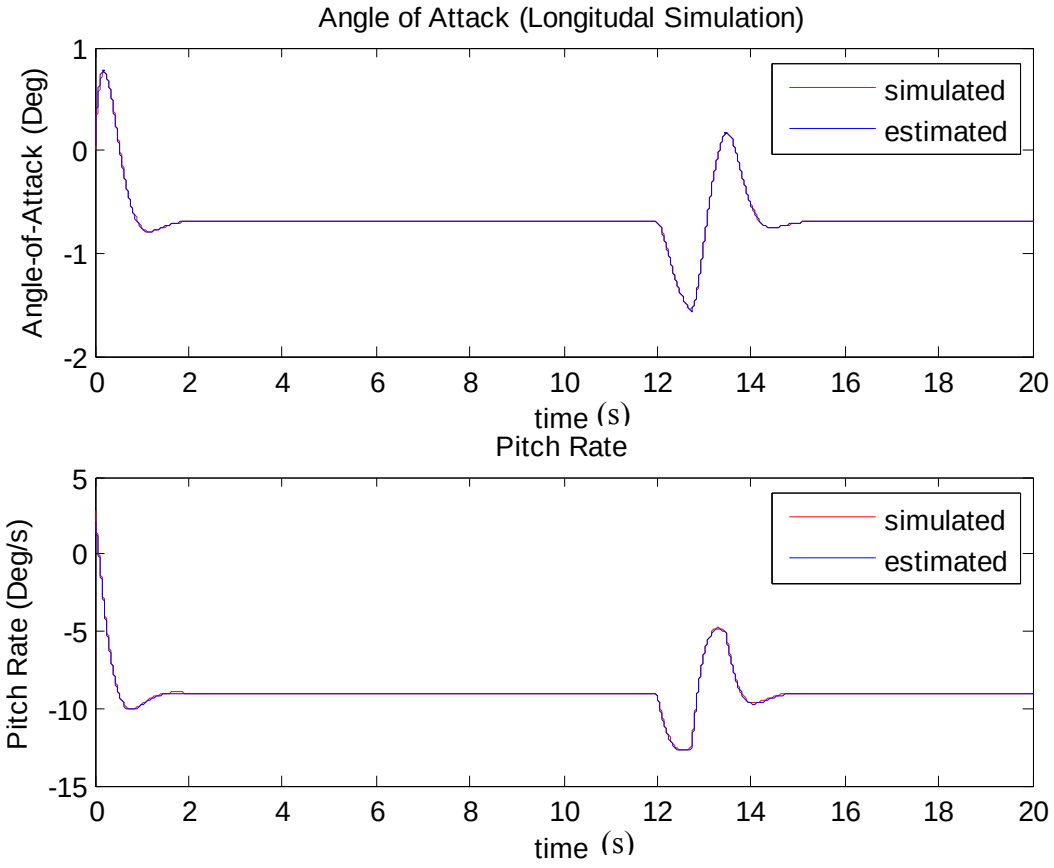

Figure 32: AoAEstimtor with bias estimation and pitch rate bias added

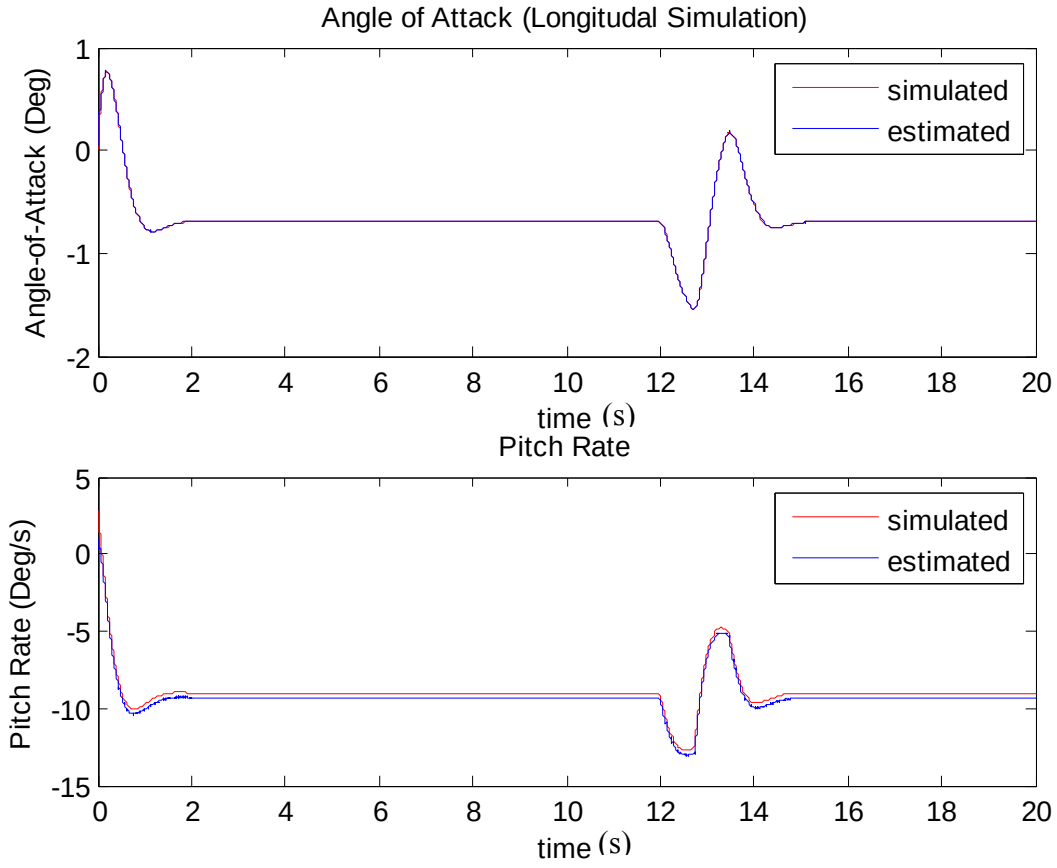

Figure 33: AoA estimation using PIKF and added pitch rate bias

From the first case, it can be seen that without bias estimation, the simple implementation (without bias estimation) yields poor results. Bias estimation (in this case, including the pitch rate bias as an extra term in the estimator) yields good results.

For the case of the PIKF filter, it can be seen that the AoA estimate is a good one. There is however discrepancies with the estimate of the pitch rate. In the setup of the PIKF estimator no bias states were added to the estimator model and the integral term was only implemented on the AoA estimate. This was done to illustrate that though the estimated pitch rate as determined by the filter is incorrect and includes a bias error , which would normally result in incorrect AoA estimates (as illustrated in Figure 31), the integral term of the filter ensures that AoA estimate and the AoA measurement converges.

Test Case 2: simulation with added parameter error

In this test case the effect of errors in the parameters on the estimated AoA are shown. For this case a 10 % error in C_{L_α} was simulated.

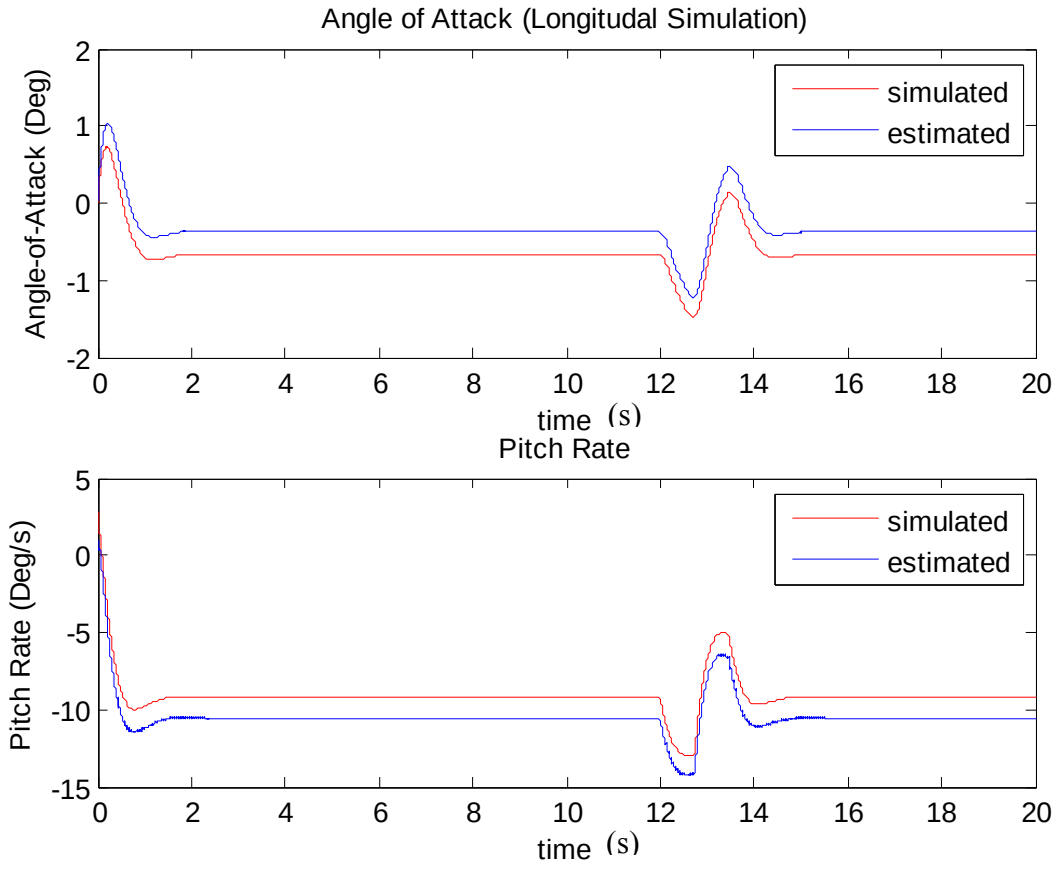

Figure 34: AoA estimator with CLa error

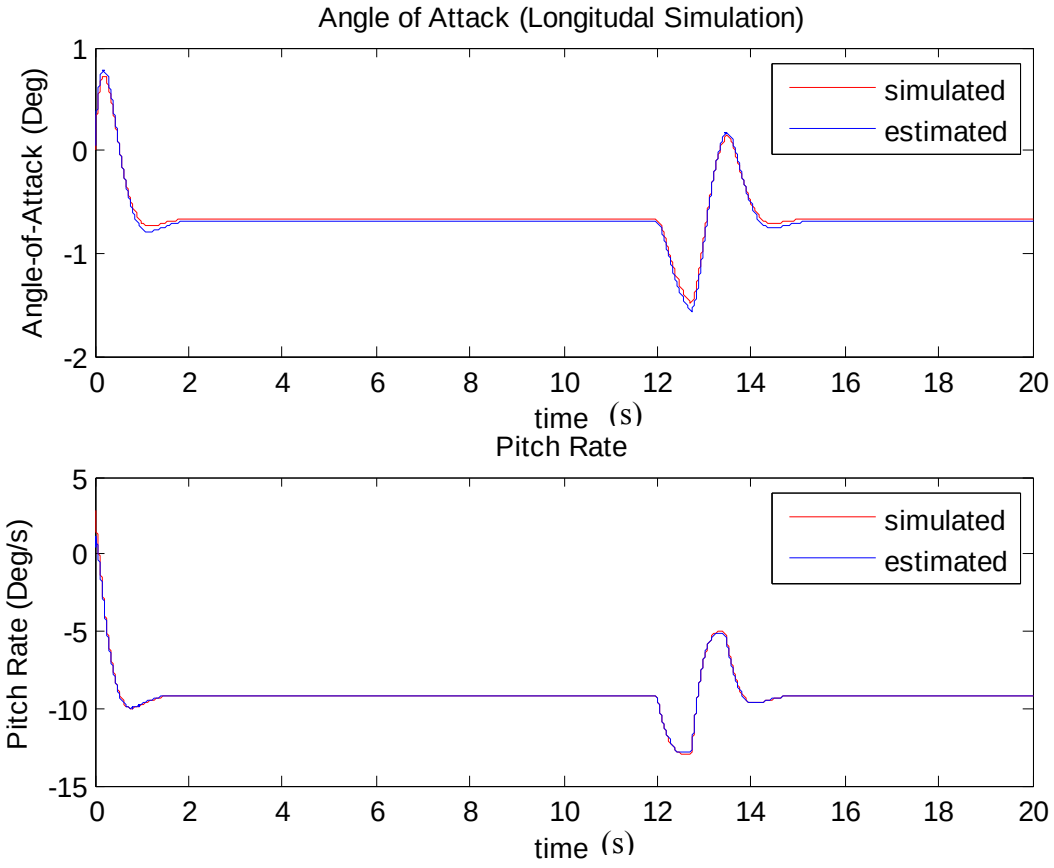

Figure 35: AoA Estimtor with bias estimation and pitch rate bias added

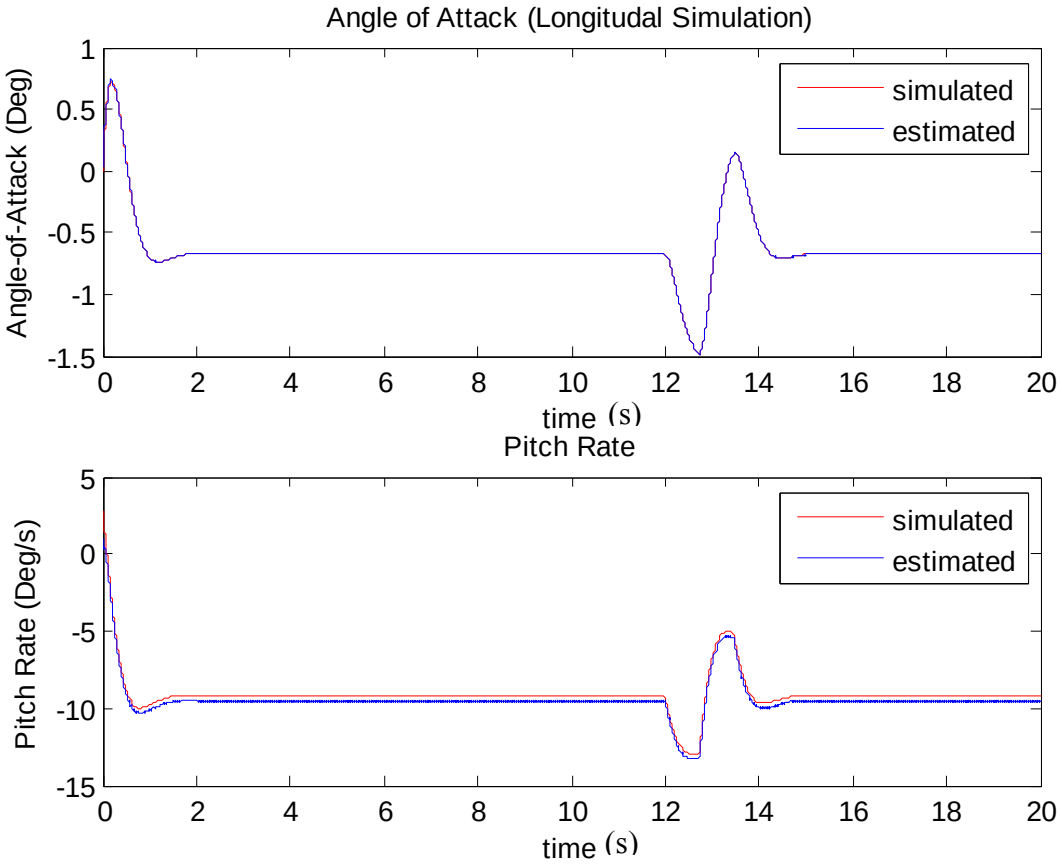

Figure 36: AoA estimation using PIKF withCLa error

In this test case it can be seen that the in the case of parameter errors, the AoA estimator implementing bias error correction starts to fail. The PIKF filter on the other hand, still successfully estimates the AoA and thus shows its superiority to the normal Kalman filter implementation.

f. Problems associated with the Aerodynamic Based Estimator

Besides the problem that the aerodynamic parameters used in the estimator are approximated and thus not exact, the implementation of the aerodynamic based estimator in a FTC framework introduces more problems.

In a FTC framework, during a fault or during parameter estimation, the aerodynamic parameters could be, to a large extent, different to the parameters in the estimator. In this case the AoA estimated by the Aerodynamic Based Estimator will be different to the actual AoA.

This erroneous AoA will then be fed into the SID algorithms which will in turn produce erroneous parameters. It can be shown, however, that over time the aircraft parameters will converge to the actual aircraft parameters and AoA estimates to actual AoA experienced by the aircraft. This is assured, in the case that an estimator augmented with an AoA sensor is used (such as in the case of the PIKF).

Another method to overcome the problem presented is by implementing the estimator in such a way that in the presence of a fault, the estimator only regards measurements obtained from the sensor. At the point when the aircraft parameters converge in the SID algorithm, the AoA estimator starts to regard the estimated AoA again.

6.3.2 The Kinematic Based Estimator

The kinematic method of estimating the AoA was discussed in Section 4.3.2. According to Jategaonkar (1996), FPR was initially used in dynamic flight testing to eliminate the need for direct measurement of angle of attack.

6.3.3 Estimator Choice

The kinematic based estimator is the preferred choice of estimator. The reasons for this choice are:

1. The kinematic based estimator is based on an exact model, whereas the aerodynamic model uses approximations. These approximations make the aerodynamic method susceptible to errors.
2. The kinematic based estimator is easier to implement as no Kalman filter gains have to be calculated.
3. The aerodynamic model is based on the aerodynamic stability and control derivatives which in this thesis are susceptible to change. In the presence of a fault, the parameters that make up the estimator model will be different from the actual parameters of the aircraft. In this case, the AoA estimate will yield an incorrect reading of the AoA, this in turn will be fed through to the SID algorithms which will determine the new, but incorrect, aircraft parameters as it will be based on an incorrect AoA estimate. This situation is not ideal. The kinematic model, however, does not suffer from this problem.

Chapter 7

Angular Acceleration Determination

In order for the aerodynamic coefficients of Equation 4.6 to be determined, it is necessary to determine the angular accelerations $\dot{P}$, $\dot{Q}$ and $\dot{R}$. Two methods for obtaining these accelerations are discussed in this section.

7.1 Numerical Differentiation

The most common method for obtaining the angular accelerations $\dot{P}$, $\dot{Q}$ and $\dot{R}$, is by differentiation the gyroscope measurements (P, Q, R). As the gyroscope measurements are noisy signals, numerical differentiation of these signals produce noisy angular acceleration estimates. Because the noise of noisy signals gets amplified when the signal gets differentiated, the signal-to-noise ratio of these estimated angular accelerations are usually bad. To overcome this problem, the measured angular rates are either filtered before they are differentiated, or they are filtered in the differentiation technique chosen. This section presents some of the differentiation techniques that can be used to obtain the angular accelerations.

7.1.1 Central Difference formulation

One of the most common methods of differentiating a function is through the central difference or finite difference method. This method computes the numerical derivative of a function $f(x)$ by approximating the function as a polynomial $P(x)$ around the point of interest x_0. This is done through interpolation. The derivative of the function is then approximated as the derivative of the polynomial at that point i.e.

$$f'(x_0) \approx P_m'(x_0) \tag{7.1}$$

The order of the polynomial used, m, is chosen to be one less than the amount of sampled points. Fitting a polynomial to 3 sampled points is illustrated below.

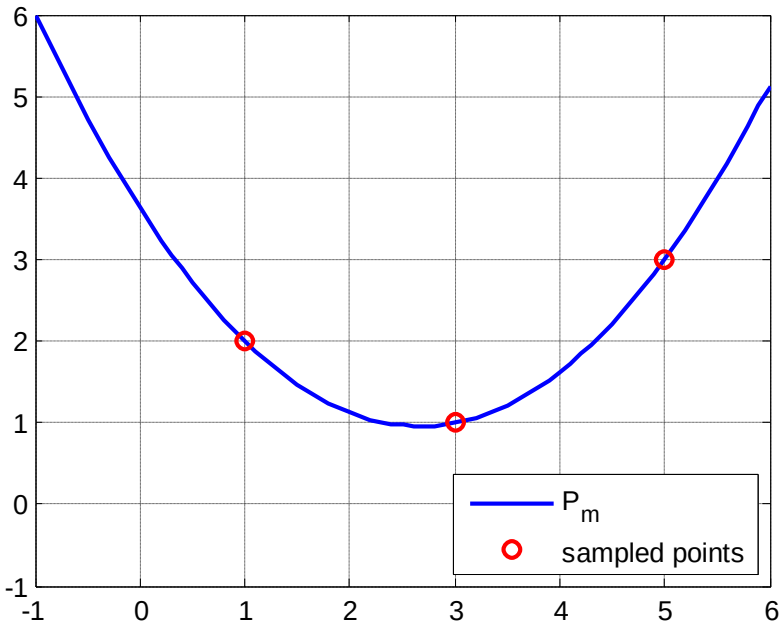

Figure 37: Fitting a polynomial to 3 points

It can be shown that the derivative of the function aboutx_0, given N equidistant samples around x_0 can be determined as follows [41]:

N	**Formulation of the Derivative**$f'(x_0)$
3	$\frac{f(x_0+h)-f(x_0-h)}{2h}$
5	$\frac{f(x_0-2h)-8f(x_0-h)+8f(x_0+h)-f(x_0+2h)}{12h}$
7	$\frac{-f(x_0-3h)+9f(x_0-2h)-45f(x_0-h)+45f(x_0+h)-9f(x_0+2h)+f(x_0+3h)}{60h}$

Though easy to implement, the central difference method is not well suited for use in a noisy environment. This is attributed to the fact that the method approaches an ideal differentiator as the number of samples increases [41], and an ideal differentiator has the characteristic of amplifying noise.

7.1.2 Smoothed Differentiators

The main difference between smoothed differentiators such as the Savitzky-Golay digital filters and the central difference method is in the method of determining the polynomial that

fits the sampled data. In the central difference method, the polynomial was derived through interpolation of the sampled points, in the Savitzky-Golay filters however, the polynomial is approximated by using least-squares approximations [2,41,42]. This is done by minimizing the cost function,

$$Z = \sum_{k=\frac{N-1}{2}}^{\frac{N-1}{2}} [f(x_0 + kh) - P_M(x_0 + kh)]^2 \tag{7.2}$$

where, N is the number of sampled points, $f(x)$ the function sampled and $P_M(x)$ the polynomial, of order M, used to fit the points. The power of the polynomial, M, should be less than (N-1) otherwise the least-squares algorithm is equal to central difference method.

Once the polynomial is estimated, the derivative of the function can be determined

$$f'(x^*) \approx P_m'(x^*) \tag{7.3}$$

The derivation of the Savitzky-Golay filter with polynomial of order 2 and using 5 sampled points is shown in Hough (2010). This method can be easily be expanded to include higher order polynomials with more sampled points. The formulae for determining the derivative of a function, using polynomials of order 2, are tabulated below for different amounts of sampled points [41].

N	**Formulation of the Derivative $f'(x_0)$, (M=2)**
5	$\frac{f(x_0+h) - f(x_0-h) + 2[f(x_0+2h) - f(x_0-2h)]}{10h}$
7	$\frac{f(x_0+h) - f(x-h) + 2[f(x_0+2h) - f(x_0-2h)] + 3[f(x_0+3h) - f(x_0-3h)]}{28h}$
7	$\frac{f(x_0+h) - f(x_0-h) + 2[f(x_0+2h) - f(x_0-2h)] + 3[f(x_0+3h) - f(x_0-3h)] + 4[f(x_0+4h) - f(x_0-4h)]}{28h}$

Table 3: Savitzky-Golay Filter (M=2)

From the table above, it can be seen that the derivative for the function, using a polynomial of order 2, can be written in the general form [41]:

$$f'(x_0) \approx \sum_{k=1}^{m} \frac{f(x_0 + kh) - f(x_0 - kh)}{m(m+1)(2m+1)}, \qquad m = \frac{N-1}{2} \tag{7.4}$$

Though only derivatives for a second order polynomial fit is shown, the equations for higher order fits can be found in [2, 41, 42].

7.1.3 Other Methods

Though the Savitzky-Golay class of filters do have element of noise suppression, they do not filter out all the high order noise. Considering the magnitude response in the figure below, it can be seen that, for high frequencies, the magnitude does not tend to zero and thus high frequency noise is not fully suppressed. The response resembles a wavy, always non-zero response on high frequencies (Holoborodko, 2012).This property is as a result of the least squares smoothing that this method uses, which is not able to fully suppress noise.

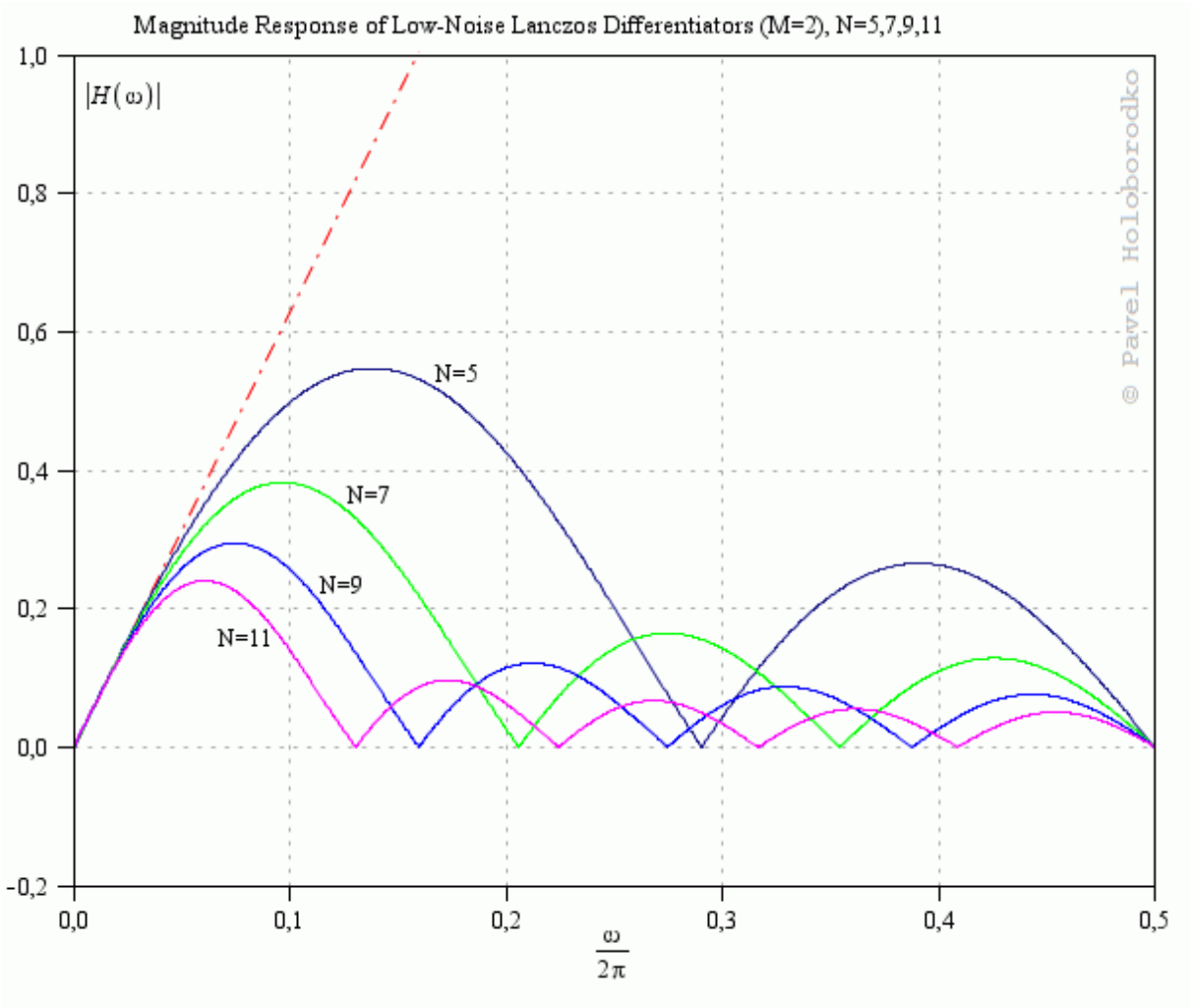

Figure 38: Magnitude response of Savitzky-Golay filters [41]

To ensure the suppression of the higher order noise, better filtering techniques have been proposed. The Smooth Robust Differentiator of [41] has a magnitude response that fades off to zero for higher frequencies. This ensures noise suppression and is more suited for determining the angular accelerations. The magnitude response is shown below:

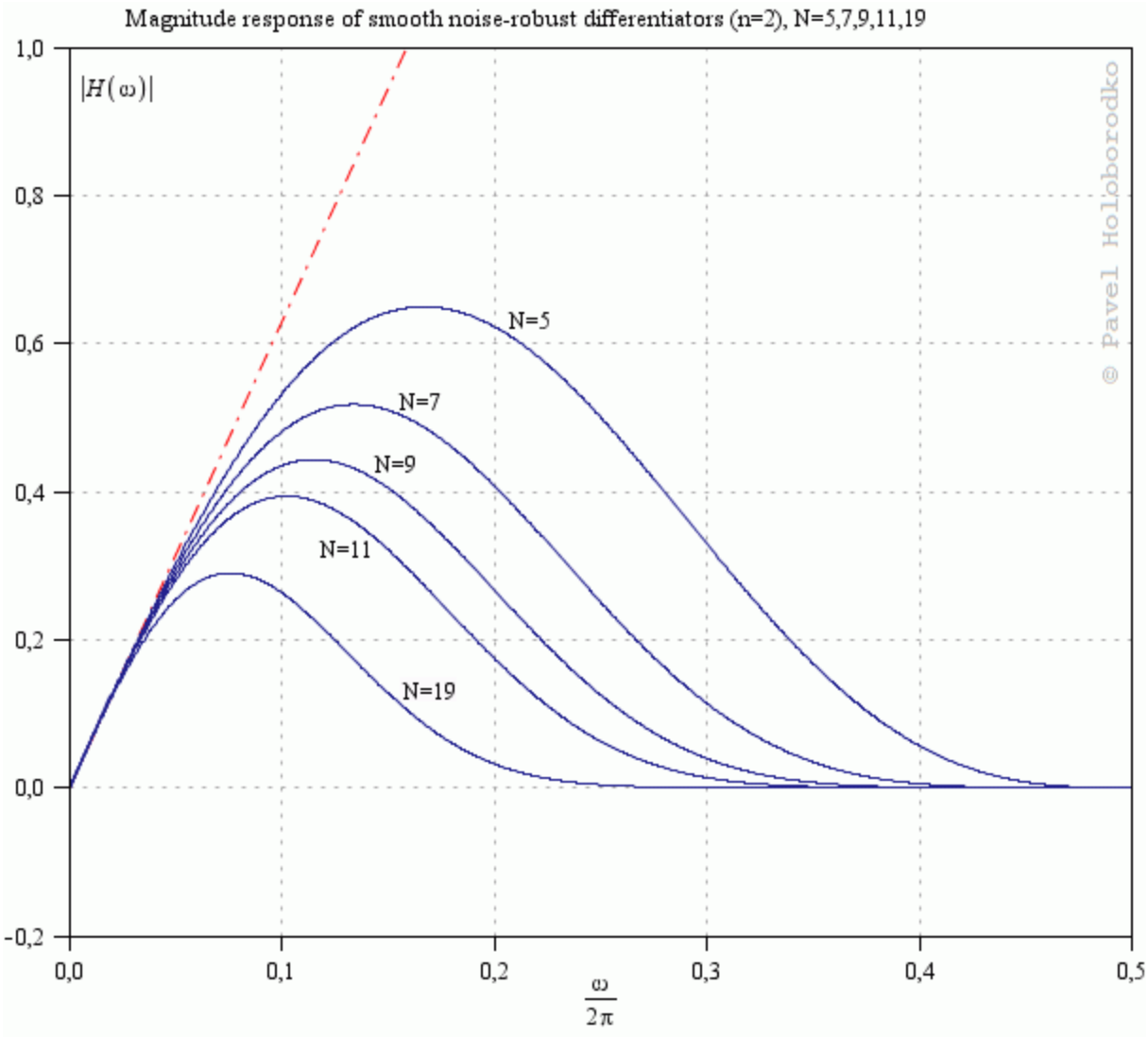

Figure 39: Magnitude response of Smooth Robust differentiators [41]

Another technique commonly used to determine the derivative of a noisy signal is through a two stage process. The first stage being a filtering stage, in which the signal is passed through a low-pass filter. The second stage is then the differentiation stage, in which techniques such as central differences or Savitzky-Golay type techniques are used. This two stage type approach has used in Jategoankar (1996) for determining the angular accelerations. In this approach, a 4^{th} order low pass, symmetrical digital filter was used for the first stage (uses the function smoothMulTS.m). The filter uses 15 points, with the first 3 and the last 3 points not being filtered. The second stage of the approach uses an 8^{th} order differentiator (uses the

Matlab function ndiff_Filter08.m). This figure below shows this method being applied to a noisy signal:

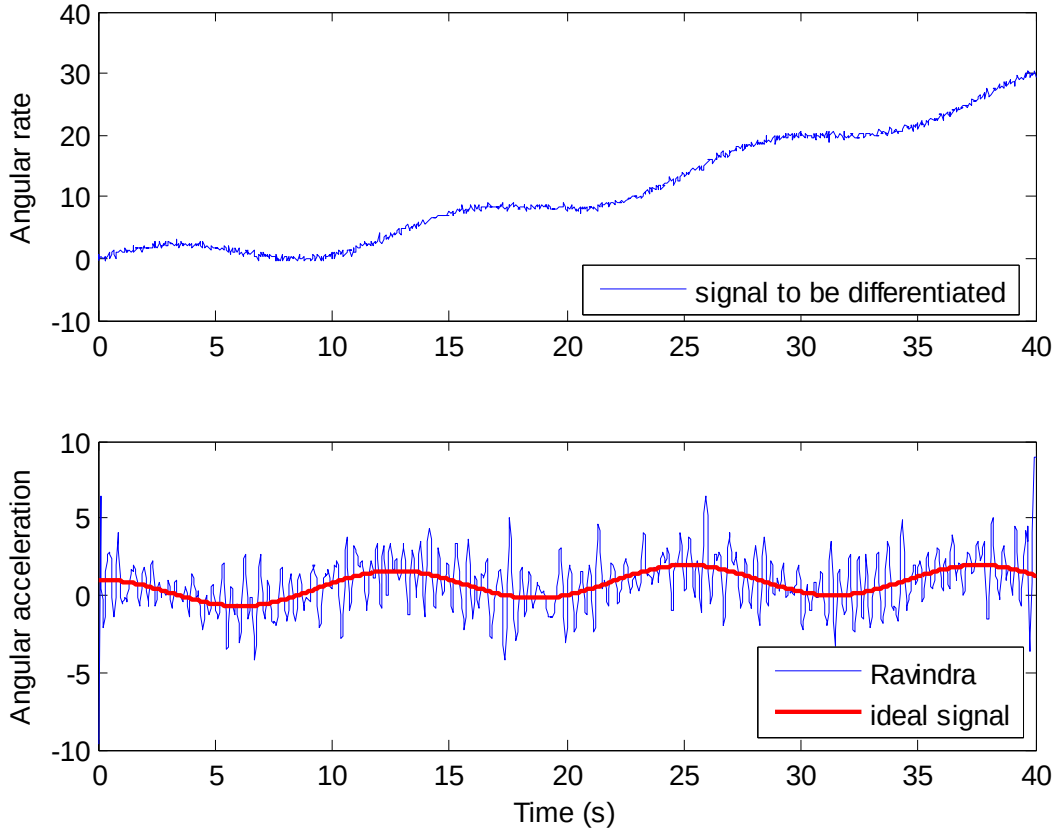

7.1.4 Practical Problems

There are two main problems associated with differentiating a noisy signal. The first being the manner in which the higher frequency noise is handled and then the second being the lag or time delays introduced when implementing the different algorithms.

The first problem, the problem of noise, can be solved by means of high order filters or by using a differencing scheme such as the Smooth Robust Differentiator of [41]. This however introduces time delays (the second problem). These time delays are introduced because future measurements are required, but practically one would have to wait to obtain these measurements and then only determine the derivative for a point in time that has already lapsed. The greater the order of the filter, the greater the time delay that gets introduced.

7.2 Distributed Sensors

In light of the disadvantages of using numerical differentiation for the determination of the angular accelerations, a new method for obtaining these measurements is proposed. By making use of distributed accelerometers, the angular accelerations can be determined. This method is illustrated below:

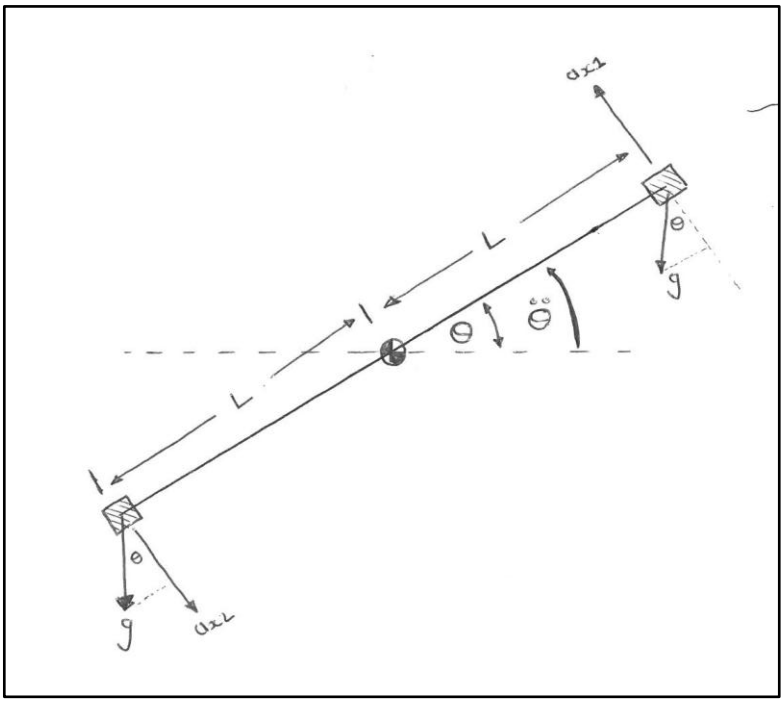

Figure 40: Illustration of distributed sensoring

By placing the accelerometers (a_{x1} and a_{x2}) equidistant away from the center of gravity, the angular accelerations as measured by the accelerometers can be expressed as (refer to the figure above):

$$a_{x1} = \ddot{\theta}L - g\cos\theta \tag{7.5}$$

$$a_{x2} = \ddot{\theta}L + g\cos\theta \tag{7.6}$$

By adding the two accelerometer measurements, the measurements can be made independent of the gravitational effects,

$$a_{x1} + a_{x2} = 2\alpha L \tag{7.7}$$

It can be shown that the angular acceleration can be determined from the two accelerometer measurements as:

$$\ddot{\theta} = \frac{a_{x1} + a_{x2}}{2L} \tag{7.8}$$

As can be seen from the previous equation, the angular acceleration can be determined through the averaging of the two accelerometers. Averaging two signals that are corrupted by white noise has the benefit of reducing the noise. This technique thus produces a more accurate angular acceleration measurement than that of differentiating a gyroscope measurement and it does not introduce time delays as is the case with numerical differentiating.

The concept of distributed sensing was tested by making use of a Simulink model. In the simulation the following assumptions were made:

1. The length L = 0.5
2. The accelerometers have zero bias, corrupted with white noise of $0.1\ m/s^2$ RMS
3. The gyroscope measurements have zero bias, corrupted by white noise of $0.11\ deg/s$ RMS
4. Gravity is taken as 9.81

The following Simulink model was derived to validate this concept:

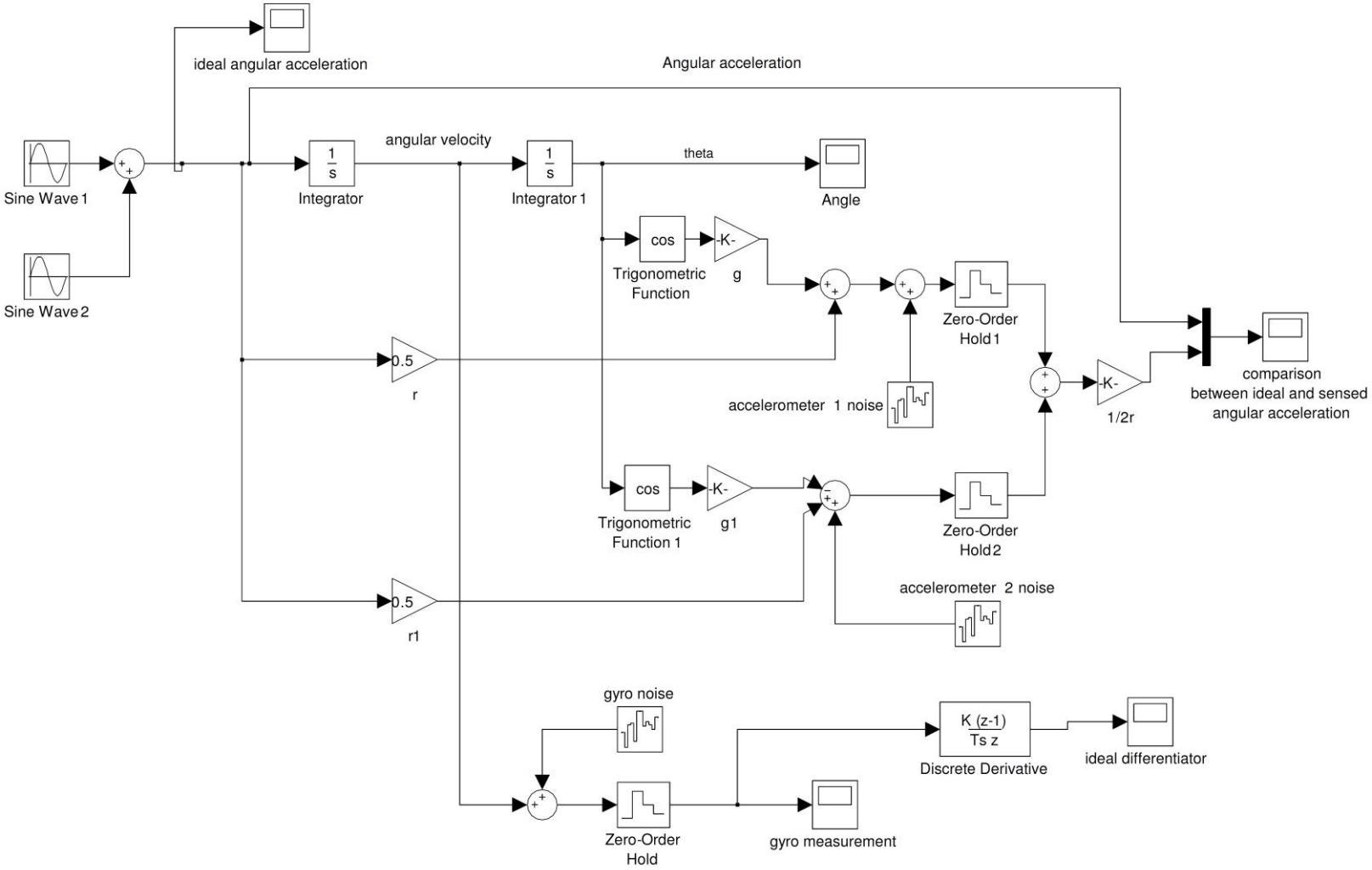

Figure 41: Simulink Model for distributed sensing

The angular acceleration produced through distributed sensing is compared to that of the angular acceleration (measured in degrees per second) produced through numerical differentiation, is shown below:

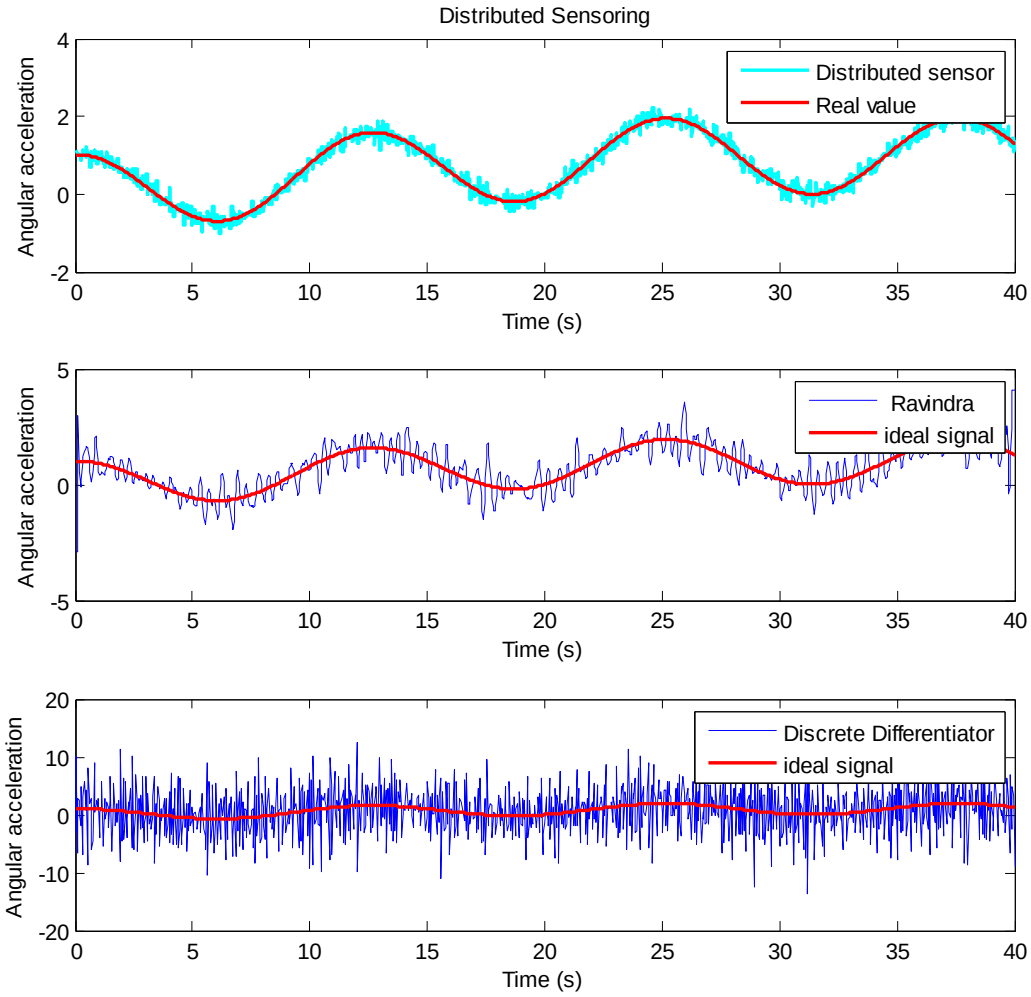

Figure 42: Comparison of distributed sensors and numerical differentiation

As can be seen from the figure above, the noise produced by the distributed sensor technique is lower than that of the numerical differentiation methods. In the case of the discrete differentiator, the signal to noise ratio is so low that it will cause problems during parameter estimation. As mentioned, the noise on the angular accelerations as determined from the distributed sensor technique is directly related to the noise of the sensor themselves. Thus the better the accelerometers used, the less the noise on the estimated angular accelerations.

Chapter 8

System Identification Simulation Results

This chapter covers the application of SID on the non-linear aircraft model developed at the University of Stellenbosch. The main focus of this chapter is to validate the whole SID approach as discussed in the previous chapters. The section thus follows the following order:

1. Obtain Prior Parameter Estimates
2. Determine Control commands (Chapter 5)
3. Obtain measurement data
4. Perform Data Consistency Checks (Chapter 4)
5. Estimate Angular Accelerations (Chapter 7)
6. Estimate measurement biases and characterize noise (Chapter 4)
7. Estimate the AoA (Chapter 6)
8. Implement SID algorithms (Chapter 4) and perform Data Collinearity Checks (Chapter 5)

This chapter pays particular attention to the estimation of the parameters that form part of the short period mode. The reasons behind this are twofold:

1. The same approach is taken to estimate the parameters that form part of the other aircraft modes
2. The aircraft used for testing is not equipped with an AoS (angle of sideslip) sensor, and thus the aircraft is not geared to estimate some of the parameters linked to the lateral dynamics of the aircraft.

8.1 Non-Linear Simulation: Short Period Mode

This section presents the simulation results of system identification applied to the Modular UAV aircraft. For the analysis presented in this section, a control system is implemented to keep the aircraft in a straight and level flight condition with an airspeed of 20 m/s. For the

simulation, it is also assumed that the air density $\rho = 1.0588\,\mathrm{kg/m^3}$ (the air density in Pretoria).

8.1.1 Aircraft parameters

The stability and control derivatives as well as the mass properties of the Modular UAV aircraft have been supplied by the CSIR and are shown below:

a. Physical Specifications:

Variable	Description	Value	Units
m	Aircraft Mass	26.0	kg
b	Wingspan	4.0	m
S	Wing reference area	1.44	$\mathrm{m^2}$
e	Oswald factor (Wing efficiency factor)	0.85	-
A	Wing aspect ratio	11.1	-
c	Mean aerodynamic chord	0.36	m
I_{xx}	Moment of inertia	16.53436	$\mathrm{kg.\,m^2}$
I_{yy}	Moment of inertia	11.58287	$\mathrm{kg.\,m^2}$
I_{zz}	Moment of inertia	13.67185	$\mathrm{kg.\,m^2}$

Table 4: Modular UAV Physical Specifications

b. Stability Derivatives

Variable	Value
C_{L_0}	0.5
C_{D_0}	0.06
C_{L_α}	5.557928
C_{L_Q}	9.046991
C_{y_β}	-0.389444
C_{y_P}	0.048295
C_{y_R}	0.244026
C_{m_0}	0
C_{m_α}	-1.069455
C_{m_Q}	-18.442581

C_{l_β}	-0.071508
C_{l_P}	-0.621899
C_{l_R}	0.194571
C_{n_β}	0.102214
C_{n_P}	-0.063578
C_{n_R}	-0.085316

Table 5: Modular UAV Stability Derivatives

c. Control Derivatives

Variable	Value
$C_{L_{\delta_E}}$	0.4104
$C_{m_{\delta_E}}$	-1.4193
$C_{y_{\delta_A}}$	-0.0194
$C_{l_{\delta_A}}$	-0.3254
$C_{n_{\delta_A}}$	0.0080
$C_{y_{\delta_R}}$	0.2138
$C_{m_{\delta_R}}$	0.0056
$C_{n_{\delta_R}}$	-0.0709

Table 6: Modular UAV Control Derivatives

The parameters shown above are used in the simulation environment and also form part of the priori information used for the control inputs used for SID.

8.1.2 Control Inputs

As discussed in Chapter 5, it is necessary to design an input signal that is able to sufficiently excite the dynamics of the aircraft during system identification. These control inputs are not only important when implementing the parameter estimation algorithms, but are also necessary when doing data consistency checks. For this very reason, not only the control inputs needed to excite the short period mode are discussed, but also for the roll and Dutch roll modes respectively.

The control inputs discussed in this section are implemented by superimposing them onto the control input of the control system implemented to keep the aircraft in a straight and level

flight condition. This method of superimposing the signal has been discussed in [4, 8, 9, and 13].

a. Short Period mode

In chapter 5 it was shown that the period of the short period mode can be calculated as follows:

$$\omega_{n\ (short\ period\ )} = \sqrt{-\left(\frac{L_\alpha}{m\bar{V}}\frac{M_Q}{I_{yy}} + \frac{M_\alpha}{I_{yy}}\right)} \tag{8.1}$$

Where

$$L_\alpha = qSC_{L_\alpha} \tag{8.2}$$

$$M_Q = qS\bar{c}\frac{\bar{c}}{2\bar{V}}C_{mQ} \tag{8.3}$$

$$M_\alpha = qS\bar{c}C_{m\alpha} \tag{8.4}$$

Thus given the aircraft physical parameters, the stability and control derivatives, the trim airspeed and the air density, the natural frequency of the short period mode can be calculated to be:

$$\omega_{n\ (short\ period)} = 3.9068\, rad/s \tag{8.5}$$

It is now possible to determine a control input to excite the short period mode. In this text, two different types of inputs are tested, the one being a simple doublet and the other being a 3-2-1-1 multistep input. The period of the excitation signals can thus be determined by the formulae presented in Chapter 5:

3-2-1-1 multistep input:

$$\Delta t_{3211} \approx \frac{1}{3}\ .\text{period of oscilation} = \frac{2\pi}{3\omega_{n\ (short\ period\ )}} = 0.5361 \text{ seconds} \tag{8.6}$$

Doublet input:

$$\Delta t \approx \frac{2\pi}{2\ \omega_{n\ (short\ period\ )}} = 0.8041 \text{ seconds} \tag{8.7}$$

The amplitude of the control inputs should be such that the input does not destabilize the aircraft. It was shown by Hough (2010), that a control input with amplitude of 5 degrees will sufficiently excite the mode without destabilizing the aircraft. Figure 43 shows a doublet and 3-2-1-1 multistep elevator input with an amplitude of 5 degrees and period as determined above.

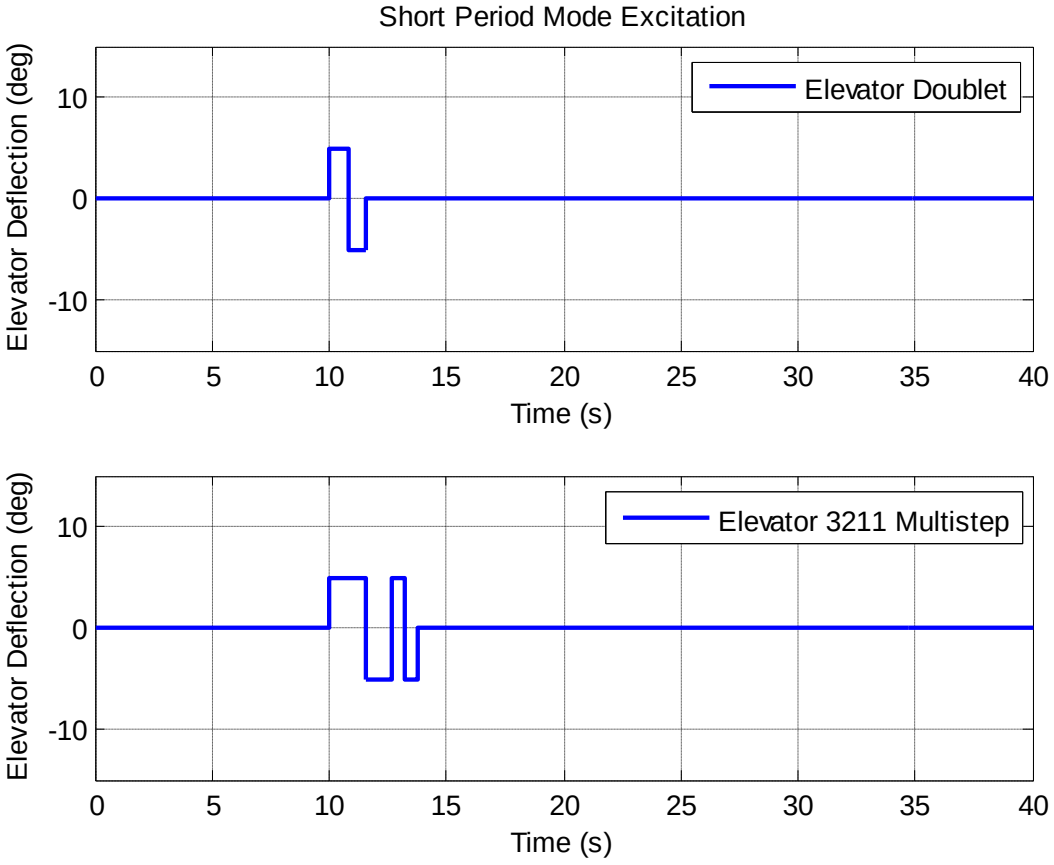

Figure 43: Short Period mode excitation

b. Roll Mode

The period of the roll mode can be determined from Equation 5.27. The resulting period for the Modular UAV aircraft at 20 m/s is thus:

$$\omega_{n\ (roll\ mode\ )} = \sqrt{-\frac{\rho \bar{V} S b^2 C_{l_p}}{4 I_{xx}}} = 2.1419\ rad/s \tag{8.8}$$

As mentioned in Chapter 5, the doublet input is generally used to excite the roll mode. The period of the doublet can thus be determined as:

$$\Delta t \approx \frac{2\pi}{2\ \omega_{n\ (roll\ mode\ )}} = 1.4667 \text{ seconds} \tag{8.9}$$

Using amplitude of 5 degrees, and the period as determined above, the aileron input signal used to excite the roll mode is shown below:

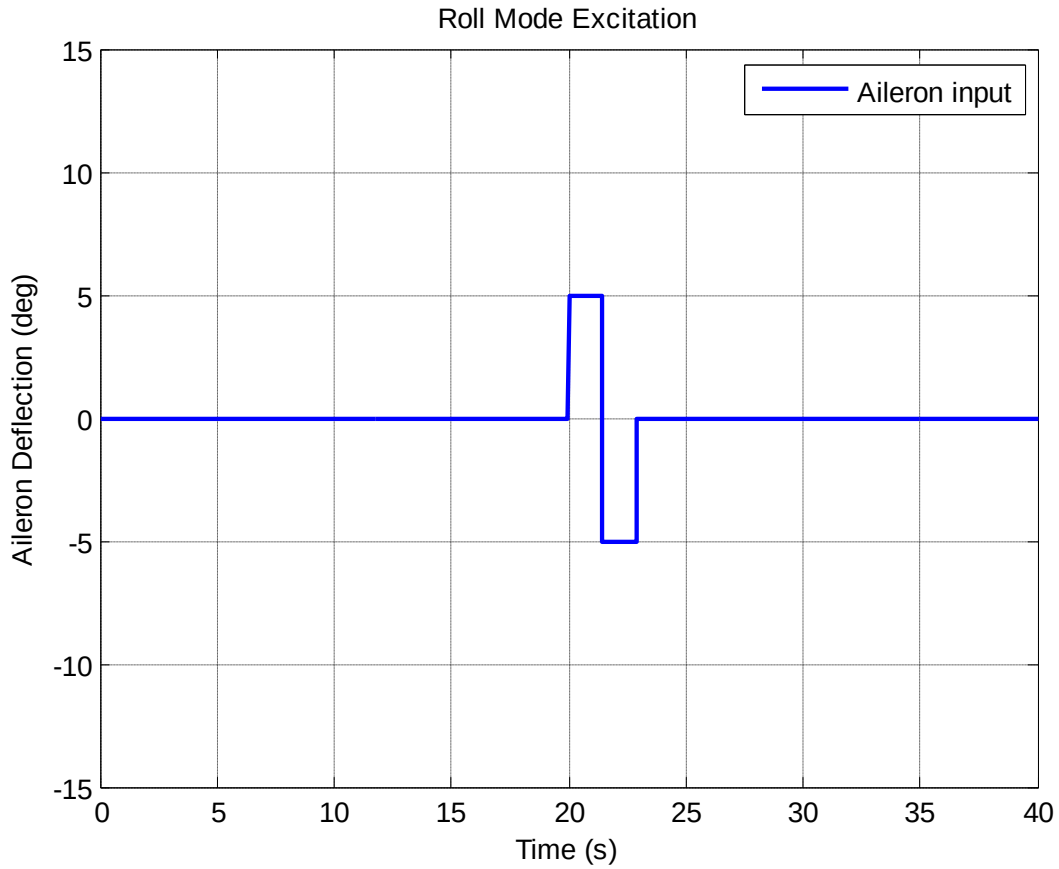

Figure 44: Roll mode excitation

c. Dutch Roll Mode

The Dutch roll mode can be excited by means of a doublet input, the period of which can be determined by:

$$\Delta t \approx \frac{2\pi}{2\,\omega_{n\ (Dutch\ roll\ mode\ )}} \tag{8.10}$$

where,

$$\omega_{n\ (Dutch\ roll\ mode\ )} = \sqrt{\left(\frac{(\rho Sb)^2 C_{y_\beta} C_{n_R}}{8mI_{zz}} + \frac{\rho SbC_{n_\beta}}{2I_{zz}}\right)} = 3.0484\ rad/s \tag{8.11}$$

Thus the period of the doublet is calculated as

$$\Delta t \approx \frac{2\pi}{2\,\omega_{n\ (Dutch\ roll\ mode\ )}} = 1.0306 \text{ seconds} \tag{8.12}$$

Using an input signal of amplitude of 5 degrees, and the period as determined above, the aileron input signal used to excite the Dutch roll mode is shown below:

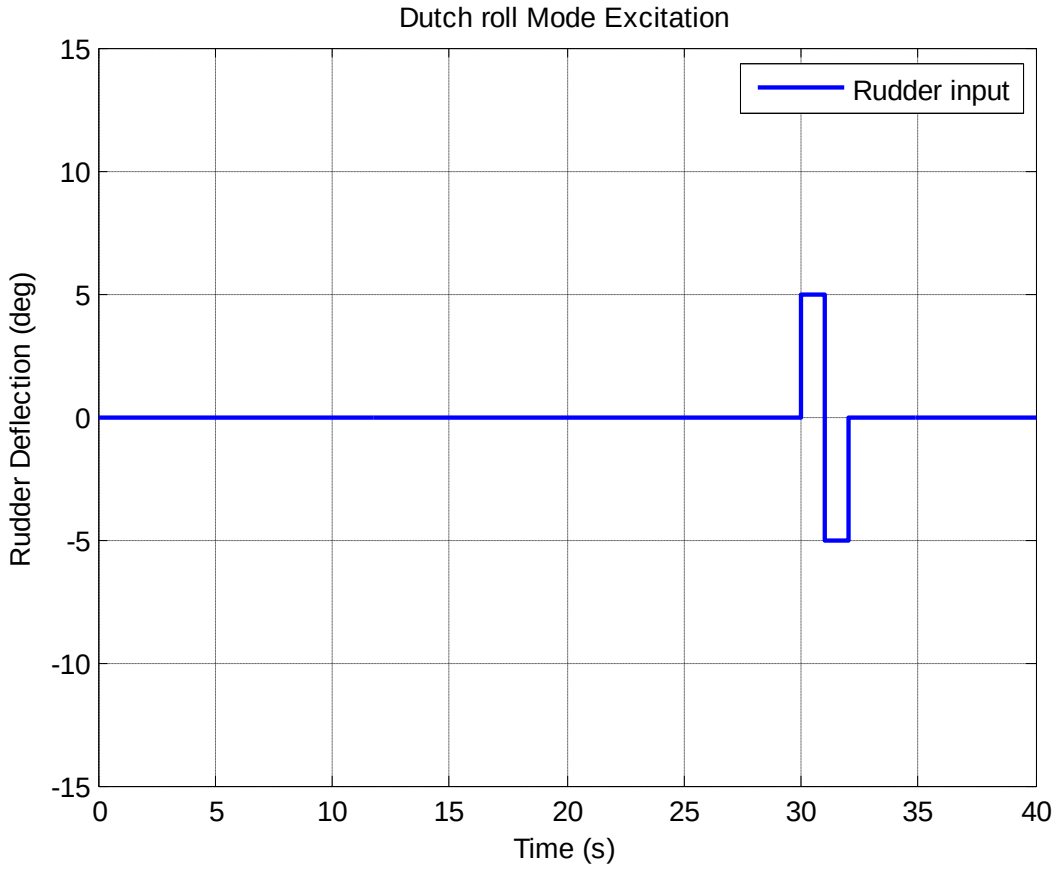

Figure 45: Dutch roll mode excitation

8.1.3 Data Consistency Check

Applying the FPR method as described in Chapter 5, it is possible to detect discrepancies between the measured and estimated variables that are used in the system identification algorithms.

Using the accelerometer and gyroscope measurements as inputs :

$$\mathbf{u} = [a_x \quad a_y \quad a_z \quad P \quad Q \quad R]^T \tag{8.13a}$$

The following states can be estimated using Equations 4.24 to 4.26:

$$\mathbf{x} = [U \quad V \quad W \quad \phi \quad \theta \quad \varphi \quad x_E \quad y_E \quad h_E]^T \tag{8.13b}$$

From which the following output variables can be determined

$$\mathbf{y} = [\bar{V} \quad \alpha \quad \beta \quad \phi \quad \theta \quad \varphi \quad h_E] \tag{8.13c}$$

By comparing these output variables to their measured responses, the effects of biases on the measured inputs (a_x, a_y, a_z, P, Q, R) are made evident. This is shown in the figure below:

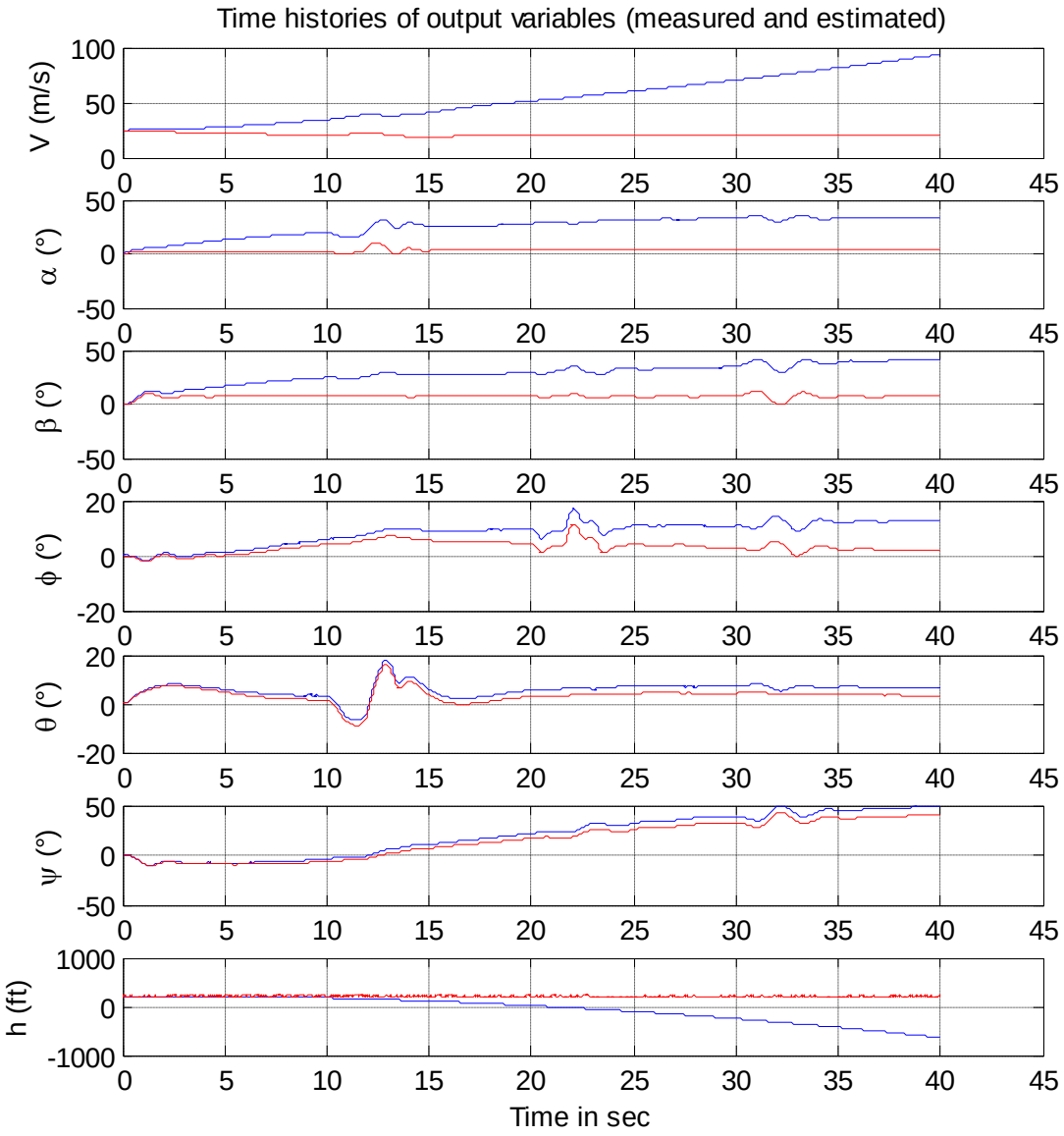

Figure 46: Output of FPR comparison

As can be seen from the previous figure, the discrepancies between the measured variables (indicated in red) and the estimated ones (indicated in blue) are very noticeable. Considering the airspeed measurement $\bar{V}$, it can be seen that the estimated airspeed diverges from the measured airspeed. This divergence is as a result of biases on the input variables. Though these biases on the measured variables may be small, during the propagation of the states, the biases accumulate causing the divergence.

Before parameter estimation can be done, it is necessary to account for the biases on the variables. This is to ensure that the estimated parameters converge to their true values. This is done in the next section.

8.1.4 Bias Estimation

Using the method presented in Section 4.3.3, the biases on the sensors can be determined. The Gauss-Newton optimization method was used to solve the Output-Error method. Two simulations were run, one without the estimation of the AoA and AoS scale factor and bias estimates, and one including these factors. The following results were obtained from the simulation:

a. Without AoA and AoS measurements

Parameter	Estimated Biases	True Biases	Error (%)
Δp	$3.5285\ 10^{-3}$ rad/s	0.0035 rad/s	0.82 %
Δq	$5.12205\ 10^{-3}$ rad/s	0.0035 rad/s	17.7 %
Δr	$3.49017\ 10^{-3}$ rad/s	0.0035 rad/s	0.28 %
Δa_x	1.02592 m/s^2	1 m/s^2	2.6 %
Δa_y	0.94647 m/s^2	1 m/s^2	5.3 %
Δa_z	0.98006 m/s^2	1 m/s^2	1.99 %

Table 7: Estimated Biases excluding AoA and AoS measurements

Including the effects of the biases estimated, the graphs to follow, were obtained using the FPR method:

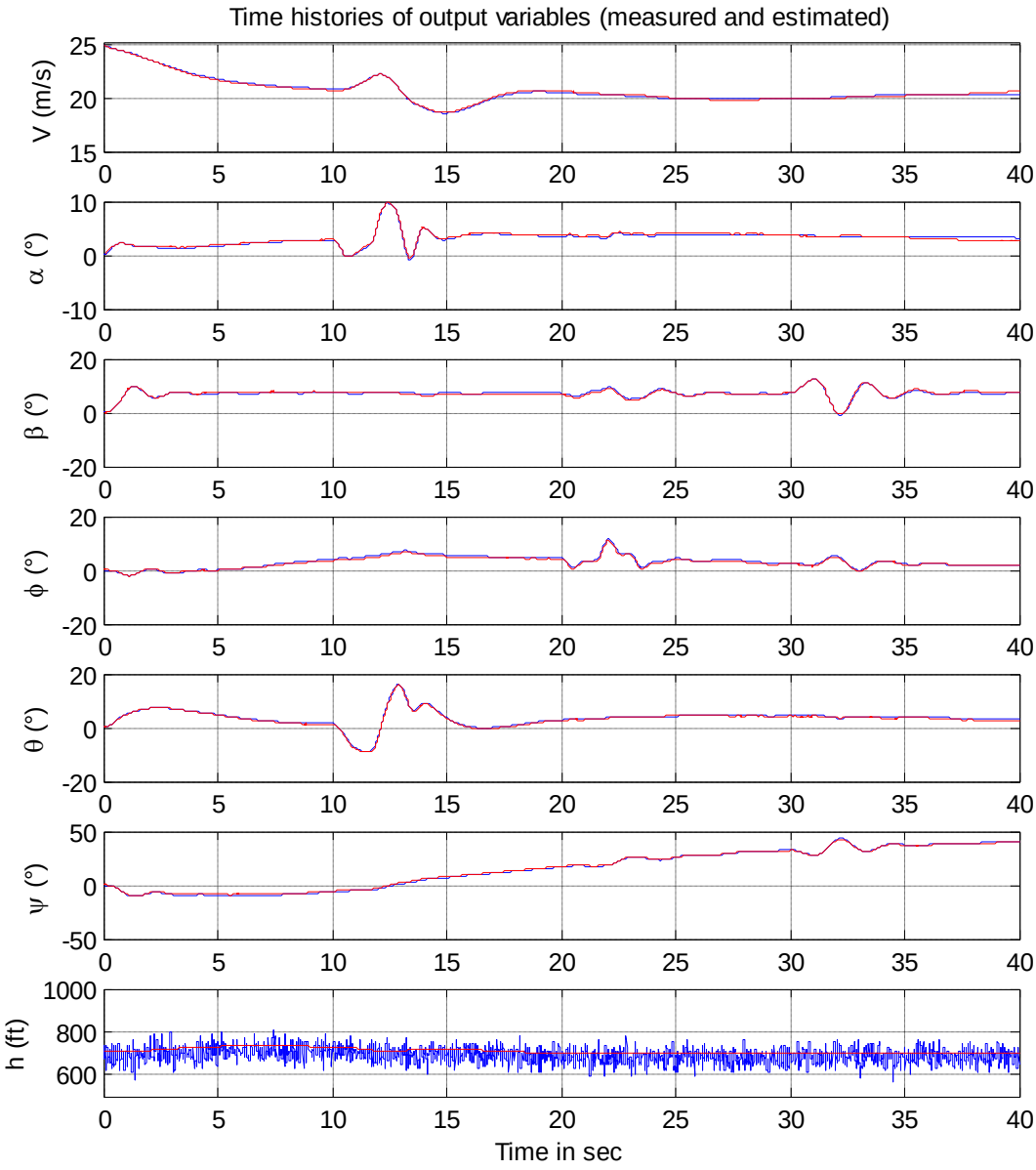

Figure 47: FPR after bias estimation (without AoA and AoS measurements)

From the results above, it can be seen that after the biases were corrected for, the FPR analysis produced results in which all the measurements were kinematically consistent and thus the estimated measurements matched the measured ones.

As can be seen from the errors, there is a considerable error (17%) on the pitch rate bias. The correlation factors give more insight to the source of this error. The table below shows which parameters have a correlation coefficient greater than 0.9:

Variable 1	Variable 2	Correlation coefficient
p	a_y	0.94
q	a_x	0.92

Table 8: Measured variables with correlation greater than 0.9

Here it is evident that the roll rate measurement is has high correlation with the y-accelerometer measurement, showing high dependence. This correlation is more evident in the measured responses plotted below. As can be seen that the responses of the variables in the table above, the measured variables p and a_y as well as $q$and $a_x$resemble scaled versions of each other.

By considering the dynamic equations of the normal force and lateral accelerations on the aircraft, the dependence of the above mentioned variables is evident. According to Peddle (2008), the normal acceleration C_w coordinated in the wind axes, and the lateral acceleration B_w coordinated in the wind axes can be expressed as:

$$C_w = \left[-\frac{qS}{m}C_{L_\alpha} \quad -\frac{qS}{m}\frac{\bar{c}}{2\bar{V}}C_{L_Q}\right]\begin{bmatrix}\alpha \\ Q\end{bmatrix} + \left[-\frac{qS}{m}C_{L_{\delta E}}\right]C_{L_{\delta E}} + \left[-\frac{qS}{m}C_{L_0}\right] \tag{8.14}$$

$$B_w = \left[\frac{qS}{m}C_{y_\beta} \quad \frac{qS}{m}\frac{b}{2V}C_{y_P} \quad \frac{qS}{m}\frac{b}{2V}C_{y_R}\right]\begin{bmatrix}\beta \\ P \\ R\end{bmatrix} + \left[\frac{qS}{m}C_{y_{\delta A}} \quad \frac{qS}{m}C_{y_{\delta R}}\right]\begin{bmatrix}\delta_A \\ \delta_R\end{bmatrix} \tag{8.15}$$

These accelerations C_w and B_w can be related to the accelerometer measurements a_x and a_y respectively, through a DCM transformation (a wind to body axes transformation). From the normal acceleration, it is evident that the pitch-rate response and the normal acceleration are dependent on each other. Of the measured inputs (P, Q, R, a_x, a_y, a_z), the pitch-rate measurement has the greatest influence on the acceleration a_x.

By considering the lateral accelerations, one would expect that the yaw-rate would have a greater relationship with the acceleration a_y, as

$$C_{y_R} > C_{y_P} \tag{8.16}$$

This relationship between the yaw-rate and side acceleration is even evident in the measured responses plotted below. It is thus difficult to ascertain the reason between the high

correlation between the roll-rate and the side acceleration. Factors such as insufficient excitation of the roll mode or insufficient excitation of the Dutch-roll mode could result in high correlation.

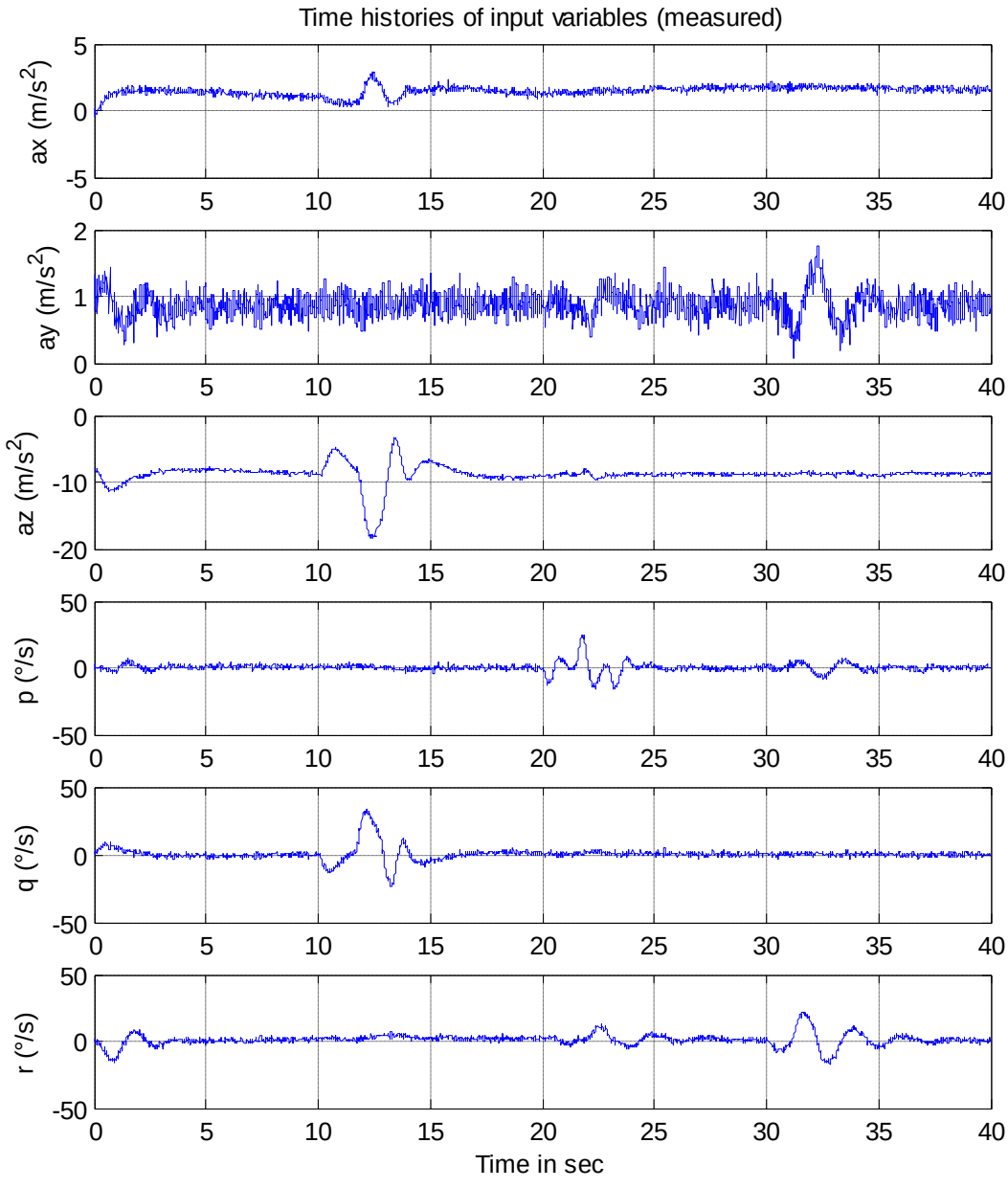

Figure 48: Measured variables for bias estimation

b. With AoA Measurements

The biases and scale factors estimated using the FPR method and the output error method are shown below:

Parameter	Estimated Biases	True Biases	Error (%)
Δp	$3.40689\ 10^{-3}$ rad/s	0.0035 rad/s	2.66 %
Δq	$3.89144\ 10^{-3}$ rad/s	0.0035 rad/s	11.18 %
Δr	$3.51523\ 10^{-3}$ rad/s	0.0035 rad/s	0.44 %
Δa_x	1.02557 m/s^2	1 m/s^2	2.56 %
Δa_y	0.921156 m/s^2	1 m/s^2	7.88 %
Δa_z	0.996628 m/s^2	1 m/s^2	0.34 %
K_α	1.89164	2	5.4%
$\Delta\alpha$	1.7350 deg	2 deg	13.2%

Table 9: Estimated Biases including AoA measurements

With the AoA measurements added, similar trends in the estimated biases are noticed. The maximum error (when considering the accelerometer and gyroscope measurements only) still lies with the yaw rate bias estimate.

With the added scale factor and bias of the AoA measurements added to the parameter vector to be estimated, it can be seen that the scale factor is estimated within 10%, and the AoA bias within 15%. Including the effects of the biases estimated, the following graphs were obtained using the FPR method:

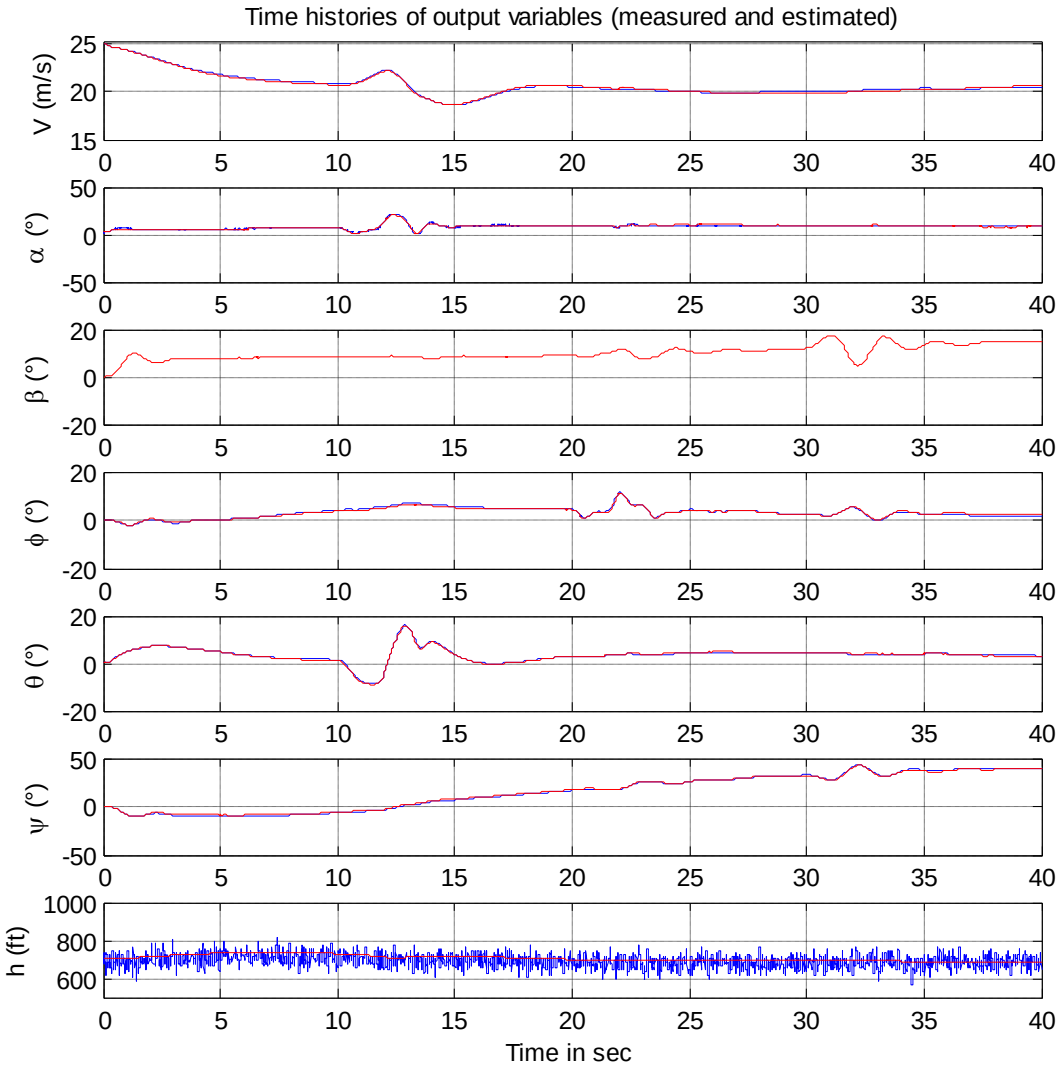

Figure 49: FPR after bias estimation (with AoA measurement)

c. Remarks

From the analysis above, it can be seen that FPR method produces fairly good results, with most of the biases estimated within 10% and all within 15% of their true values. To improve these results the following can be done:

1. Choose sensors with better noise characteristics, and
2. Filter the measurements before estimating the biases.

The FPR method should not replace the normal calibration of sensors, but rather assist in the calibration process. The method is also not well suited for online application, and is generally used as data pre-processing step in offline system identification. The main reason behind this, being the computational time required for a solution to be found. In all the tests performed, using the Output-Error method, the FPR method took more than 10 mins to find a solution on a Core2Duo, 2 GHz machine with 3 GB ram.

For online implantation, the FPR method can be performed prior to the system identification flight test, and the results used as calibration of the sensors for the flight test. In the case where real-time updates of the biases are required, the extended Kalman filter implementation of FPR can be used, [23].

8.1.5 Estimation of Angular Accelerations

Though the concept of distributed sensoring for the determination of the angular accelerations was seen to be a good option, this is not currently implemented on the aircraft at the ESL. The angular accelerations are thus obtained through numerical differentiation.

The gyro measurements are first smoothed by means of a 4^{th} order symmetric filter, after which, the filtered measurements are passed through an 8^{th} order differentiator. This process is described in Jategoankar (1996) and the results are shown below.

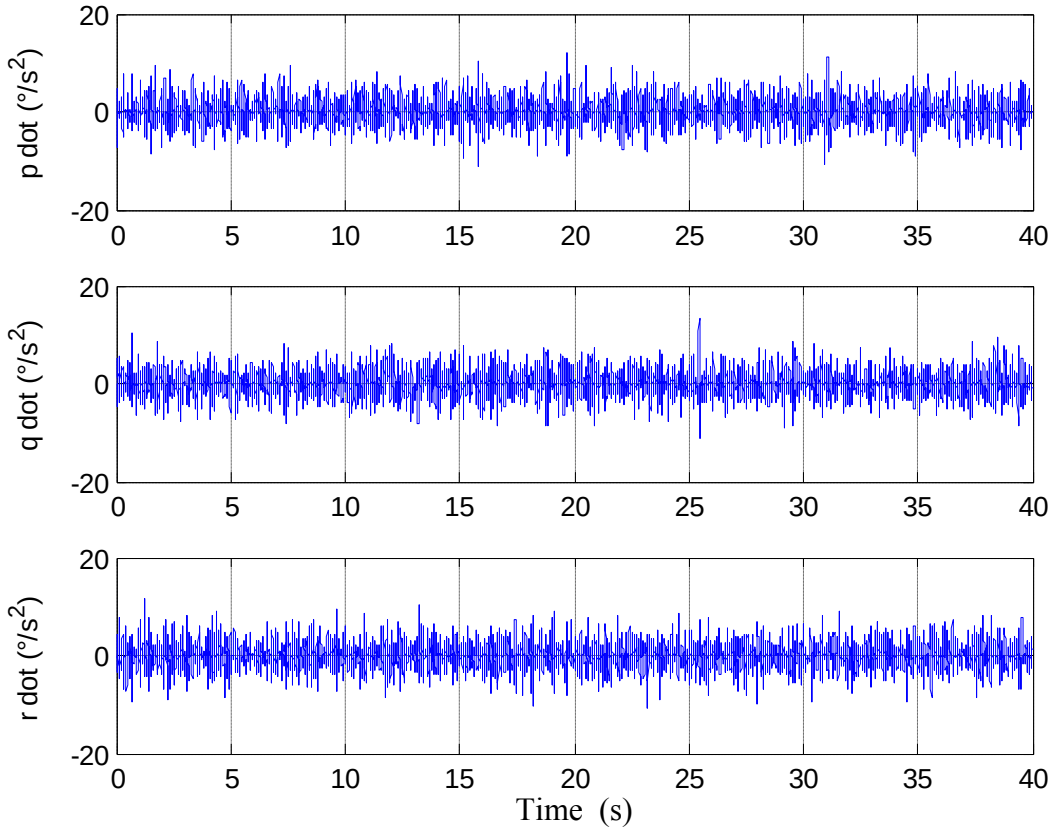

Figure 50: Angular accelerations as determined by ndiff08

Though the method used by Jategoankar was shown in [12] to produce satisfactory results, for the case presented in this thesis, the signal-to-noise ratio of the estimated angular accelerations was too low. There are two methods to overcome this problem:

1. Use better quality gyroscopes that have less noisy signals
2. Increase the order of the smoothing filter
3. Use distributed sensors instead of numerical differentiation

As the gyroscopes used on the aircraft are limited to those available, a higher order filter was used prior to differentiation of the gyroscope signals. By using an 11^{th} order low-pass Butterworth filter prior to differentiation, better estimates of the angular rates were achieved. This is shown in the figure below:

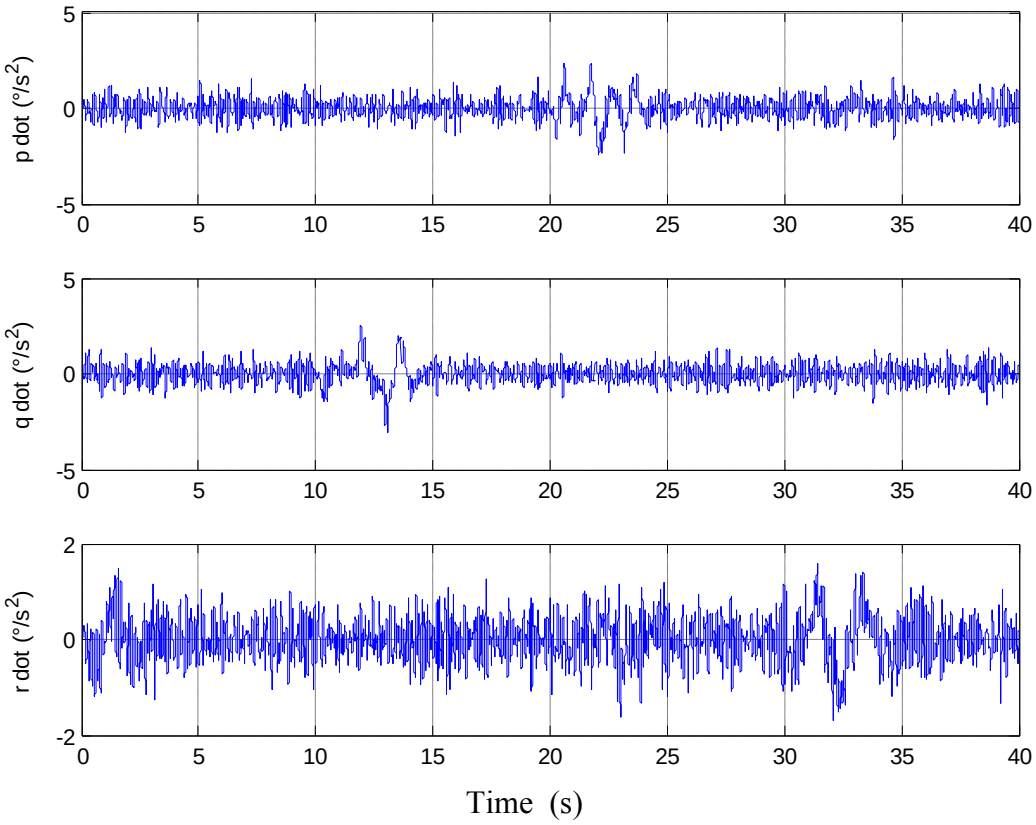

Figure 51: Differentiation with 11th order smoothing filter

A comparison of the estimated and the actual angular accelerations are shown below. This is to indicate the closeness of the estimates to the actual angular accelerations as well as to show the time delay that is introduced into the signal. These time delays have to be accounted for before estimating the aircraft parameters.

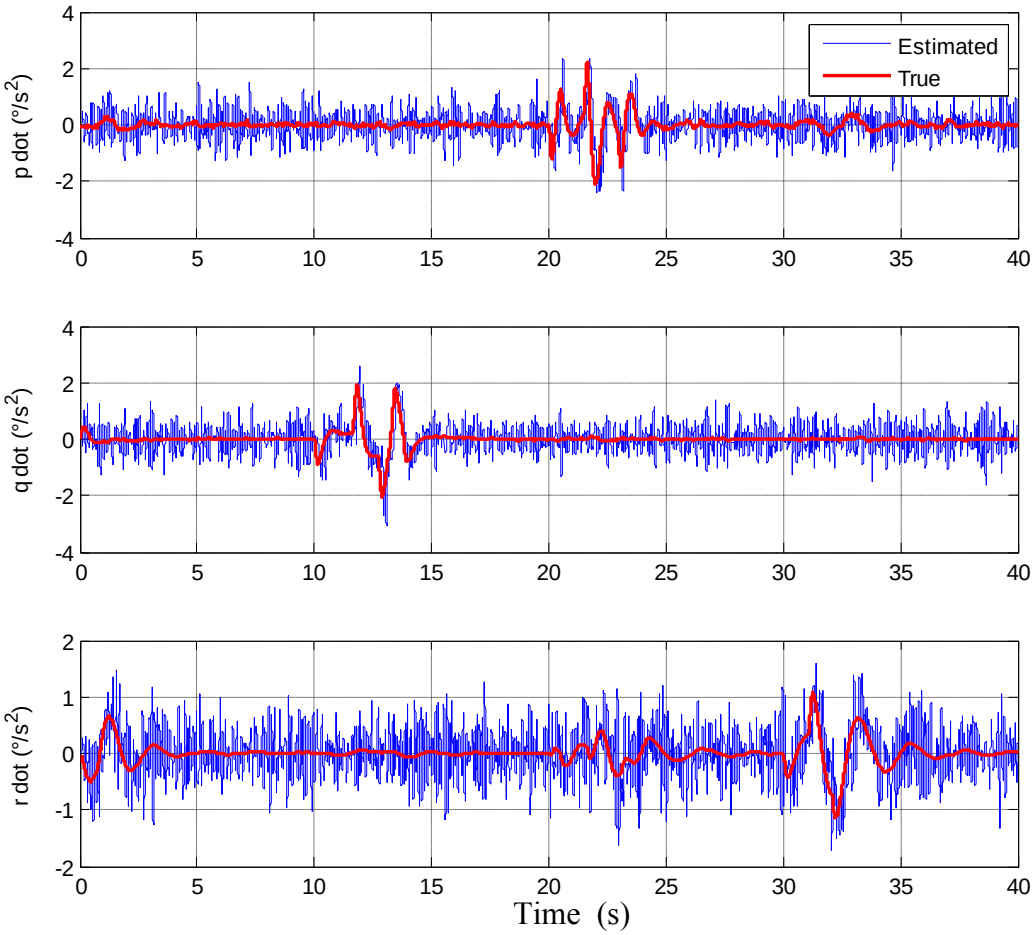

Figure 52: Actual vs Estimated angular accelerations

8.1.6 AoA estimation

Having estimated the sensor biases in Section 8.1.4, it is now possible, through the use of FPR, to estimate the AoA. The estimated AoA is thus given below:

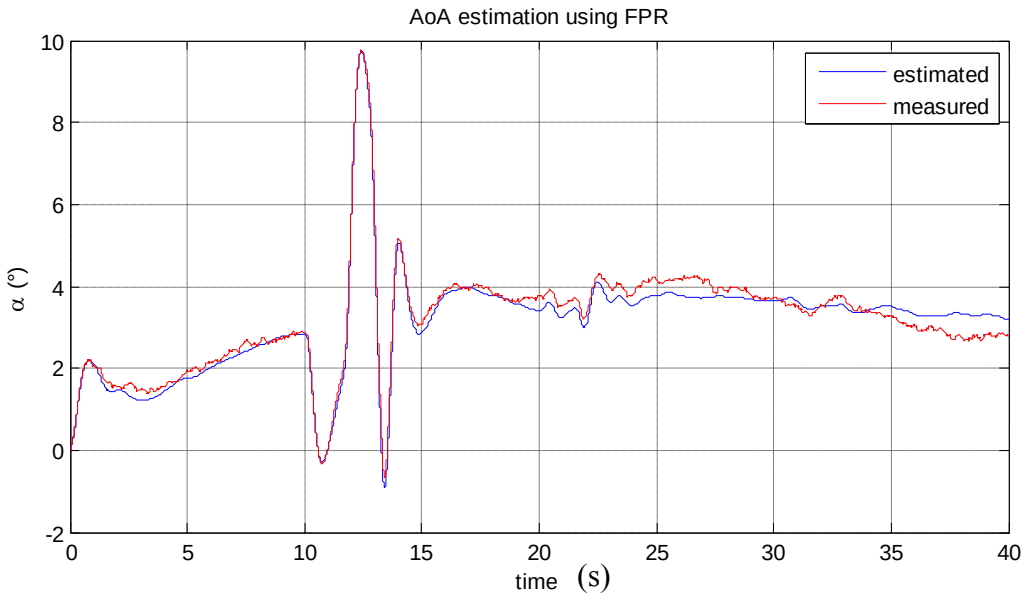

Figure 53: AoA estimate using FPR

For the offline implementation of SID, the previous method of determining the AoA has been shown to yield good results. A problem arises when trying to implement FPR in real-time. In the case of determining the biases (Section 8.1.4), it was assumed that, during the period in which the excitations are performed, the biases on the sensors are constant. This however is not the case with real sensors, as sensors experience bias drift and are thus constantly changing. As mentioned previously, any biases on the measured variables will introduce growing biases on the AoA estimates and result in inaccurate AoA estimates. To overcome this problem, it is possible to implement an extended Kalman filter in which the measured AoA is used as a measurement input.

The implementation of the extended Kalman filter will correct for the bias on the AoA estimate, ultimately resulting in a better AoA estimate. Due to time constraints, the extended-Kalman filter method as applied to FPR was not implemented.

8.1.7 Parameter Estimation: Short Period mode

The following section discusses the results obtained when performing system identification on the short period mode of the Modular UAV aircraft. To obtain the results stated below the following steps (according to the previous sections) was followed:

1. An elevator control input was determined (Section 8.1.2 a). The multi-step 3-2-1-1 input was chosen as it produces the best estimates.
2. The biases on the accelerometer and gyroscope measurements were determined using FPR and the Output-Error method (Section 8.4.1)
3. The angular accelerations were derived using numerical integration (Section 8.1.5)
4. An estimate of AoA was derived using the FPR method (Section 8.1.6)

a. Pitching moment Coefficients

Using the above mentioned measurements and inputs, system identification was performed on the Modular UAV aircraft. The first set of parameters of interest was those related to the pitching moment of the aircraft. As from Chapter 4, the aerodynamic pitching moment is given by the equation:

$$C_m = C_{m_0} + C_{m_\alpha}\alpha + \frac{\bar{c}}{2\bar{V}} C_{m_Q} Q + C_{m_{\delta_E}}\delta_E \tag{8.17}$$

where

$$C_m = \frac{1}{qSc}[I_y\dot{Q} + (I_x - I_z)PR] \tag{8.18}$$

In the case of the pitching moment equation, the regression equation for N samples can be formulated as:

$$\boldsymbol{z} = [C_m(1) \quad C_m(2) \quad \dots \quad C_m(N)]^T \tag{8.19}$$

$$\boldsymbol{H} = \begin{bmatrix} 1 & \alpha(1) & \bar{\bar{Q}}(1) & \delta_E(1) \\ 1 & \alpha(2) & \bar{Q}(2) & \delta_E(1) \\ \cdot & \cdot & \cdot & \cdot \\ \cdot & \cdot & \cdot & \cdot \\ \cdot & \cdot & \cdot & \cdot \\ 1 & \alpha(N) & \bar{Q}(N) & \delta_E(N) \end{bmatrix} \tag{8.20}$$

$$\boldsymbol{\theta} = \begin{bmatrix} C_{m_0} & C_{m_\alpha} & C_{m_Q} & C_{m_{\delta_E}} \end{bmatrix} \tag{8.21}$$

where the unknown stability and control derivatives can be calculated as:

$$\widehat{\boldsymbol{\theta}} = (\mathbf{H}^{\mathbf{T}}\mathbf{H})^{-1}\mathbf{H}^{\mathbf{T}}\mathbf{z} \tag{8.22}$$

or through the recursive implementation of the least-squares method. In the subsection to follow, the recursive least-squares method was used to estimate the aircraft parameters relating to the short period mode.

Results:

The results of system identification performed on the pitching moment dynamics is shown below:

Parameter	Estimated Value	True Value	% Error
C_{m_0}	0.0138	0	-
C_{m_α}	-1.0007	-1.0695	6.43 %
C_{m_Q}	2.9899	-18.4426	83.79 %
$C_{m_{\delta_E}}$	-1.0450	-1.4193	26.37 %

Table 10: Estimation of pitching moment coefficients (Q_dot determined by means of numerical differentiation)

From the table above, it is evident that the estimation using the least-squares method did not produce accurate results of the pitching moment coefficients. One possibility is that the short-period dynamics were not sufficiently excited, yielding parameters that have high correlation. The correlation matrix (shown below), however, does not agree with this statement:

$$\boldsymbol{H^{*T}H^{*}} = \begin{bmatrix} 1 & 0.6146 & -0.5496 \\ 0.6146 & 1 & -0.7659 \\ -0.5496 & -0.7659 & 1 \end{bmatrix} \tag{8.23}$$

Here it is evident that none of the parameters have a correlation of greater than 0.9. Further study into the estimation of the pitching coefficients showed that the high errors in the parameter estimates were due to the estimated pitching acceleration as determined in Section 8.1.5. The estimated angular acceleration as produced through numerical differentiation yielded a pitching acceleration with too low a signal-to-noise ratio. By using an estimated acceleration with less noise, the following results were obtained:

Parameter	Estimated Value	True Value	% Error
C_{m_0}	0.0034	0	-
C_{m_α}	-1.0469	-1.0695	4.92 %
C_{m_Q}	-18.8281	-18.4426	2.09 %
$C_{m_{\delta_E}}$	-1.4143	-1.4193	0.35 %

Table 11: Estimation of pitching moment coefficients (modified Q_dot)

Using a pitch acceleration measurement, that has less noise, better results were achieved. From the table above, all the measurements were estimated within 5% of their true values. The time histories of the estimated parameters are shown below:

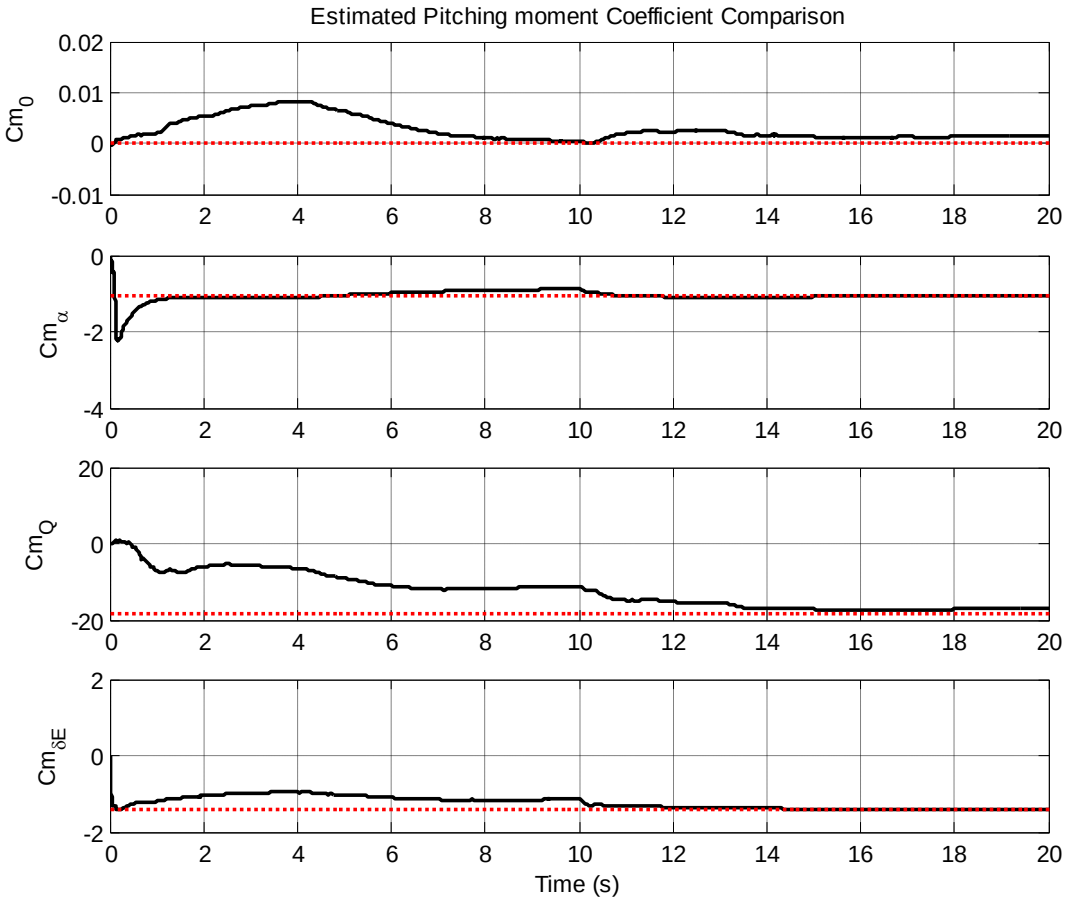

Figure 54: Time history of Pitch moment coefficients

b. Lift force Coefficients

The second set of dynamics that are linked to the short period mode, is the dynamics linked to the aerodynamic lift of the aircraft. From Chapter 4, the lift force coefficient can be determined from the equations:

$$C_L = C_{L_0} + C_{L_\alpha}\alpha + \frac{\bar{c}}{2\bar{V}} C_{L_Q} Q + C_{L_{\delta_E}} \delta_E \tag{8.24}$$

where

$$C_L = -C_z \cos\alpha + C_x \sin\alpha \tag{8.25}$$

And C_x and C_y can be determined from

$$C_x = \frac{1}{qS}(ma_x - T) \tag{8.26}$$

$$\mathrm{C_z} = \frac{\mathrm{m}}{\mathrm{qS}}\mathrm{a_z} \tag{8.27}$$

The above equations can then be used to determine the aerodynamic coefficients linked to the aerodynamic lift. The regression equations for the lift coefficients are thus given as:

$$\boldsymbol{z} = [C_L(1) \quad C_L(2) \quad \ldots \quad C_L(N)]^T \tag{8.28}$$

$$\boldsymbol{H} = \begin{bmatrix} 1 & \alpha(1) & \bar{Q}(1) & \delta_E(1) \\ 1 & \alpha(2) & \bar{Q}(2) & \delta_E(1) \\ . & . & . & . \\ . & . & . & . \\ . & . & . & . \\ 1 & \alpha(N) & \bar{Q}(N) & \delta_E(N) \end{bmatrix} \tag{8.29}$$

$$\boldsymbol{\theta} = \begin{bmatrix} C_{L_0} & C_{L_\alpha} & C_{L_Q} & C_{L_{\delta_E}} \end{bmatrix} \tag{8.30}$$

Results:

Applying the least-squares method to the above regression equation yields:

Parameter	Estimated Value	True Value	% Error
C_{L_0}	0.4919	0.500	1.62 %
C_{L_α}	5.3163	5.5579	4.35 %
C_{L_Q}	0.2021	8.0470	97.49 %
$C_{L_{\delta_E}}$	0.5502	0.4104	34 %

Table 12: Estimated lift coefficient comparison

From the table above, it is evident that the estimation using the least-squares method did not produce accurate results of the lift coefficients. From the correlation matrix, it can be shown once again, that the errors are not caused by correlation between the regressors, as none of the correlation coefficients are greater than 0.9:

$$\boldsymbol{H^{*T}H^{*}} = \begin{bmatrix} 1 & 0.5453 & -0.6191 \\ 0.5453 & 1 & -0.7554 \\ -0.6191 & -0.7554 & 1 \end{bmatrix} \tag{8.31}$$

By analyzing the influence of the different variables on the estimation result, it was found that the AoA measurement has big influence on the results. By using an accurate estimate of AoA (not that determined using FPR), the following results were obtained:

Parameter	Estimated Value	True Value	% Error
C_{L_0}	0.4987	0.500	0.26 %
C_{L_α}	5.5714	5.5579	0.24 %
C_{L_Q}	6.9091	8.0470	14.14 %
$C_{L_{\delta_E}}$	0.4339	0.4104	5.73 %

Table 13: Estimated Lift Coefficient using accurate AoA estimates

Comparing the estimated values in the table to those contained in the table before, the influence of the accuracy of the AoA measurement on the estimated parameters, is clearly evident.

The plots of the estimated parameters are shown below:

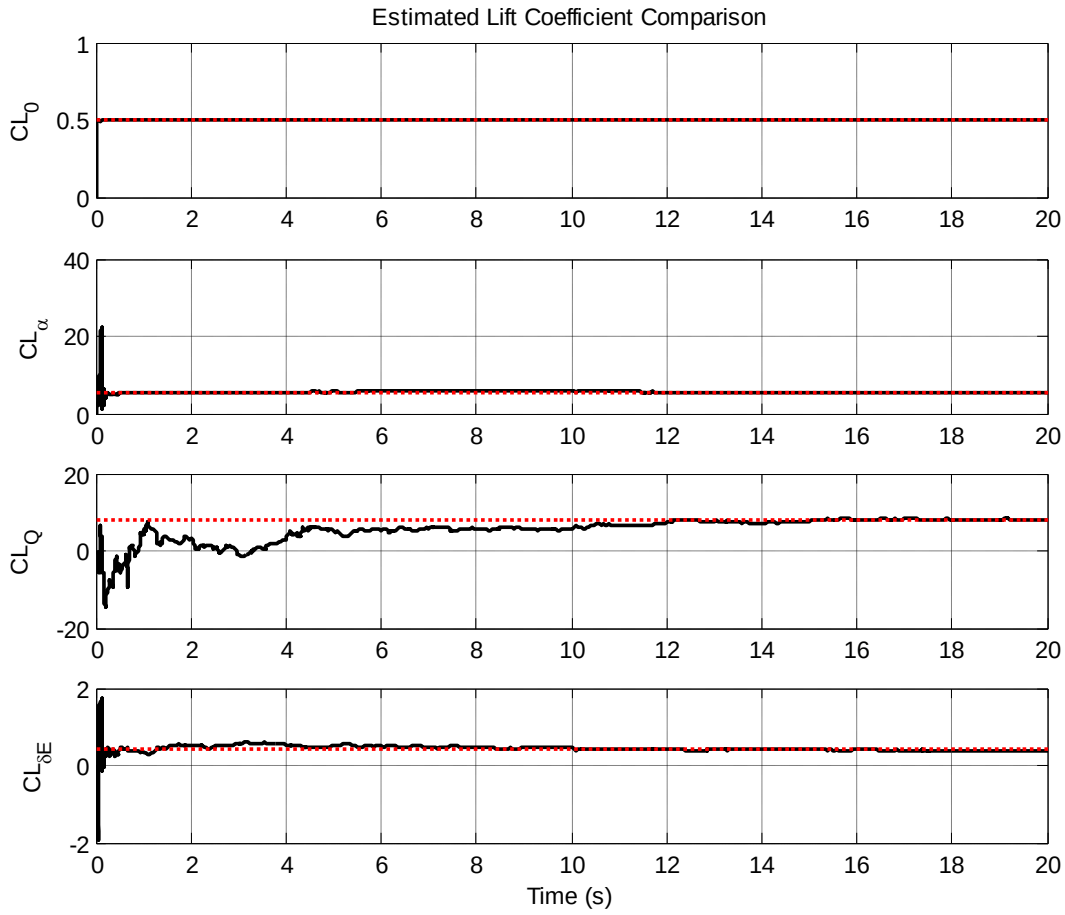

Figure 55 : Time history of the Lift coefficients

8.2 Conclusion

This chapter explored the application of the least-squares method to estimating the parameters that form part of the short period mode. The chapter covered the whole procedure, from data acquisition to estimation of the stability and control derivatives.

Some of the main findings of this chapter are summarized below:

1. The least-squares method is highly dependent on the quality of measurements.
2. Low cost gyroscopes are not advised for use in system identification. It was shown that numerical differentiation of gyroscopes did not produce angular acceleration measurement accurate enough for its use in system identification.
3. The AoA measurements have a major influence on the estimation of the aerodynamic lift coefficients. Measurements obtained solely through FPR, were not accurate enough to be used to determine these coefficients.

Though the focus of this chapter was primarily on the application of system identification on the short period mode, the same logic can be used to estimate the parameters of the roll and Dutch roll modes. These modes, however, will not be covered in this thesis. References to the estimation of these modes include [2, 12 and 9].

Chapter 9

Estimation from Flight Test Data

This section presents some findings of a flight test that was performed to test the System Identification approach presented in this thesis. Due to time constraints and the initial unavailability of a test aircraft, only one test was done. The Modular UAV aircraft was not available, and so the aircraft, the Sampieon, was used.

During this test, the aircraft was flown straight and level by an external pilot. Once stable, the aircraft was disturbed, by the pilot, by means of elevator inputs. Several doublet inputs were commanded on the elevator to stimulate the short period mode. As it is difficult for a pilot to command an elevator input with a specific frequency, the period of the doublet was chosen by discretion of the pilot. Several doublets were commanded until sufficient response was noted.

9.1 Prior Parameter Estimates

Following the steps that were presented in the previous chapter, prior Parameter estimates are required. The following aircraft parameters for the Sampieon were obtained from program AVL. As only estimation on the normal dynamics is considered in this thesis, the parameters related to this mode are shown below:

Parameter	Value
S	0.677
m	6.35
c	0.37
I_{yy}	0.5143
C_{m_0}	0
C_{m_α}	-0.664939

C_{m_Q}	-7.438796
C_{L_0}	0
C_{L_α}	4.4808411
C_{L_Q}	7.812170
$C_{m_{\delta E}}$	0.456085
$C_{L_{\delta E}}$	-0.957351

Table 14: Sampioen Aircraft Parameters

9.2 Kinematic consistency and Data check

As a first check, the kinematic check, making use of the FPR method was done, and the results shown below and in Appendix A:

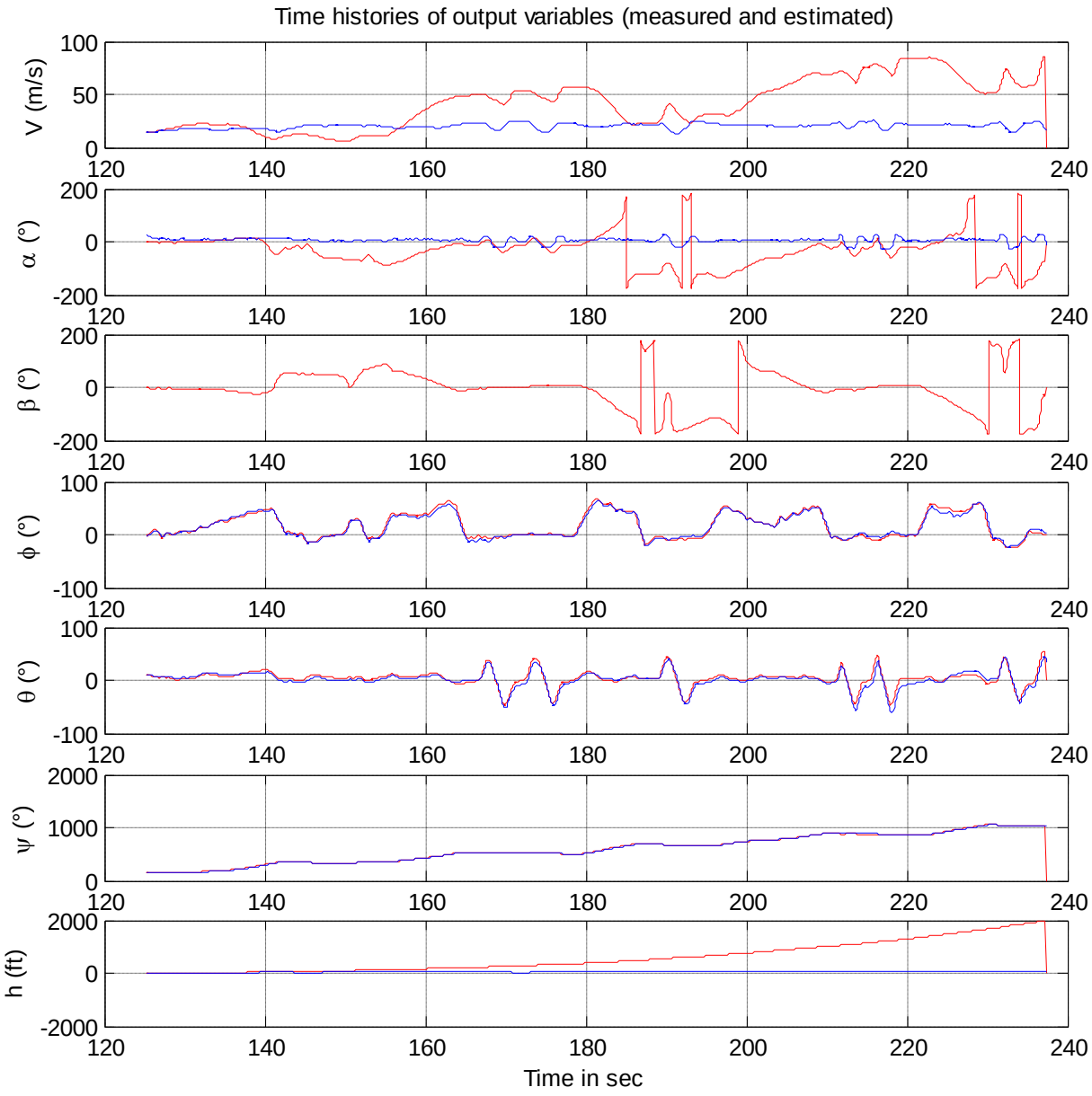

Figure 56: FPR applied to Flight Data

From Figure 56, it is evident that the flight data is not kinematically consistent. The divergence in the altitude and airspeed measurements clearly show that biases do exist on the measurements. Note that the red graphs refer to the estimated quantities and the blue to the measured.

Considering the attitude angles and comparing the estimated response to the measured responses, of Figure 56, it is evident that the measured and estimated responses match well.

One deduction that can be made from the fact that the estimated attitude angles match well with the measured attitude angles is that the biases on the recorded gyroscopes are small. This deduction is made as the attitude dynamics, as predicted through FPR, are solely dependent on the gyroscope measurements. This is evident from the attitude dynamics of Equations 4.25 (repeated below):

$$\dot{\phi} = P + \tan\theta\,(Q\sin\phi + R\cos\phi) \tag{4.25a}$$

$$\dot{\theta} = Q\cos\phi - R\sin\phi \tag{4.25b}$$

$$\dot{\psi} = Q\sin\phi\sec\theta + R\cos\phi\sec\theta \tag{4.25c}$$

It is therefore safe to assume that the effects of the accelerometer biases on the measured altitude and airspeed have a greater effect.

9.3 Bias estimation

The biases and scale factors, as determined from using the FPR and Output-Error method on the flight data, are shown below:

Parameter	Estimated Biases
Δp	$-9.24816\ 10^{-3}$ rad/s
Δq	$-5.27713\ 10^{-3}$ rad/s
Δr	$3.26087\ 10^{-3}$ rad/s
Δa_x	$-2.39983\ 10^{-2}$ m/s^2
Δa_y	$6.43052\ 10^{-2}$ m/s^2
Δa_z	$1.26461\ 10^{-1}$ m/s^2
K_α	1.6666
$\Delta\alpha$	0.1474 deg

Table 15: Bias Estimates from Flight Data

The gyroscope measurements and the accelerometer measurements as well as the AoA measurements were corrected for, and FPR was performed using these corrected measurements. The results of the FPR analysis are shown in Figure 57.

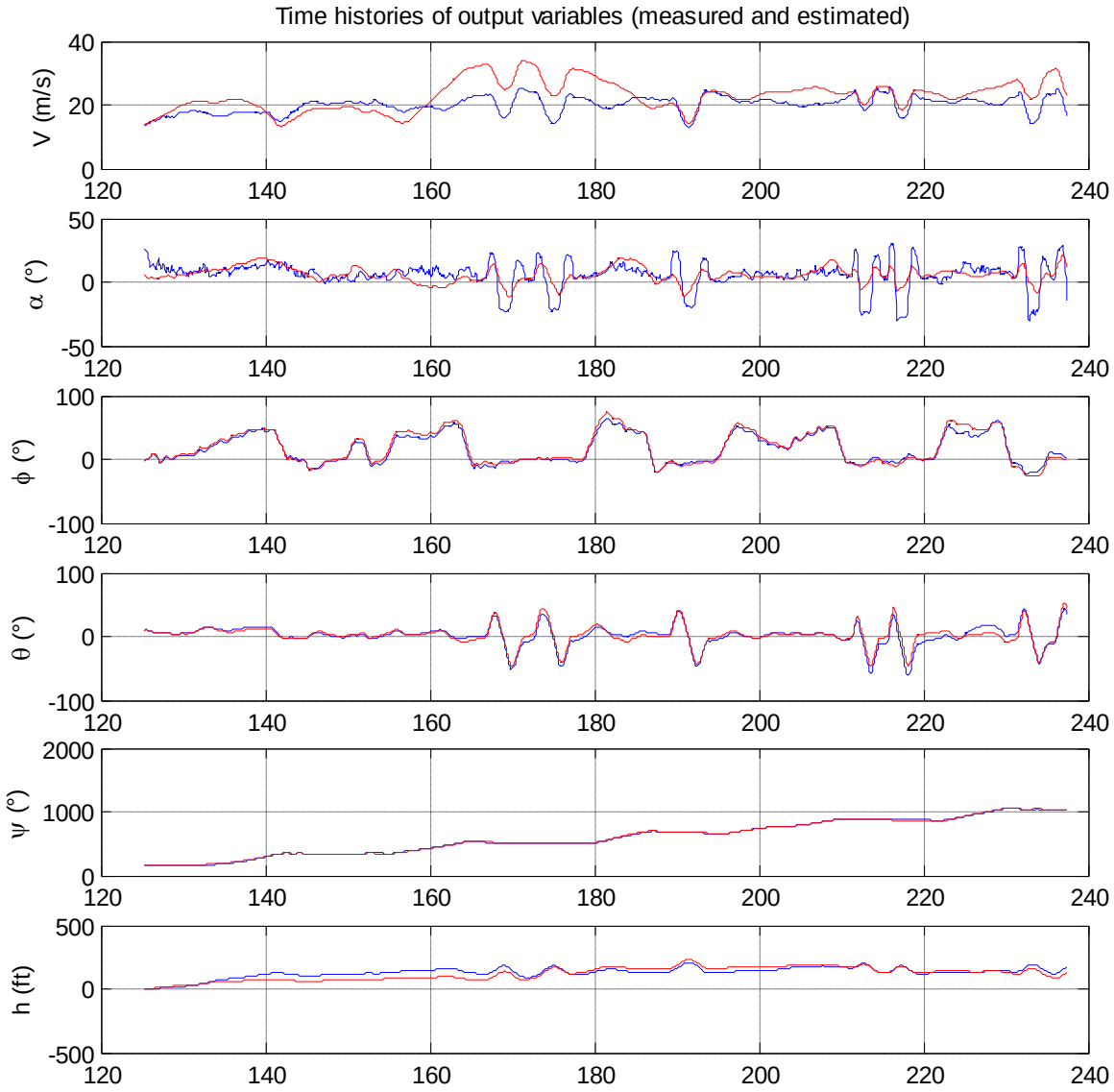

Figure 57: FPR on Flight Data after bias estimation

Figure 58, shows that by including the biases as estimated using the FPR and Output-Error method, the velocity and altitude estimates match the measured response much better than prior to correcting for bias effects. There are, however, still discrepancies or deviations between the measured and estimated airspeed measurements, as well as discrepancies between the measured and estimated AoA. The discussion of the AoA is done in Section 9.4.

The discrepancies between the measured and estimated airspeed responses can, for one, be attributed to residual biases on the measurements. As mentioned earlier, measurement instrumentation experience bias drift, causing the biases to change over a time period. Another possible cause is the effect of wind and gusts on the airspeed measurement. The FPR method does not account for wind and gust effects, which can have a considerable effect on the measured airspeed. A third possible source could be attributed to position errors. Position errors on accelerometer measurements will also affect the estimated airspeed.

To minimize the effect of bias drift on the estimated response, a shorter time period of data was used. For the rest of the analysis, the measurements taken between 165 seconds and 200 seconds are used. This time period was for two reasons:

1. The period is short enough, that the effect of bias drift should be minimal
2. There is seemingly enough longitudinal dynamics excited in this period

The biases, as determined for this time period, are shown below:

Parameter	Estimated Biases
Δp	$-1.75396\ 10^{-2}$ rad/s
Δq	$4.88058\ 10^{-2}$ rad/s
Δr	$-7.05364\ 10^{-3}$ rad/s
Δa_x	$9.78463\ 10^{-2}$ m/s^2
Δa_y	$-3.50564\ 10^{-2}$ m/s^2
Δa_z	$-3.03173\ 10^{-1}$ m/s^2
K_α	1.5385
$\Delta\alpha$	0.1310 deg

Table 16: Bias Estimates for time period 2

A comparison of the biases estimated using the full data set and those estimated over the period 165 to 200 seconds is shown below:

Parameter	**Estimated Biases (whole data set)**	**Estimated Biases (165 to 200 s)**
Δp	$-1.75396\ 10^{-2}$ rad/s	$-9.24816\ 10^{-3}$ rad/s
Δq	$4.88058\ 10^{-3}$ rad/s	$-5.27713\ 10^{-3}$ rad/s
Δr	$-7.05364\ 10^{-3}$ rad/s	$3.26087\ 10^{-3}$ rad/s
Δa_x	$9.78463\ 10^{-2}$ m/s^2	$-2.39983\ 10^{-2}$ m/s^2
Δa_y	$-3.50564\ 10^{-2}$ m/s^2	$6.43052\ 10^{-2}$ m/s^2
Δa_z	$-3.03173\ 10^{-1}$ m/s^2	$1.26461\ 10^{-1}$ m/s^2
K_α	1.5385	1.6666
$\Delta\alpha$	0.1310 deg	0.1474 deg

Table 17: Bias comparison

Here it is evident that the biases, as estimated using FPR, are not constant. The biases determined over a subset of the data are not equal to the biases as determined over the full test. This is an indication that bias drift is evident.

The responses, after the biases and scale factors have been accounted for, for the period 165 to 200 seconds (hereafter referred to as *time period 2*), is shown below:

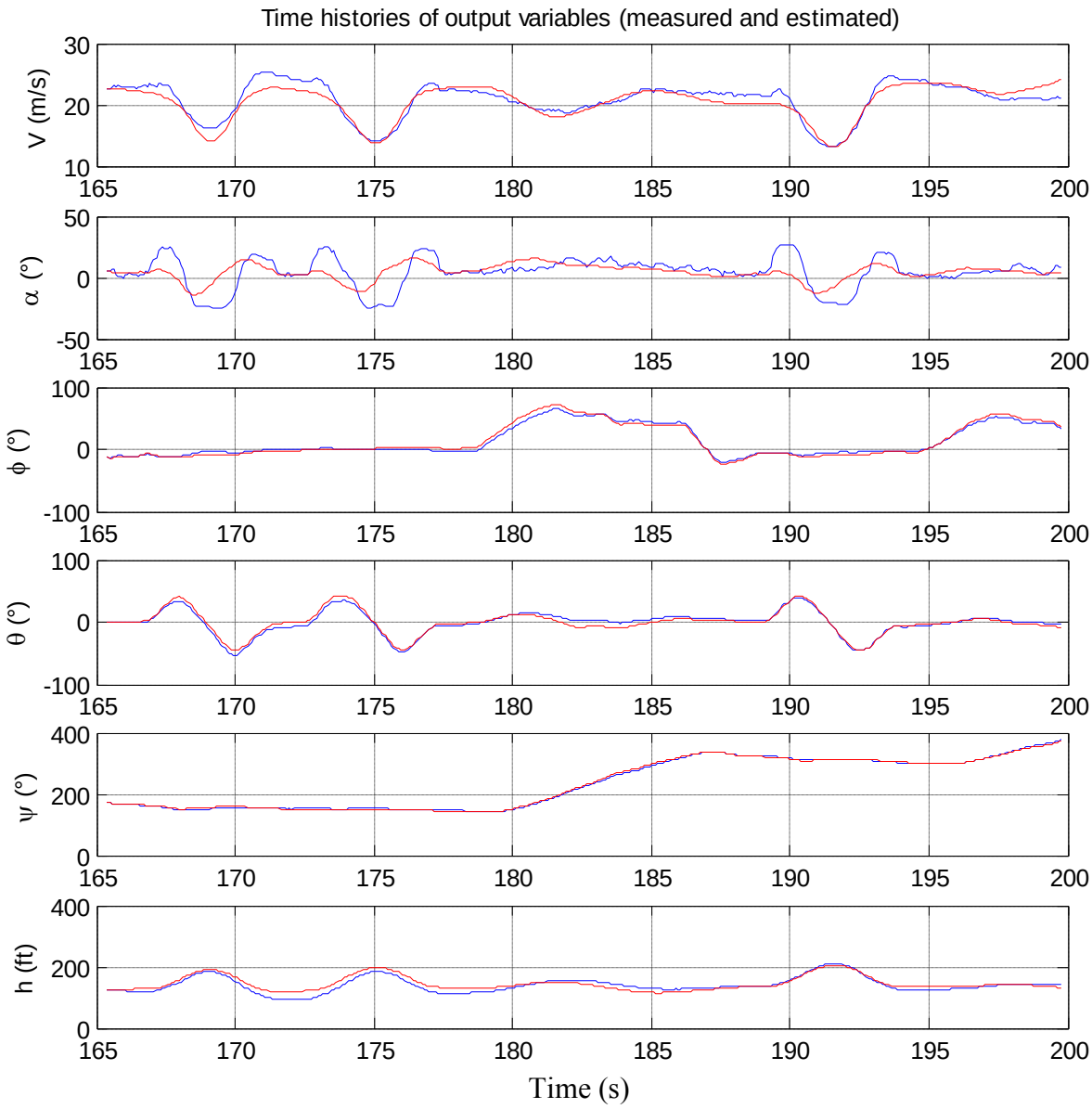

Figure 58: FPR for time period 2

As can be seen, the fit over the shorter time period is much better (compared to the fit across the full data set), as the effects of bias drift is minimized. Whereas before, considerable deviation from the measured airspeed was evident around the 175 second mark, the estimated airspeed now matches the measured response with greater accuracy. There is also a clear improvement in the estimated altitude.

With a better fit between the measured and estimated measurements, these measurements are now more suited for determining the aircraft parameters by means of the Regression method. One measurement not discussed as yet, is the AoA measurement. This discussion, however, is done in the next section.

9.4 AoA measurement

Having estimated the sensor biases, it is now possible, through the use of FPR, to estimate the AoA. The estimated AoA is thus given below:

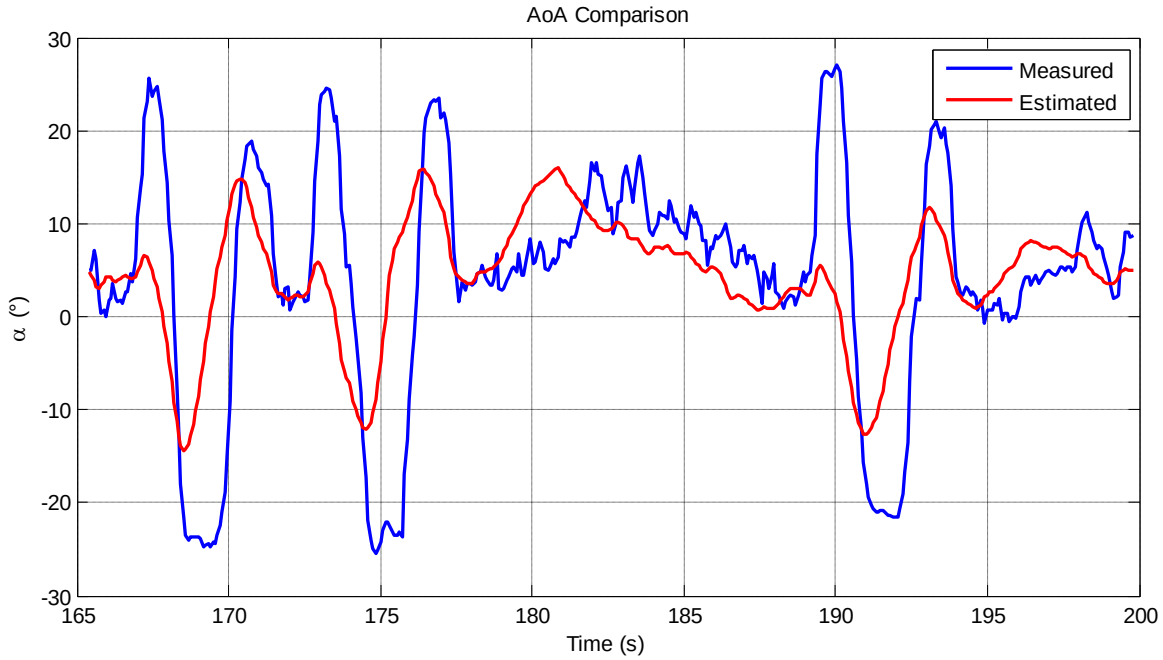

Figure 59: AoA measurement analysis

Here the bias and scale factor, as determined in the previous section, on the measured response has already been accounted for. Though the general response of the AoA measurement and AoA estimate exhibit similar dynamic response, there are 2 clear discrepancies evident:

1. The amplitude of the measured and estimated responses differ,
2. There exists a time-shift between the measured and estimated responses.

As the dynamic response of the AoA probe was not determined in the wind-tunnel tests, very little can be said about the time-shift in the data. More tests are needed to quantify the dynamic response of the sensor, such as to achieve a better fit between the measured and estimated responses.

If determined, the time-shift in the measured AoA must be corrected for, before being used in the parameter estimation algorithms. The difference in the amplitudes of the measured and estimated AoA should also be accounted for.

9.5 Angular Acceleration Estimation

As the distributed sensor method of determining the angular accelerations was not implemented on the aircraft, a the angular accelerations were determined by means of numerical differentiation as done in the simulation in Chapter 8. The results are shown below:

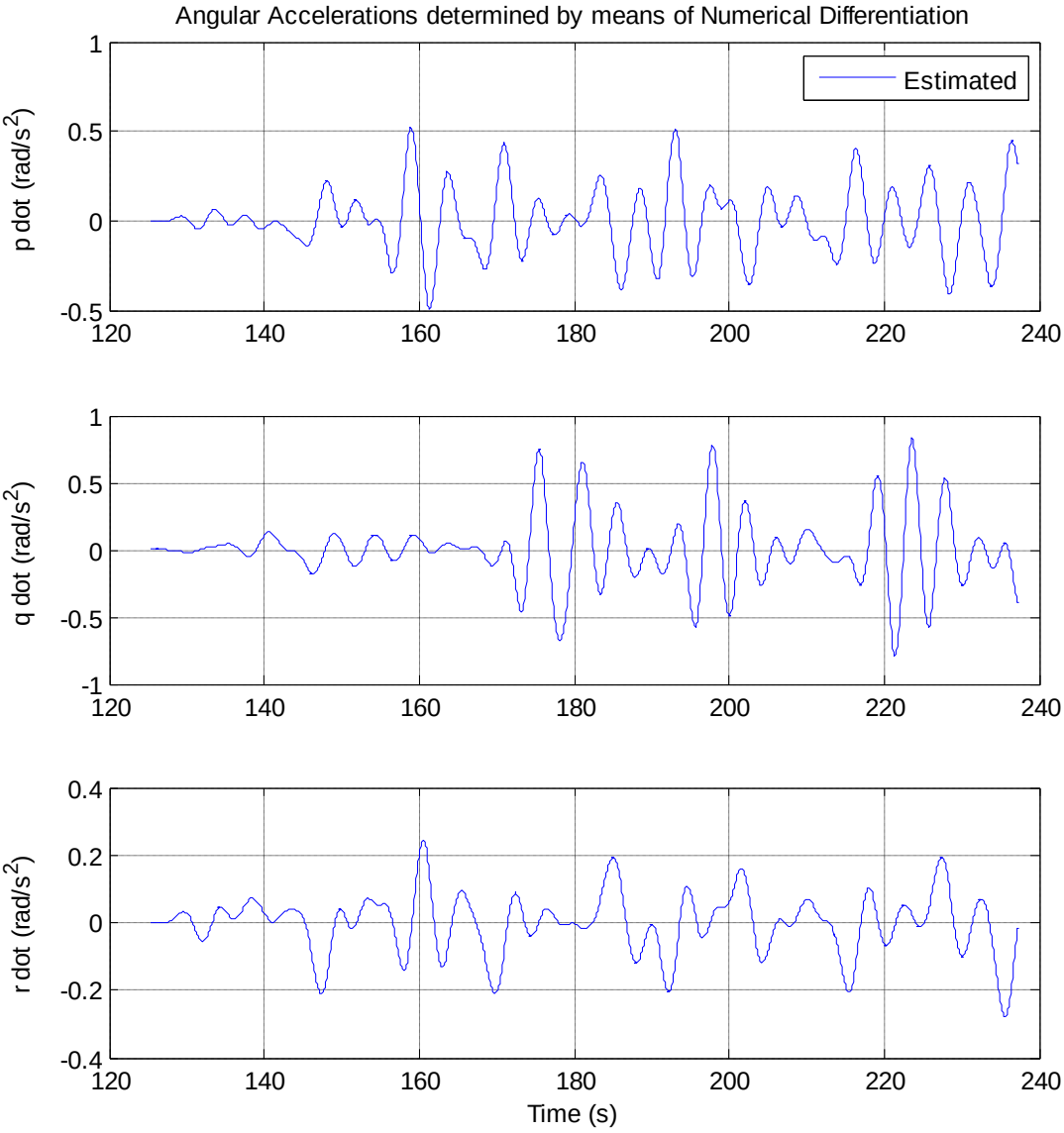

Figure 60: Angular accelerations determined through numerical differentiation

Here it is evident that on the actual flight data, the Angular Accelerations can be easily determined. The results show that the pre-filtering implemented both electronically and in the differentiation method was sufficient.

9.6 Parameter Estimation

Due to time constraints, an in depth analysis into Parameter estimation as applied to the flight data was not achieved. An attempt to estimate the aircraft parameters was made, but this was found to be unsuccessful.

The plots of the pitching moment coefficient as determined from the flight data of the aircraft Sampioen is shown below:

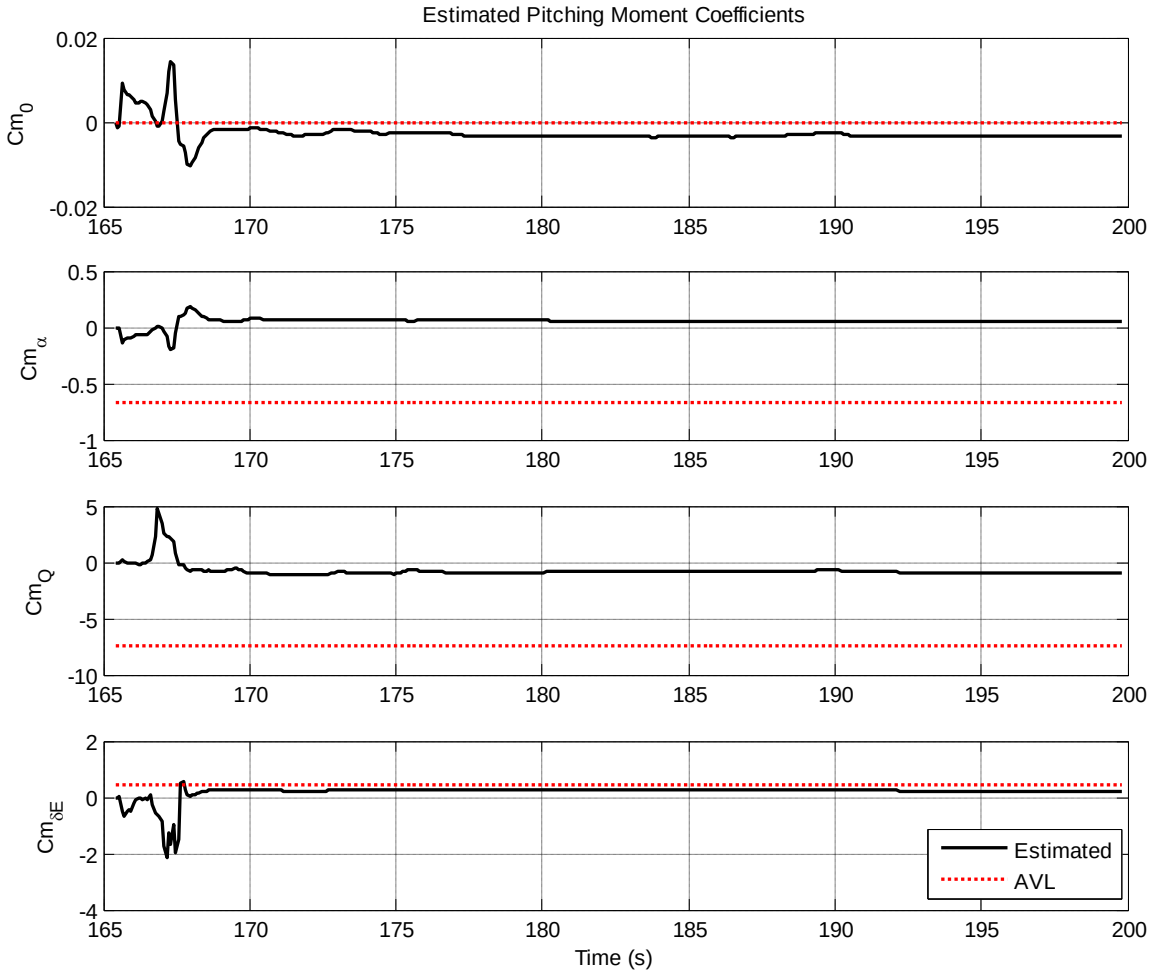

Figure 61: Pitching Moment Coefficients

From these figures it is evident that the estimated pitching moment coefficients do not mach those as determined from AVL. This however is made more clear in Table 18.

The table below shows a comparison of the aircraft parameters as estimated by means of the Regression method and the parameters as obtained from AVL.

Parameter	Estimated	AVL
C_{m_0}	-0.0034	0
C_{m_α}	0.0568	-0.664939
C_{m_Q}	-0.9387	-7.438796
$C_{m_{\delta E}}$	0.1936	0.456085

Table 18 : Comparison of AVL and Estmimated Pitching Moment Coefficients

As can be seen from the table above, the estimated parameters do not match those determined from AVL well. The correlation coefficients are given as

$$\boldsymbol{H^{*T}H^{*}} = \begin{bmatrix} 1 & 0.7172 & 0.0752 \\ 0.7172 & 1 & 0.0146 \\ 0.0752 & 0.0146 & 1 \end{bmatrix} \tag{9.1}$$

This indicates that the source of the problem is not correlation. By considering the pitch rate response (shown below) as well as the AoA response of the previous section, it is evident that there is sufficient dynamic response of the longitudinal dynamics.

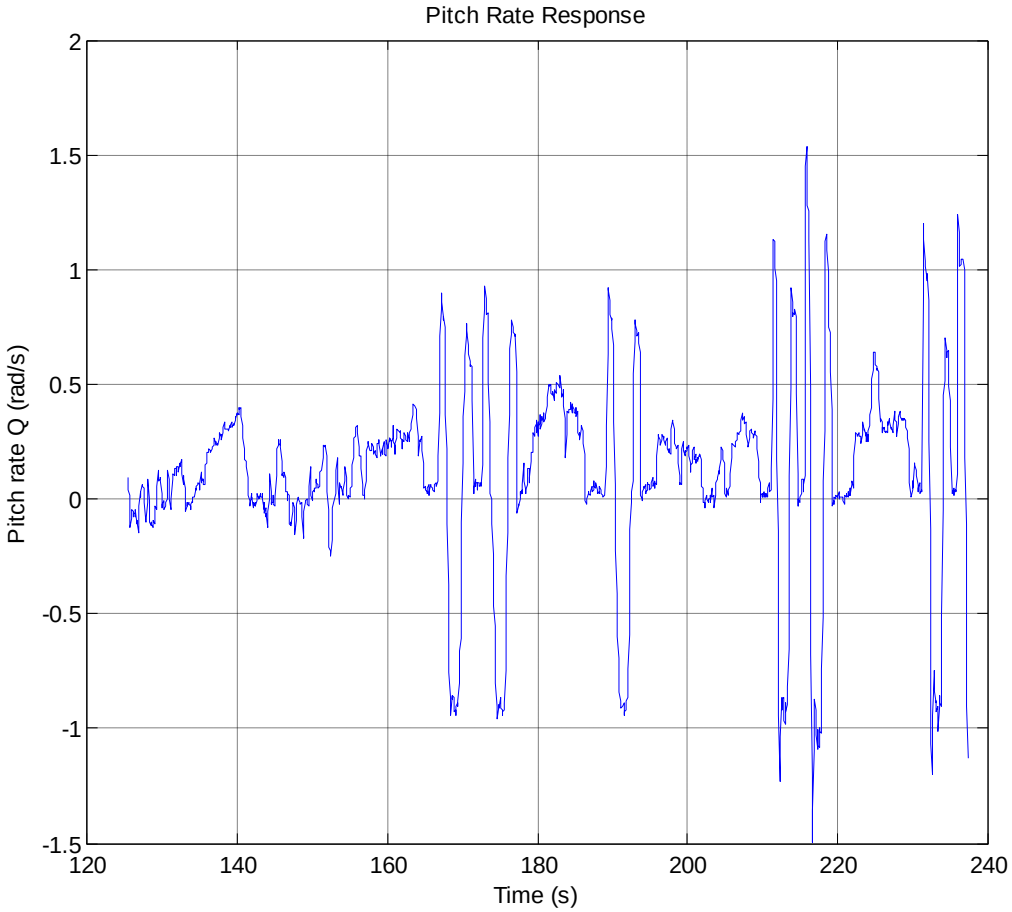

Figure 62: Measured Pitch Rate Response

Another possible source of error is the elevator command that used to determine the parameters. The elevator deflection as obtained through flight data is calculated from the elevator servo response, and is not the actual elevator deflection as experienced by the control surface. The command sent to the elevator servos is thus shown below:

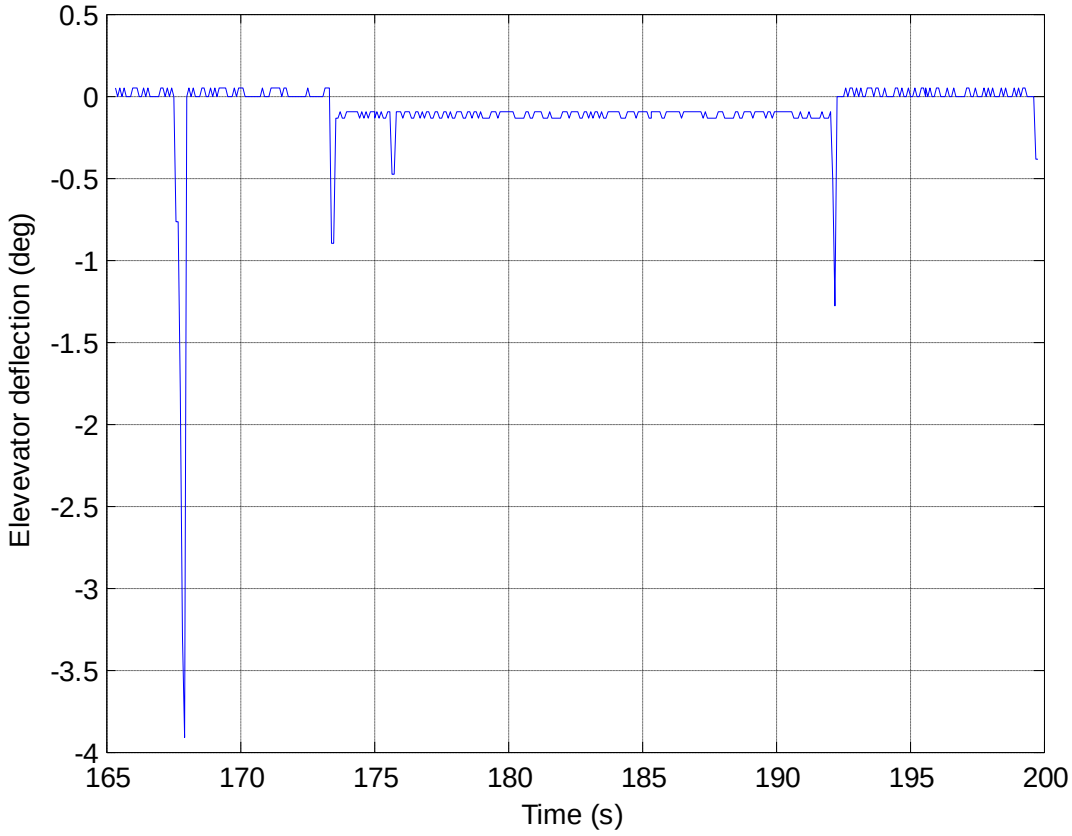

Figure 63: Elevator Response for time period 2

Here it is evident that for the most part, the elevator input was small. This could result in not enough elevator input to the Regression analysis and thus the estimation of incorrect parameters. To excite the short period mode an elevator doublet of a period in the order of 1 second should be commanded, this is not evident in the data presented above. The -4 degree elevator deflection shown, is just a spike in the received data.

9.7 Conclusion

In this chapter, the techniques in this thesis were applied to flight data. The measurement data obtained from the analysis could not be used to successfully estimate the aircraft parameters. Though the flight test was not successful in terms of aircraft parameter estimation, several lessons were learnt from the experience, these include:

1. It is necessary to properly calibrate sensors before flight. Not only to determine scale-factors and biases, but to also quantify any position errors that might be inherent because of the placement of the sensors.
2. 1 flight test is not enough as it does not provide enough data to for both calibration and parameter estimation and validation.
3. Programming the control inputs (elevator, rudder and aileron inputs) into the autopilot would yield better results, as better excitation of different aircraft modes can be achieved through more accurate control inputs.
4. Numerical Differentiation of the Gyroscopic measurements are sufficient to produce angular acceleration measurements.
5. By shortening the period over which the data is analyzed, the effects of bias drift on the estimation of sensor biases can be minimized.
6. The AoA sensor needs to be properly calibrated and the dynamic response of the sensor determined.

Chapter 10

Summary and Recommendations

10.1 Summary

This thesis provided a framework for the implementation of System Identification for aircraft parameter estimation, using flight data. The thesis covers most of the issues involved in system identification, from defining an aircraft model to the implementation of parameter estimation on flight data.

The thesis starts with the derivation of a 6 degree-of-freedom model that is used throughout this text for both simulation and analysis. This is followed by the selection of the method used for parameter estimation. Several different methods were considered, amongst these were:

1. The Regression technique (based on the Least-squares method)
2. The Output-Error method.
3. The filter error method.

The Regression method was chosen to be used as it was seen to be the easiest to implement, it requires less computational time to process and is more suited for real-time implementation. These properties were found to be sufficient to justify its choice over the previous methods.

The regression method, however, is based on the assumption that the measurements that are used to make up the regressor matrix are error free, and thus do not contain noise or biases. This is however is never the case when implementing the method using actual flight data. The estimated parameters, as obtained from the regression method, are shown to be highly dependent on the quality of the measurements.

As the regression method was found to be dependent on the quality of the measurement, a method for checking the validity of flight data was presented. Flight Path Reconstruction, enables one to not only check whether all the measurements agree kinematically, but also provides a means to estimate the biases on the measurements and thus correct for them.

Even if it were possible to obtain error free measurements, this would not ensure that accurate parameters would be estimated. The issue of Parameter Identifiability was thus explored in Chapter 5. It was shown that if the aircraft's dynamics were not sufficiently excited during parameter estimation, the regression method would yield singularities, resulting in poor or inaccurate measurements. To solve this problem, different aircraft control surface inputs were discussed. These included Rudder, Elevator and Aileron inputs, which would sufficiently excite the aircraft modes (Dutch roll mode, short-period mode and roll mode) for parameter estimation.

The focus of Chapter 6 and Chapter 7 was on the obtaining of flight data. In the process of estimating the aircraft parameters, certain measurement are required that are not currently being measured on the aircraft at the ESL. These measurements include the angle-of-attack, the angle-of-sideslip and the angular accelerations.

Chapter 6 presents different methods for obtaining the angle-of-attack measurement. In this chapter, the design, test and calibration of an angle-of-attack sensor was presented. The sensor was built and calibrated in a wind-tunnel at the University of Stellenbosch.

Another method explored to obtain angle-of-attack measurements, was through the estimation. 2 different models were looked at and discussed. The first being based on the short-period mode dynamics of the aircraft and the second being a model based on the kinematic relationship of the different measured variables. The main downfall of the method based on the short-period mode dynamics, is that the accuracy of the angle-of-attack measurement is dependent on the aircraft parameters. In a Fault Tolerant Framework, the aircraft parameters are assumed to be varying and not known exactly. In this case the estimated angle-of-attack, as determined using the short-period model, will not be accurate.

The second approach to estimating the angle-of-attack that was considered was based on the FPR method presented previously. Here the estimated angle-of-attack was based solely on the measured aircraft states. This method was seen to be more robust, when applied in a Fault Tolerant Framework and was thus chosen.

Chapter 7 covered the estimation and determination of the angular accelerations of an aircraft. A novel method, using distributed accelerometers was proposed. In this method the angular accelerations could be determined directly. The method of obtaining these measurements through numerical differentiation was also proposed. Here several different differentiation

schemes were presented including Savitzky-Golay filters, Smoothed differentiators as well as methods that filter and differentiate signals separately.

Chapter 8 summarized the previous chapters by showing the application of the different methods to a non-linear simulation of the Modular UAV aircraft. This chapter highlights the possible problems that can be experienced when applying the different methods presented in this thesis to flight data. The findings of this chapter are summarized below:

1. Sensor biases and scale factors can be successfully estimated by making use of the FPR and Output-Error method. In doing this, it is possible to correct the measurements so that they are kinematically consistent with each other.
2. By including the AoA sensor as an output variable it is also possible, through the use of FPR and the Output-Error method, to calibrate the AoA sensor using flight data.
3. Angular accelerations as determined through numerical differentiation, was found to be inadequate for System Identification purposes. The signal-to-noise ratio of the resulting measurements was found to be too low, with the noise dominating the signal. It was thus suggested that the best means to determine the angular accelerations, is through distributed sensoring.
4. AoA measurements can be determined by means of FPR, when there is no AoA sensor.
5. It was shown, through simulation; how the accuracy of the measured data used to form the regressors, affect the accuracy of the parameters determined. The AoA measurements were shown to have a major influence on the accuracy of the aerodynamic lift coefficients. Measurements obtained solely through FPR, were not accurate enough to be used to determine these coefficients.

Chapter 9 explored the use of the system identification methods on flight data. The measurement data obtained from the flight test showed kinematic inconsistencies that could not be corrected by means of the Output-Error and FPR methods. The data was thus not suitable for aircraft parameter estimation.

Though the data obtained on the flight test was found not able to successfully estimate the aircraft parameters, the data was used to validate some of the other concepts presented in this thesis. One finding was that, though the AoA measurements were not accurate in terms of its scale, the dynamic response of the sensor fit the dynamic response of the aircraft. This

showed that if calibrated properly, the AoA sensor can be used to determine the AoA successfully.

Another finding was that, though the simulation proved otherwise, angular acceleration can be determined from flight data using numerical methods. The actual gyroscope measurements show less noise than that simulated in the non-linear model and thus could be differentiated.

In summary, this thesis showed the processes involved in obtaining aircraft parameter estimates from flight data. The different problems associated with obtaining these estimates were discussed and recommendations for alleviating or minimizing these problems were presented. This thesis thus provides a basis for further research into the implementation of aircraft parameter estimation for real-time applications within a Fault Tolerant Framework.

10.2 Recommendations

In this thesis system identification was applied to actual flight data. The thesis focused primarily on the determination of the stability and control derivatives that form part of the short-period mode of the aircraft.

Following the work presented here, the following is recommended for future work:

1. In-flight calibration of the AoA sensor
2. Online implementation of the Recursive least-squares method on an aircraft
3. Implementation of distributed sensoring
4. Implementation of the Kalman filter version of FPR, for real-time bias estimation

11 Bibliography

[1] I.K. Peddle, *Fault Tolerant Control: Overview and Research at Stellenbosch University*. IASSA, 2009.

[2] W.H. Pietersen. *System Identification for Fault Tolerant Control of Unmanned Aerial Vehicles*, Masters Thesis, 2010.

[3] I.K. Peddle. *Acceleration Based Maneuver Flight Control System for Unmanned Aerial Vehicles.* Ph.D. thesis, University of Stellenbosch, 2008.

[4] W. Milliken. *Progress in stability and control research*. Journal of theAeronautic Sciences, Vol. 14, 494–519, 1947.

[5] H.Greenberg.*A survey of methods for determining stability parameters of an airplane from dynamic flight measurements*. Tech. Rep., NASA TN2340, 1951.

[6] M.Shinbrot. *A least squares curve fitting method with application ofthe calculation of stability coefficients from transient-response data*. Tech.Rep., NASA TN 2341, 1951.

[7] K.W. Iliff, R.E. Maine. *Bibliography for Aircraft Parameter Estimation*. NASA Technical Memorandum 86804, 1986.

[8] V. Klein, E.A. Morelli. *Aircraft System Identification: Theory and Practice*. Reston, VA: American Institute of Aeronautics and Astronautics, 2006.

[9] V. Klein. *Estimation of aircraft aerodynamic parameters from flight data*. Progress in Aerospace Sciences, vol. 26, no. 1, pp. 1–77, 1989.

[10] V.Klein. *Identification evaluation methods. Parameter Identification*.AGARD-LS-104, Paper 2, 1972.

[11] P. Hamel, R. Jategaonkar.*Evolution of flight vehicle system identification*.Journal of Aircraft, vol. 33, pp. 9–28, 1996.

[12] R.Jategaonkar.*Flight Vehicle System Identification, A Time Domain Methodology*. Reston, VA: American Institute of Aeronautics and Astronautics, 2006.

[13] M.B. Tischler, R.K. Remple. *Aircraft and rotorcraft system identification: engineering methods with flight-test examples.* Reston, VA: American Institute of Aeronautics and Astronautics,2006.

[14] M.V. Cook. *Flight Dynamics Principles*. Elsevier Butterworth-Heinemann, 1997.

[15] B. Etkin. *Dynamics of Atmospheric Flight*. John Wiley & Sons, 1972.

[16] B. Etkin, L.D. Reid. *Dynamics of Flight, Stability and Control*, 3rd Ed. John Wiley &Sons, 1996.

[17] D. R. Gaum. *Aggressive Flight Control Techniques for a Fixed-Wing Unmanned Aerial Vehicle*. Master's thesis, University of Stellenbosch, 2009.

[18] L.V. Schmidt. *Introduction to Aircraft Flight Dynamics*. AIAAEducational Series, 1998.

[19] P.H. Zipfel. *Modeling and Simulation of Aerospace Vehicle Dynamics,* 2nded. AIAA Educational Series, 2006.

[20] F. Schweppe. *Uncertain Dynamic Systems.* Prentice-Hall, Upper Saddle River, NJ, 1973.

[21] R.A. Fisher. *Theory of Statistical Estimations*, Vol. 22, Proceedings of the Cambridge Philosophical Society, pp. 700-725, 1925.

[22] T.R. Fortescue, L.S. Kershenbaum, and B.E. Ydstie. Implementation of self-tuning regulators with variable forgetting factors. Automatica, 17, 6:831 -835, 1981.

[23] H.L. Jonkers, *Application of the Kalman filter to Flight Path Reconstruction from Flight Test Data including estimation of instrumental bias error corrections.* Delft University of Technology, 1976.

[24] L.C.S. Goes, E.M. Hemerly, B.C.O. Maciel, *Parameter Estimation and Flight Path Reconstruction using Output-Error method.* 24th International Congress of Aeronautical Sciences, 2004.

[25] R.A. Stuckey, *Identification of Nonlinear Model Parameters- Spoiler Aerodynamics of the F-111C Aircraft.* PHD thesis, University of Sydney, 1995.

[26] E. Sofyan, *Identification of Model Aircraft Dynamic Using Flight Testing.*Masters thesis, Royal Melbourne Institute of Technology, 1996.

[27] W.J. Hough, *Autonomous Aerobatic Flight of a Fixed Wing Unmanned Aerial Vehicle*. Masters thesis, Stellenbosch University, 2007.

[28] D.G. Hull, *Fundamentals of Airplane Flight Mechanics*. Springer, 2007.

[29] M. Buschmann, J. Bange, P. Vörsmann, *MNAV- A miniature Unmanned Aerial Vehicle (Mini-UAV) for Meterological Purposes*. TechnischeUniversitatBraunscheweig, Germany.

[30] A. van den Kroonenberg, T. SpießJBange, *First wind measurements with the meteorological UAV 'M2AV Carolo'*. Institute of Aerospace Systems at Technical University Braunschweig, Germany, 2007.

[31] T. Spiess, J. Bange, M. Buschmann, P. Vörsmann, *First application of the meteorological Mini-UAV 'M2AV'*. Institute of Aerospace Systems at Technical University Braunschweig, Germany, 2006.

[32] C. Ippolito, *Wind Tunnel Calibration of the Exploration Aerial Vehicle (EAV) Five-Hole Pitot Probe*. NASA Ames Research Center, 2006.

[33] W. Gracey, *Summary of Methods of Measuring Angle of Attack on Aircraft*. Tech. Rep., NACA TN 4351, 1958.

[34] K. Kim, B. Shafai, and E. Kappos, *Proportional integral estimator*. Proceedings of SPIE Signal and Data Processing of Small Targets, Orlando. Fl, vol. 1096, pp. 187-208, 1989.

[35] Ö.Y. Bas, B. Shafai, S.P. Linder, *Design of Optimal Gains for the Proportional Integral Kalman Filter with application to Single Particle Tracking.* Northeastern University, Boston, 1999.

[36] S.P. Linder, B. Shafai, *Rejecting Disturbances to Flexible Structures using PI Kalman Filters.* Proceedings of the 1997 IEEE International Conference on Control Application Hartford, CT,1997.

[37] S.P. Linder, B. Shafai, *Robust PFI Kalman Filters.* Proceedings of the American Conttrol Conference Philadelphia, Pennsylvania, 1998.

[38] J. Lan, C. Mu, *A strong tracking proportional integral Kalman Filter for nonlinear system state estimation.* Proceedings of the Fourth International Conference on Machine Learning and Cybernetics, Guangzhou, 2005.

[39] P. Axelsson, U. Orguner, F. Gustafsson, M. Norrlöf, *ML Estimation of Process Noise Variance in Dynamic System.* Linkoping University.

[40] M. Enescu, M. Sirbu, V. Koivenen, *Recursive estimation of noise statistics in Kalman Filter based on MIMO equalization.* Helsinki University of Technology.

[41] P. Holoborodko, *Applied Mathematics and Beyond*. Viewd 30 November, 2012,

<http://www.holoborodko.com/pavel/>

[42] P. Persson, G. Strang, *Smoothing by Savitzky-Golay and Legendre Filters.*

[43] G.J.J. Guillaume, *Fault-tolerant Flight Control and Guidance Systems, Practical Methods for Unmanned Aerial Vehicles.* Advanced Industrial Control, Springer, 2009.

[44] Y. Zhang, J. Jaing, *Bibliographical review on reconfigurable fault-tolerant control system*. Annual Reviews in Control, 32, 229-252, 2008.

[45] J. Jaing, X. Yu, *Fault-tolerant control systems: A comparative study between active and passive approaches.* Annual Reviews in Control, 36, 602012.-72, 2012.

[46] I.K. Peddle, *Fault Tolerant Control: Overview and Research at Stellenbosch University*. IASSA, 2009.

[47] V. Klein, P.C. Murphy, *Aerodynamic Parameters of High Performance aircraft estimated from wind tunnel and flight test data.* NASA, 1998.

[48] R.E Maine, K.W. Iliff, *Application of Parameter Estimation to Aircraft Stability and Control, The Output-Error Approach.* NASA Reference Publication, 1168, 1986.

12 Appendix A: Flight Data (Sampioen)

The following measurement data was obtained during the flight test of Test Case 1:

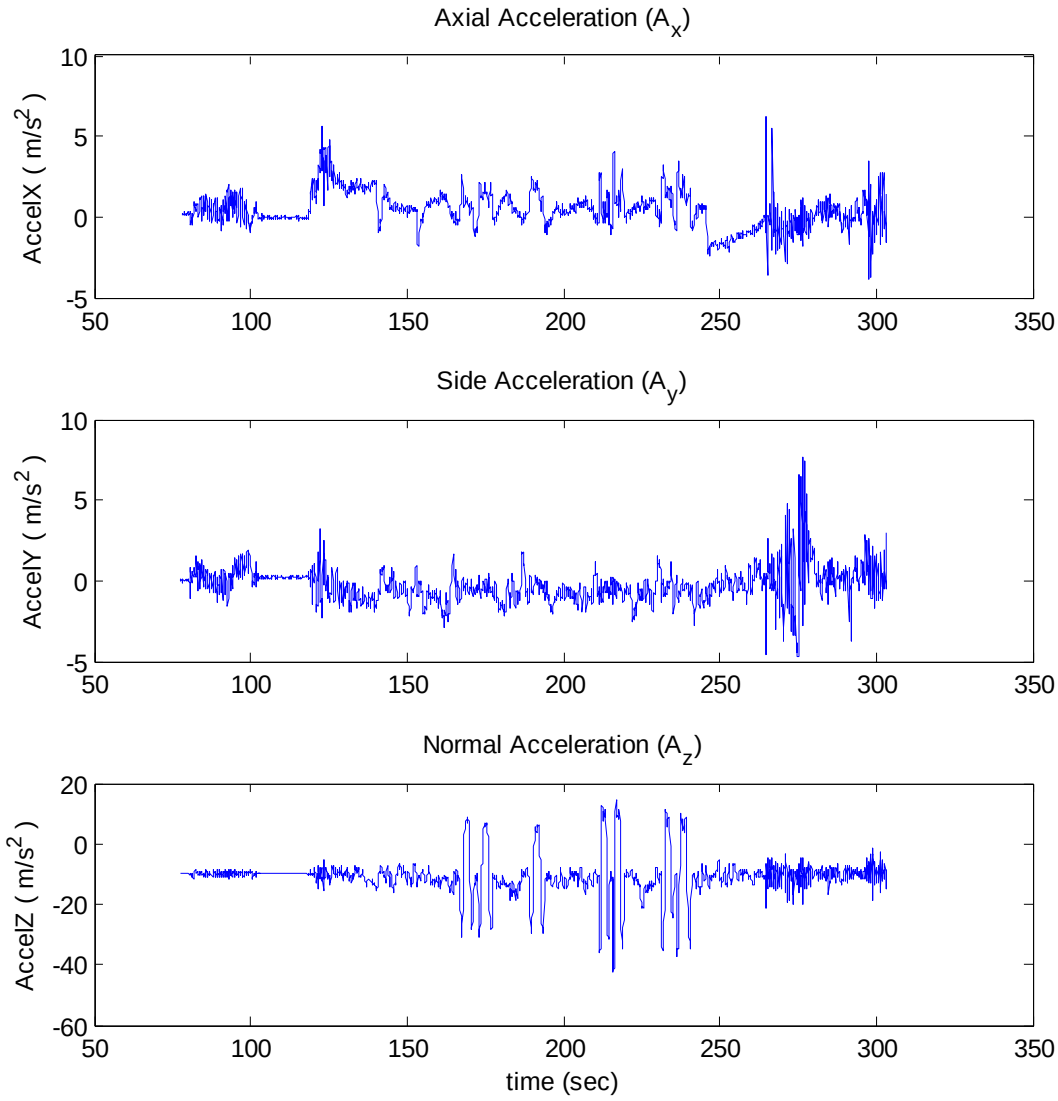

Figure 64: Accelerometer Measurements (Sampioen)

.

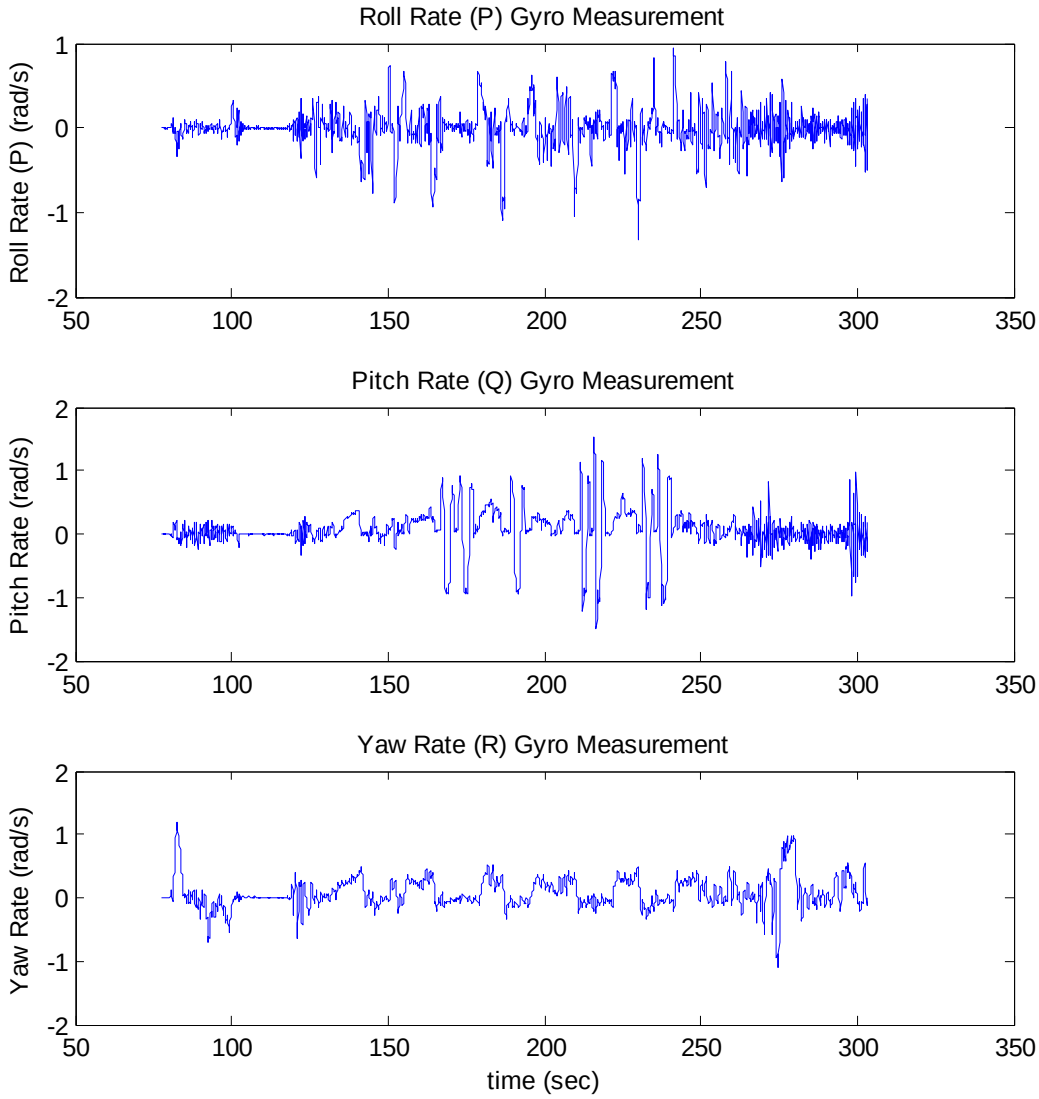

Figure 65: Gyroscope measurements (Sampieon)

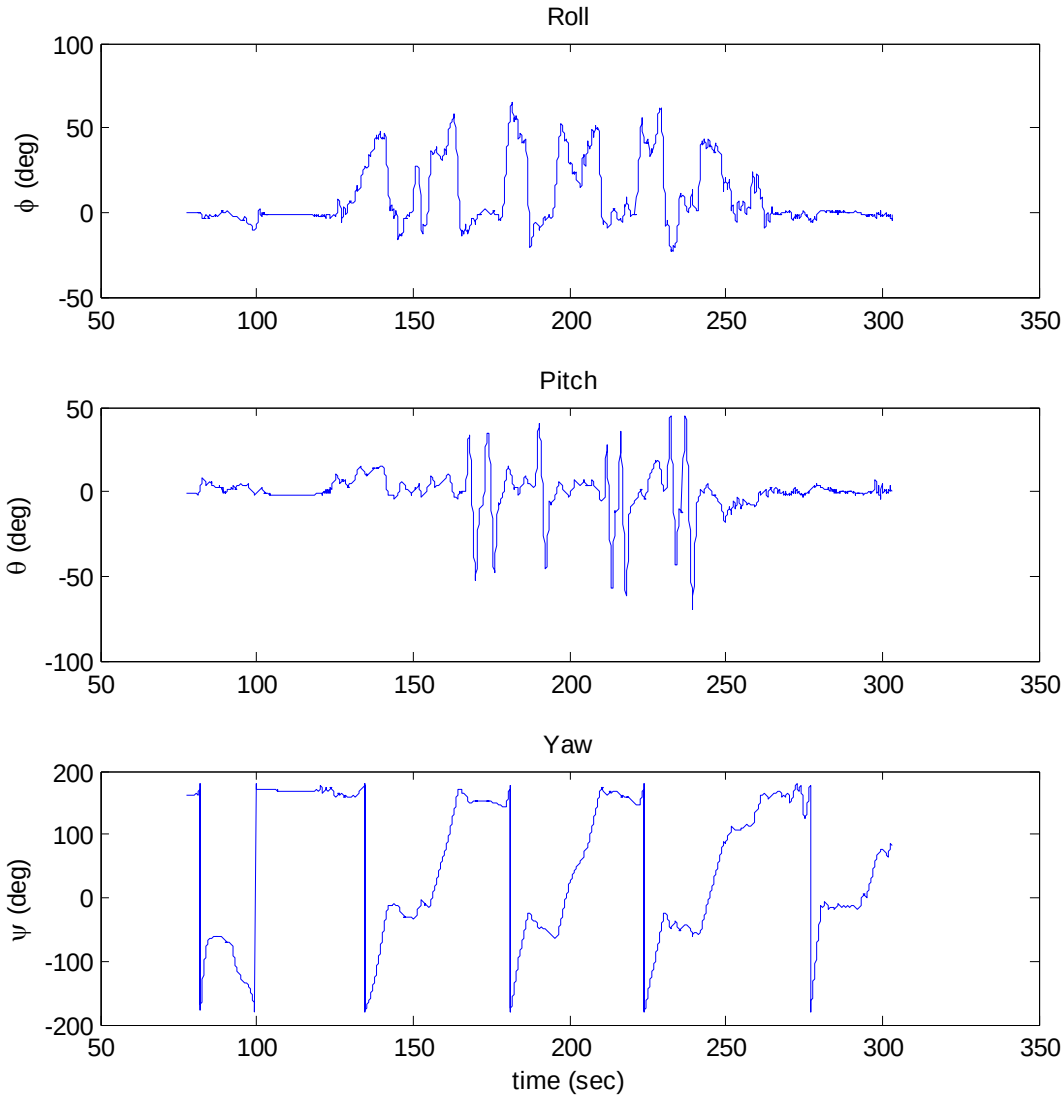

Figure 66: Measured Attidtude Angles (Sampioen)

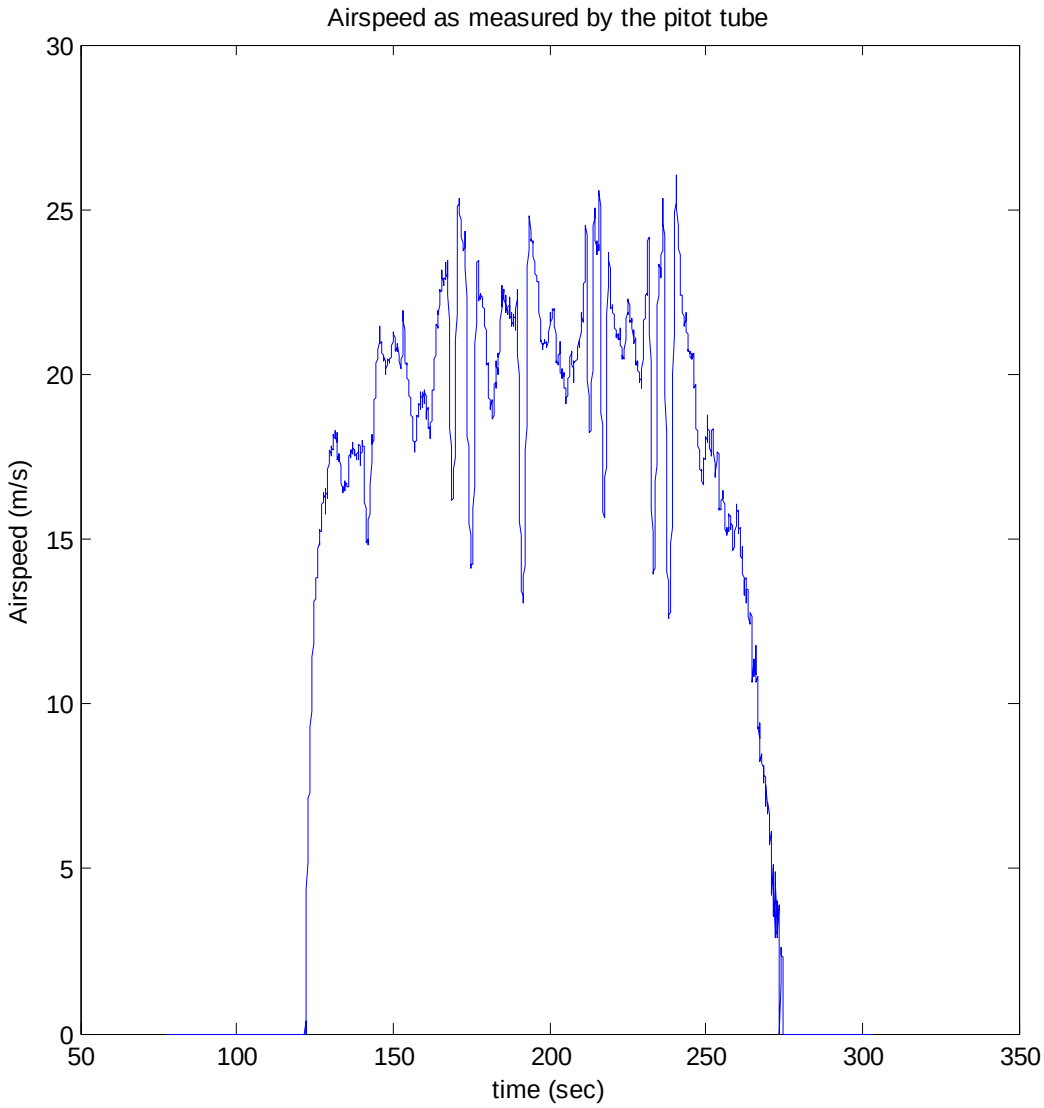

Figure 67: Airspeed Measurements (Sampioen)

13 Appendix B: Output Error Method

The output error method is summarized in the flow diagram below:

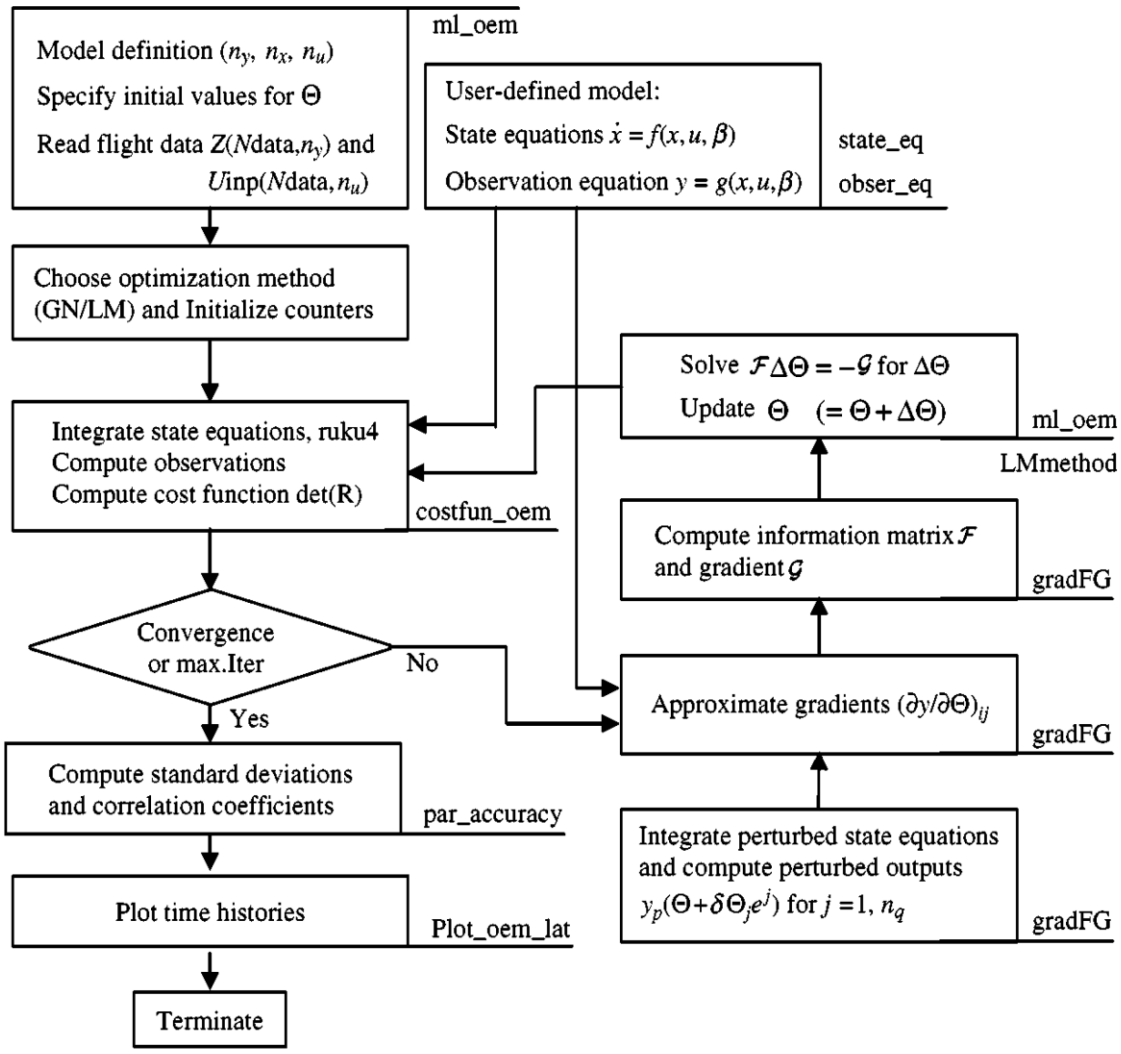

Figure 68: Details of implemented output error method

The flow diagram shown above was obtained from Jategoankar (1996). The flow diagram shows how the Output-Error method was implemented in the function ml_oem.m. For a detailed description of how the output error method is implemented in ml_oem, refer to Chapter 6 of Jategoankar (1996)